2011

Model Identification, Updating, and Validation of an Active Magnetic Bearing High-Speed Machining Spindle for Precision Machining Operation

Adam C. Wroblewski
Cleveland State University

Recommended Citation

Wroblewski, Adam C., "Model Identification, Updating, and Validation of an Active Magnetic Bearing High-Speed Machining Spindle for Precision Machining Operation" (2011). *ETD Archive*. 310.
https://engagedscholarship.csuohio.edu/etdarchive/310

MODEL IDENTIFICATION, UPDATING, AND VALIDATION OF AN ACTIVE MAGNETIC BEARING HIGH-SPEED MACHINING SPINDLE FOR PRECISION MACHINING OPERATION

ADAM C. WRÓBLEWSKI

Bachelor of Science in Mechanical Engineering
Cleveland State University
December, 2006

Master of Science in Mechanical Engineering
Cleveland State University
December, 2008

Submitted in partial fulfillment of requirements for the degree
DOCTOR OF ENGINEERING
at the
CLEVELAND STATE UNIVERSITY
August, 2011

This dissertation has been approved

For the Department of Mechanical Engineering

And the College of Graduate Studies by

Dr. Jerzy T. Sawicki

Department/Date

Dr. Stephen F. Duffy

Department/Date

Dr. James A. Lock

Department/Date

Dr. Taysir H. Nayfeh

Department/Date

Dr. Ana V. Stankovic

Department/Date

ACKNOWLEDGEMENTS

The successful completion of this dissertation is owed to many individuals that have been very helpful throughout this endeavor. To begin with, I thank my advisor, Dr. Jerzy T. Sawicki who has continually provided his wealth of expertise over the past several years. His dedication to his students has been instrumental to the advancement of my skills as an engineer and as a researcher. I thank my committee members, Dr. Stephen F. Duffy, Dr. James A. Lock, Dr. Taysir H. Nayfeh, and Dr. Ana V. Stankovic for providing valuable feedback on my research topic early in my research process. Their multidisciplinary guidance has aided in the final course that my work has taken. I thank my fellow graduate students Alexander H. Pesch and Ryan J. Madden for their friendship and assistance in the laboratory work that was required. Their talents have added to the value of the RoMaDyC laboratory's research efforts. I thank Dr. Randy J. Locke and Dr. Mark P. Wernet for their ongoing encouragement of my graduate study. Finally, I thank my parents, Michael and Maria, for teaching me the importance of education and for their continuous support of my graduate study.

MODELING AND IDENTIFICATION OF ACTIVE MAGNETIC BEARING HIGH-SPEED MACHINING SPINDLE FOR HIGH-SPEED PRECISION MACHINING OPERATION

ADAM C. WROBLEWSKI

ABSTRACT

High-Speed Machining (HSM) spindles equipped with Active Magnetic Bearings (AMBs) are envisioned to be capable of autonomous self-identification and performance self-optimization for stable high-speed and high quality machining operation. High-speed machining requires carefully selected parameters for reliable and optimal machining performance. For this reason, the accuracy of the spindle model in terms of physical and dynamic properties is essential to substantiate confidence in its predictive aptitude for subsequent analyses.

This dissertation addresses system identification, open-loop model development and updating, and closed-loop model validation. System identification was performed in situ utilizing the existing AMB hardware. A simplified, nominal open-loop rotor model was developed based on available geometrical and material information. The nominal rotor model demonstrated poor correlation when compared with open-loop system identification data. Since considerable model error was realized, the nominal rotor model was corrected by employing optimization methodology to minimize the error of resonance and antiresonance frequencies between the modeled and experimental data.

Validity of the updated open-loop model was demonstrated through successful implementation of a MIMO μ-controller. Since the μ-controller is generated based on the spindle model, robust levitation of the real machining spindle is achieved only when the model is of high fidelity. Spindle performance characterization was carried out at the tool location through evaluations of the dynamic stiffness as well as orbits at various rotational speeds. Updated model simulations exhibited high fidelity correspondence to experimental data confirming the predictive aptitude of the updated model. Further, a case study is presented which illustrates the improved performance of the μ-controller when designed with lower uncertainty of the model's accuracy.

TABLE OF CONTENTS

LIST OF FIGURES

LIST OF TABLES

NOMENCLATURE

$a_{ij,k}$	Antiresonance error
$act, amb, sens, tool$	Subscripts for actuator, AMB, sensor, and tool
$\mathbf{A,B,C,G}$	State-space free-free rotor representation
AC	Alternating current
A_g	Area face of pole
A/D	Analog to digital
AMB	Active magnetic bearing
AMT	Association for Manufacturing Technology
AVC	Active vibration control
$B(\mathbf{e})$	Black-box function
CAD	Computer aided design
CAM	Computer aided manufacturing
CNC	Computer numerical control
d_f	Number of degrees of freedom
D/A	Digital to analog
DN	Speed factor
$\mathbf{e}$	Vector design variables, modulus of elasticity
e_p	Design variables, modulus of elasticity
err	Error value
E	Modulus of elasticity
EDM	Electrical discharge machining

f	Force
ff	Subscript for free-free condition
$\mathbf{f}$	Vector of input forces
F	Force of electromagnet
F_{amb}	Force of opposed magnetic actuator pair
F_{imp}	Impulse response force
F_{stp}	Step response force
FE	Finite element
FEA	Finite element analysis
FEM	Finite element model
g	Target-to-electromagnet gap
G_0	Experimental open-loop transfer function
$\mathbf{G}(s)$	Matrix of experimental transfer function measurements
$\mathbf{G}(j\omega_f)$	Matrix of experimental open-loop transfer functions
HF	High frequency
HSM	High-speed machining
$\mathbf{H}_n, \mathbf{H}_n^R$	Transfer matrices
i	Current
i_b	Bias current
i_c	Control current
i,j	Subscripts for AMB input and output axes

I_p	Polar moment of inertia
I_t	Transverse moment of inertia
ID	Inner Diameter
k	Flexible mode number
k_i	Current stiffness
k_k	Spring rate
k_n	Spring rate at n^{th} location
k_x	Position stiffness
K	Controller
$\mathbf{K}_i$	Matrix of current stiffness
$\mathbf{K}_x$	Matrix of position stiffness
l	Finite element length
L	Left side
m	Mass
m_f	Number of flexural modes
m_n	Mass at n$^{\text{th}}$ location
m_r	Number of rigid-body modes
m_t	Total number of modes
MIMO	Multiple-input, multiple-output
MRR	Material removal rate
MSF	Mode scale factor

n	Number of design variables
ns	Station number
N	Number of coils
NCDMM	National Center for Defense Manufacturing and Machining
NIST	National Institute of Standards and Technology
OD	Outer diameter
P_0	Modeled open-loop transfer function
PID	Proportional integral derivative controller
PCD	Poly-crystalline diamond
$r_{ij,k}$	Resonance error
R	Right side
RoMaDyC	Center for Rotating Machinery Dynamics and Control
$\mathbf{s}$	State vector of node position
$\mathbf{S}$	Selection matrix
SISO	Single-input, single-output
SME	Society of Manufacturing Engineers
SMS	Smart machining system
t	Time
t_{imp}	Impulse duration in time
TDC	Top dead center
TF	Transfer function
u_i	Input signal to AMB

$\mathbf{u}$	Vector of input signals to AMB
$\mathbf{u}_{act}$	Vector of control currents to actuator
$\mathbf{U}(\omega_f)$	Fourier coefficients of signal inputs
v	Control voltage
v,w	Subscripts, rotor's longitudinal planes
$\mathbf{w}_{tool}$	Vector of forces at tool location
x	x-axis coordinate
x_c	Nominal radial clearance
x_r	Radial displacement
x_{nc}	Sensor/actuator noncollocation
y	y-axis coordinate
y_j	Sensor signal from AMB
$\mathbf{y}$	Vector of output positions
$\mathbf{Y}(\omega_f)$	Matrix of Fourier coefficients of response outputs
$\mathbf{Z}_n^R, \mathbf{Z}_n^L$	Vector of state variables
ε	Geometric correction factor
μ_0	Magnetic flux permeability constant in vacuum
ρ	Density
$\tilde{\phi}_k$	Calculated mode shape vector
$\hat{\phi}_k$	Experimental mode shape vector

ω_f	Frequency
$\tilde{\omega}_{ij,k}$	Calculated resonance frequency
$\hat{\omega}_{ij,k}$	Experimental resonance frequency
${}^{a}\tilde{\omega}_{ij,k}$	Calculated antiresonance frequency
${}^{a}\hat{\omega}_{ij,k}$	Experimental antiresonance frequency
Ω	Rotor angular speed

CHAPTER I

INTRODUCTION

High-Speed Machining (HSM) is a rapidly evolving field in industry and is tightly integrated with the Smart Machining Systems (SMS) initiative. Smart machining systems incorporate all aspects of machining technologies, from software to hardware, in efforts to advance and integrate all areas of the machining process. The smart machining system is commonly described as a mode to enable the cost effective manufacture of parts to specification, on schedule, for the first part and every part thereafter. The smart machining initiative is recognized by numerous industry leaders and organizations which hold meetings for the exchange of progress in technology and standardizations. Several organizations involved are the National Institute of Standards and Technology (NIST), Society of Manufacturing Engineers (SME), Cincinnati-based TechSolve, Association for

Manufacturing Technology (AMT), and the National Center for Defense Manufacturing and Machining (NCDMM) [1] [2].

Smart machining systems require intelligence in the machining process to improve machine reliability, optimize machining performance, and allow for long term unmanned operation [3] [4]. This requires extensive application of science and physics based approaches to understand the machines themselves, as well as their processes. In addition, advancements in feedback and sensing capabilities will allow for intelligent, self-correcting operation [5] [6]. Capabilities such as self-monitoring and optimization of operation, self-assessment of work quality, self-learning and performance improvement, enhanced vibration monitoring, active thermal compensation, and enhanced operator interaction are envisioned for the future of smart machining systems. Such features aid in the machine's autonomous operation with less dependency on the machine operator's guidance and experience.

1.1 Introduction to High-Speed Machining

High-speed machining has received a lot of attention in recent years due to many of its attractive qualities such as shorter machining cycles, higher part accuracy, better surface finishes, and overall lower production costs in comparison to conventional machining techniques [7]. High-speed machining simultaneously shortens machining cycles and improves the accuracy of machined surfaces, despite the unintuitive nature of improving the two contradictory objectives. With application of high-speed machining, reduced cutting forces and increased Material Removal Rates (MRR) are achieved [8].

Figure 1 graphically illustrates general properties of HSM [9] showing trends in cutting volume, surface quality, cutting forces, and tool life, as a function of cutting speed.

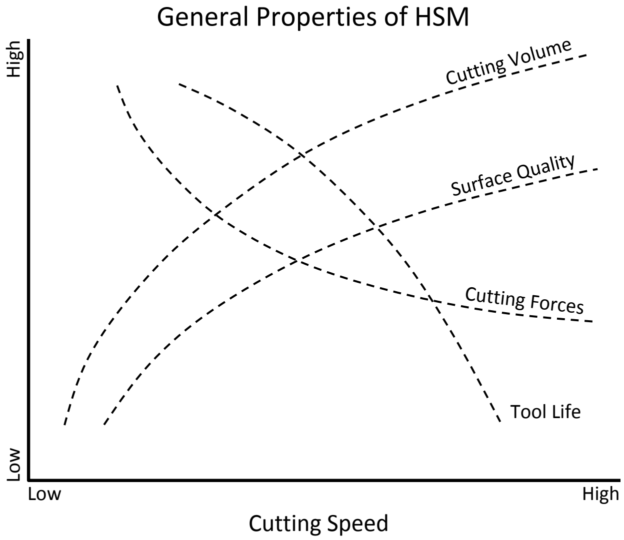

Figure 1: General properties of high-speed machining [9].

The term high-speed machining is commonly reserved for spindles that are capable of rotational speeds of 15,000 rpm and higher. Although most machine shops may consider high-speed machining an exotic technique, many large companies have employed it with great success, particularly in the aerospace industry. For example, certain aircraft components can be machined from a single block of aluminum rather than joining a number of machined or stamped parts into an assembly. With application of HSM, the feasibility of efficiently producing large monolithic parts is greatly increased. Figure 2 shows an example of the same airframe component with both standard and monolithic construction [10]. The monolithic construction offers lower cost, faster production time, and lighter component weight, while concurrently increasing its strength and rigidity [7] [11].

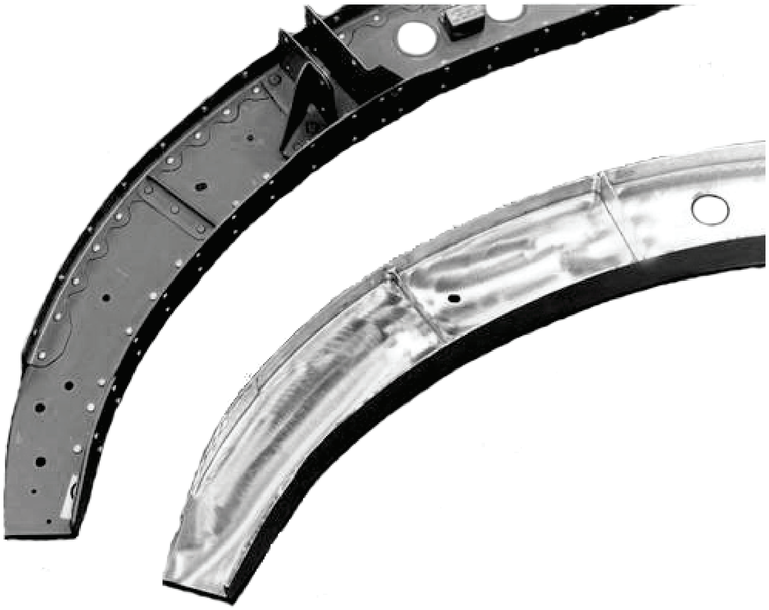

Figure 2: Airframe component, standard (top) and monolithic (bottom) construction [10].

A well designed, robust HSM spindle achieves high power at fast rotational speeds without generating large amounts of torque and tangential loads during cutting. This substantially reduces the loads endured by the machined part, cutting tool, and spindle bearings [12]. Most often the limiting factor of increasing machining speeds of conventional machining is the heat generation from the cutting process. Generally, it is understood that increases in tool surface speeds produce increases in the cutting tool temperature. However, research in HSM from decades ago has shown that cutting tool temperatures begin to plateau and even decrease above particular cutting speeds [13] [14]

[15]. Figure 3 illustrates experimental studies from as early as 1931 [16] which reports that temperatures at the interface between the tool and chip begin to drop at increasingly higher speeds. Continued experimental investigations on this topic suggest that the heat generated by high-speed operation is largely dissipated with the ejection of the removed material or chips [17] [18].

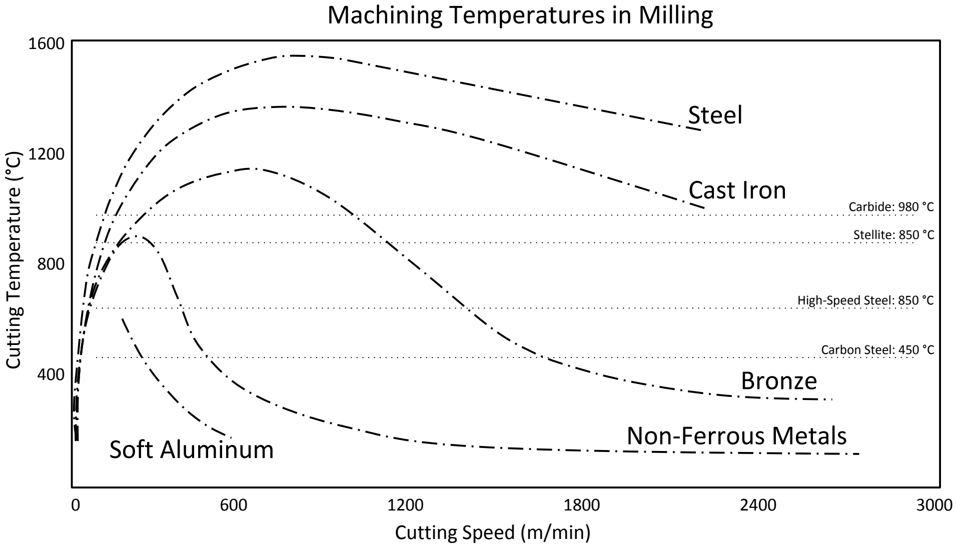

Figure 3: Cutting temperature trends with respect to cutting speed [16].

Using small diameter cutting tools and high feed rates, it is possible to machine intricate features which normally could only be done with other techniques such as Electrical Discharge Machining (EDM). This allows for elimination of many traditional steps to provide a much simpler and more efficient machining process.

The ability to produce thin walled features is possible due to the reduction in cutting forces which minimize tool and work piece deflection. An example of thin wall capabilities of HSM is shown on the left in Figure 4, illustrating the high quality surface finish and very straight, thin-walled features machined out of single pieces of aluminum [10]. Note that properly chosen parameters in the HSM process are essential; otherwise poor results will occur as illustrated in the right image of Figure 4.

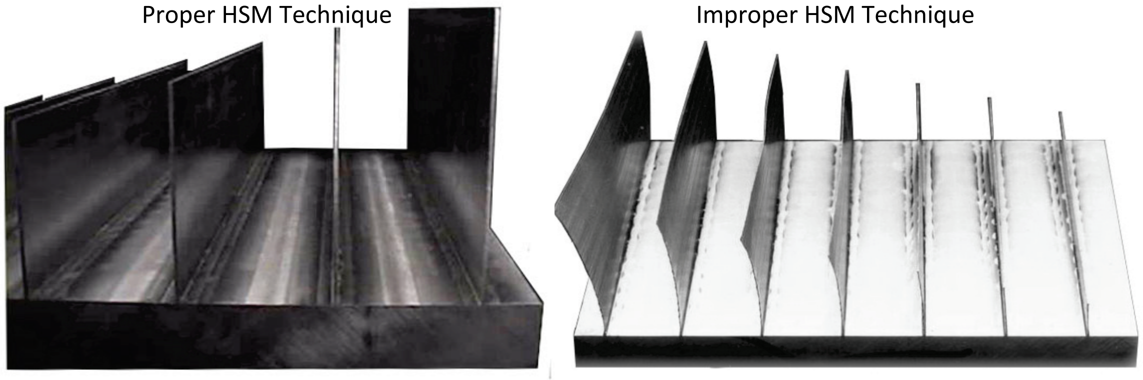

Figure 4: HSM thin-wall capability, good results (left) and poor result (right) [10].

Although the HSM offers many benefits which are advantageous over traditional machining methods, most of machine shops prefer continuing business with traditional machining methods. A completely revised philosophy is required to make the HSM practice work successfully. There are many considerations that require evaluation before employing HSM. A general-purpose HSM machine does not exist due to notable introduction of system dynamics, unique to each machining process [7], hence, necessitating the use of a machine that is built specifically for the particular application. Designers of the HSM machines take into account its intended use, which considers many parameters such as the type of part, part size, cutting tool speeds, and work piece materials [8].

As rotational speeds of a machine increase, the dynamics of both the machining spindle and the machined part become a significant consideration. In general, unwanted vibrations are the root of most dynamic problems that can stem from various sources in the machine. For example, a well-known and heavily researched dynamic problem in machining is known as *machining chatter*. As a result of machining chatter, the machined part does not have an acceptably smooth finish, and the spindle will endure excessive abuse. Chatter can be identified audibly as well as visually by the wavy surface patterns on the work piece.

1.2.1 **Introduction to High-Speed Machining Spindles**

The term *spindle* refers to the rotor assembly and its housing which is in many cases intended to be quickly replaceable within the HSM machining station. Machining spindles are often mounted within machining stations which maneuver the spindle and/or work piece with precise Computer Numerical Control (CNC). An example of a state of the art high-speed CNC machining station is shown in Figure 5. This is an advanced articulated robot built by Stäubli [19] which has an optional 42,000 rpm spindle. This high-speed machining station boasts a quickly replaceable spindle unit.

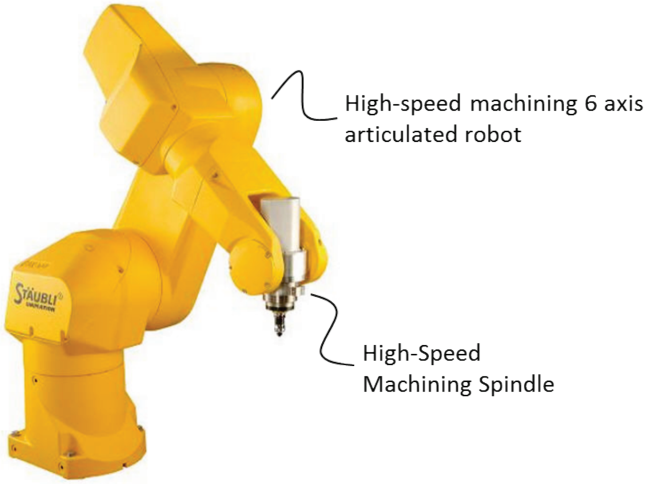

Figure 5: Stäubli high-speed machining 6 axis articulated robot pictured with a 42,000 rpm spindle option [19].

Most high-speed spindles retain similar constructions, consisting of the same basic components which include a spindle housing, rotating shaft, bearing system, integral drive motor, tool retention system, and cutting tool. Specialized HSM machining spindles from some manufacturers operate at rotational speeds of up to 200,000 rpm. Such high speeds are possible due to advances in bearing technologies found in rolling-element bearings, fluid film bearings, and Active Magnetic Bearings (AMBs). Typical high-speed spindle construction of a high-speed spindle is pictured in Figure 6 produced by Primero Machine Tools Corp [20].

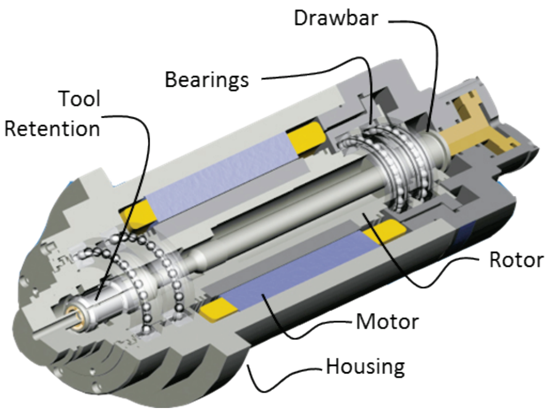

Figure 6: Cross section of high-speed machining spindle offered by Primero Machine Tools Corp [20].

Rolling-element bearings are far more common in HSM spindles than any other type. Angular contact ball bearings are often implemented due to their low-friction characteristics and ability to withstand external loads in both axial and radial directions [21]. Non-metal balls, made from silicon nitride, are commonly employed in high speed applications [22]. To categorize and define rotor's rotational speed properties for bearing application, a speed factor is defined and commonly used. The speed factor, DN (mm×rpm), is defined by the rotor's outside diameter multiplied by its rotational speed [13]. HSM spindles often run well above 0.5×10^6 DN, however, are most often limited by the physical limits of conventional bearings.

1.2.2 Design Challenges of HSM Spindles

The design of a high-speed spindle requires a compromise across several design areas to obtain a solution that meets the application's requirements in a cost-effective manner. Features that define the performance characteristics of a high-speed spindle are numerous and include power output requirements, expected loads, rotational speeds, and tooling requirements, to name a few. Further, reliability and maintenance programs are important topics to consider. A number of design challenges are mentioned below.

Powering the rotor to high speeds is limited to an integral motor solution. AC induction motors are utilized which eliminates the associated troubles and limitations of external belts and gears for power transmission. This type of electric motor is contactless and has high power density making it an ideal solution for powering machining spindles.

Prevention of spindle housing contamination from machining debris is a significant design challenge. Besides the inherent limitation due to high rotational speeds of the rotor, implementing seals for an AMB equipped spindle is additionally difficult since the seal has to accommodate the levitated and de-levitated state of the rotor. To resolve this problem, high pressure air is supplied to the spindle housing to maintain positive pressure, preventing contamination.

Tool retention systems are required to have automatic tool change capability for use in CNC machining stations. Developed standardized tooling styles exist and are required to meet strict specifications in terms of dimensional tolerance and balancing. A common method to retain the tool is with the use of a drawbar which extends through the entire hollow rotor. However, this is a potentially problematic construction when operating at high speeds due to unbalance issues. Rotordynamic effects like critical speeds should not reside in the intended operational range of the spindle. Large vibrations occur at resonance and require rotordynamic analyses to design around detrimental dynamics effects.

Bearings are often considered the limiting factor in rotational speeds of the rotor. Conventional contact bearings have speed limitations and may require complex lubrication and cooling strategies to inhibit wear and premature failure. The spindle rotor and its supporting bearings are engaged in a close relationship in terms of rotor geometry and bearing speed limitations in which compromises are required. An increase in rotor diameter provides improvements in rotor stiffness, however, also increasing the rotor speed factor, DN. Conventional spindle bearings are strictly limited to certain values of DN which in turn limits the maximum rotor diameter and rigidity of the rotor. The application of contactless bearings, such AMBs, minimizes this limitation and is discussed in subsequent sections.

1.3 AMB Levitated HSM Spindles

Magnetically levitated rotors benefit from a variety of advantages in comparison to rotors that operate on conventional bearings. Many considerable problems encountered by conventional bearing types can be minimized, if not completely avoided with appropriate utilization of AMBs. Relatively recent advances in high precision technologies as well as the explosion of digital computing have allowed for the rapid progression of active magnetic levitation of structures. Researchers continually apply active magnetic levitation technology to variety of fields due to the allure of contactless levitation. Despite of ongoing developments, there is still significant room for advancement, specifically when applied to high-speed, magnetically supported spindles.

The most noteworthy advantages of AMB levitated spindles over other conventional rotor suspension technologies are the much higher achievable rotor surface speeds and the variety of feedback control algorithms. Due to the higher achievable surface speeds, AMB levitated rotors can be built much more robustly in comparison to conventional spindles of similar rotational speed. The rotor surface speed in AMB spindles is limited by the rotor material's ability to resist failure due to the extremely high centrifugal forces acting on it. Feedback control systems for AMBs offer flexible possibilities in efforts to minimize vibrations which conventional spindle bearings lack [23]. In the case of machining chatter, control systems can be tailored to assist in the suppression of unwanted dynamics of rotating systems. These advantages over conventional spindle bearing technologies have potential for significant advancement in the field of HSM.

1.3.1 **Active Magnetic Bearing Background**

Although AMB supported spindles have not yet been well established in the HSM industry, AMBs for high speed rotating applications are being continuously researched as they offer many attractive features over conventional bearings. Over the past decades AMBs have become practical solutions to many design problems requiring a robust structural support such as in vibration isolation systems, compressors, turbines, pumps, motors, power generators, and even magnetically levitated trains. AMBs are inherently contactless, which greatly reduces bearing resistance and makes the need for lubrication and the problem of mechanical wear virtually nonexistent. This allows for higher bearing surface speeds; enabling spindle rotors to be much larger in diameter which directly increases robustness than with rotors operating on conventional bearings [24]. In addition, active control capabilities of AMBs allow for adjustments of stiffness and damping, unbalance compensation, active suppression of machining chatter, possibility of shaft path prescribing, and control of bearing dynamic characteristics [25] [26]. Many performance parameters can be specifically adjusted for the particular application. Rotating machines equipped with AMBs are capable of self system identification with utilization of existing AMB actuators and sensors. This proves to be useful in application of adaptive control to improve performance, increase reliability, and extend service life of the machine [27]. Many magnetic bearing systems can incorporate Active Vibration Control (AVC) capabilities which notably reduce vibration amplitudes in real time. Industries, as well as academia, continually present contributions to the field of magnetic bearing levitation, adding to its technological knowledgebase.

Despite the various benefits, there are a number of reasons industry refrains from implementing machines equipped with AMBs. First, the initial cost is relatively high due the plurality of components for the system, namely the bearing rotors, the stator and electromagnet, power amplifiers, and the digital control system. Further, specially trained personnel may be required to service or repair AMB systems. Other factors that initially may be unattractive include the relatively low specific load capacity of AMBs, the difficulty in achieving high bandwidth operation, and the challenge in control design complicated by complex spindle and machining dynamics [26]. The well-known and intuitive disadvantage of a magnetic bearing is that it is inherently unstable without active feedback [28] [29]. Active feedback is required for supporting and controlling a mechanical structure magnetically. In rotor systems, feedback is supplied to the controller by measuring the shaft position with displacement sensors. This allows for controlling rotor movement by generating the desired electromagnetic forces to displace the rotor to the required position [30].

Figure 7 presents the main components of an electromagnetic bearing and illustrates the function of a simple bearing for suspending a rotor in one axis. Initially, a displacement sensor measures the position of the shaft relative to a reference position. In order to return the rotor to the reference position, the controller calculates the required control signal necessary for this task. The controller sends the control signal to a power amplifier where it is then converted to a control current. This control current is directed to the coils in the electromagnet which generates the calculated magnetic field forcing the rotor to the desired position. Commonly in rotordynamic systems, this process occurs on the order of kilohertz. The feedback control law is responsible for stabilizing the rotor as well as the stiffness and damping properties of the suspension [31]. Within the feedback control law, it is possible to adjust the stiffness and damping properties during levitation.

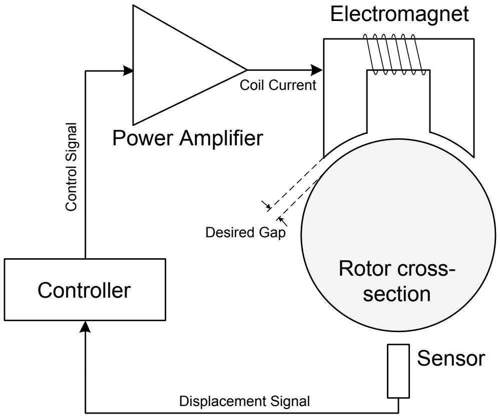

Figure 7: Basic AMB concept schematic.

Although AMB rotor systems are not subject to mechanical contact during operation, several types of energy losses still exist. Understanding their sources and magnitude is especially important in applications such as in flywheel or gas turbine technologies. Primary loss sources in AMB rotor systems are windage and electromagnetic losses. Windage loss is caused by the viscous effects of the surrounding fluid absorbing energy within the gap of the rotor and stator [32] in a non-vacuum environment. At very high rotor surface speeds, viscous friction greatly influences the rotor's outer surface temperature and the stator's inner surface temperature [33]. Although windage losses exist in conventionally supported rotating machinery, it has more presence in AMB systems due to much higher rotational and surface speeds. Losses due to magnetic hysteresis and eddy current loss are mitigated by material selection. Energy in form of heat is absorbed by the core material and then dissipated.

An ongoing issue in magnetic bearing design is non-collocation, as it's nearly impossible to co-locate the sensor and actuator. This is shown in Figure 8, where the magnetic actuator and sensor are not in the same axial plane. This separation distance, x_{nc}, is known as the amount of non-collocation in the magnetic bearing [34] and may be unavoidable due to physical limitations of the hardware. When the actuator and sensor are non-collocated, it is clear that the measured gap at the sensor will disagree with the real gap at the actuator to some finite extent. This is true for all cases of vibration except for the perfectly cylindrical rigid-body vibrational mode. Commonly in industry, once the levitated rotor system is ready for evaluation, engineers manually adjust active control settings to compensate for unpredicted instabilities. A vast amount of time is spent testing and fine tuning the magnetically levitated rotor system to meet some specified stability requirements [35].

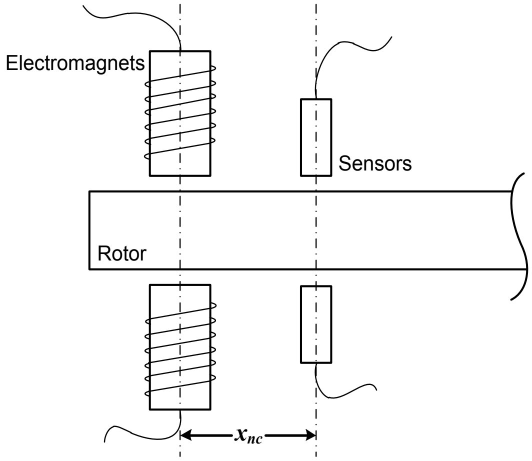

Figure 8: Illustration of non-collocation of electromagnets and sensors.

1.3.2 State-of-the-Art High-Speed AMB Spindles

Although rolling-element bearings are the dominating spindle rotor support type in the HSM spindle market, various companies produce AMB supported HSM spindles with great success. The many attractive advantages of this technology motivate companies to continue to heavily pursue and advance AMB systems. A few examples of HSM spindles using AMBs are presented.

Revolve Magnetic Bearings Inc., a division of SKF group, produces a line of precision spindles named Hyperspin™. These magnetic bearing spindles are applied in various applications such as turbomolecular pumps, neutron choppers, hydrogen circulators, and grinding spindles. These spindles can operate at 60,000 rpm at 900 W using synchronous motors and 50,000 rpm at 10 kW with asynchronous motors. There are base models which require the selection of various options before purchase such as cooling method, cable length between spindle and control system, and what type of payload will be attached. The payload attached directly to the Hyperspin™ shaft which uses a standard taper interface. They also offer customized extensions to suit other attachment methods such as welding, interference fits, and tapered locking elements [36]. Several accessories exist such as the MB Controller for magnetic bearing control, MBScope™ which is a software suite of easy-to-use graphical tools providing access to diagnostic information, and various machine cables for carrying power and signals between the spindle and control system. Figure 9 illustrates some of the spindles in the Hyperspin™ series.

Figure 9: Hyperspin™ magnetic bearing spindles from Revolve [36].

IBAG Switzerland AG is an AMB machine tool spindle manufacturer. Figure 10 pictures one of the high performance AMB spindles they produce [37]. This model is rated to have a torque of 1.5 Nm at 70,000 rpm and 11 kW.

Figure 10: IBAG magnetic bearing spindle [37].

S2M is a manufacturer of magnetic bearings and high-speed motors. AMBs manufactured by S2M are commonly sized to fit shafts from 50 mm to 400 mm in diameter, in addition to special application which require AMBs to fit shafts well outside this range. High speed motors are produced that cover a power range of up to 500 kW with speeds up to 120,000 rpm. An example applied to HSM is a heavy duty machine tool spindle that is capable of running 30,000 rpm at 70 kW on magnetic bearings. Figure 11 shows a robust machine tool spindle that was put to a crash test at the ENIM laboratory in France in 2001. The crash test consisted of direct penetration of a 25 mm diameter milling tool into aluminum at a feed rate of 10 m/min. This is reportedly an extremely severe event for a machine tool spindle to endure, simulating possible extreme operating conditions or an accidental maneuver in high-speed machining centers. The spindle, shown in Figure 11 was restarted immediately to continue machining and showed no signs of damage to the spindle hardware [38].

Figure 11: S2M magnetic bearing machining spindle [38].

Most companies, however, manufacture AMBs for a broad spectrum of applications, not limited to HSM spindles. For example, Mecos Traxler AG, S2M, Synchrony, SKF, and Waukesha are companies that apply this technology to various fields. Mecos Traxler AG reports magnetically levitated machines such as turbomachines, centrifuges, machine tool spindles, and flywheels that can operate in excess of 100,000 rpm. They produce magnetic bearing systems for industry which include built-in diagnostics capabilities for problem diagnoses and preventative maintenance [39]. Synchrony produces various lines of AMBs. The Synchrony Fusion® series is an AMB that is reportedly the first time an active magnetic bearing fully integrates the control system within the actual bearing structure. This allows for the simple integration into many existing applications without separate controller cabinets [40]. Waukesha produces custom designed AMB bearing solutions for various demanding applications. Particular specialties include applications where bearings are immersed in the process fluid such as in sea water for extended periods of time [41].

Figure 12: AMBs produced by Mecos, Synchrony, and Waukesha [39] [40] [41].

1.4 Statement of the Problem

The focus of this dissertation was to develop the correct rotordynamic model of the high-speed AMB levitated machining spindle. The spindle prototype used in this study is located in the Center for Machinery Dynamics and Control at Cleveland State University and was manufactured by Revolve Magnetic Bearings, Inc., a subsidiary of SKF Group. The requirement for accurate spindle modeling is dictated by the synthesis of robust Multiple-Input Multiple-Output (MIMO) controllers, which inherently rely on the plant model. For successful implementation of MIMO controller for this spindle system, a methodology was needed to correct the nominal spindle model in terms of its physical and dynamic properties to coincide with experimentally extracted MIMO transfer functions. The dynamic characteristics that quantified the difference between the experimental data and the model were its resonance frequencies and mode shapes. The final updated spindle model was verified with experiments that confirmed its capability to successfully fulfill its duty as an accurate spindle representation.

1.5 Organization of Dissertation

The structure of this dissertation first introduces the reader to the smart machining system initiative. There is an enormous number of subtopics bounded by this area of research, too many to describe in detail. Hence, this work quickly narrows the subject matter down to the significance of high-speed machining with magnetically levitated spindles and the motivation for its successful implementation. Design challenges of high-speed machining spindles prompts for further investigation of the state-of-the-art technology for enabling advanced high-speed rotor performance. Chapter I concludes with the statement of the problem.

Chapter II describes the experimental setup and hardware that was studied and utilized in this work. In particular, the spindle rotor's complexity is described and supported with illustrations of its various components. MIMO system identification procedures and results are illustrated followed by more specific interpretation of several features observed in the frequency domain.

Chapter III assembles a nominal open-loop spindle model with comparisons with open-loop experimental system identification data. Model updating procedures are described with final model results presented. Several experiments were performed and compared to simulations to assess the predictive aptitude of the updated model.

Chapter IV validates the updated model through implementation of the μ-synthesis controller design strategy. This inherently model-based controller synthesis methodology was demonstrated experimentally to validate that the model is in fact representative of the real system. Measurements and simulations of the dynamic stiffness at the spindle's tool location are compared. Tool orbit measurements were acquired to accompany the dynamic stiffness measurements.

Chapter V summarizes the results and concludes the work presented in this dissertation.

CHAPTER II

EXPERIMENTAL HSM AMB TEST PLATFORM

2.1 Overview of HSM Station Hardware

The experimental test rig seen in Figure 13 is located in Cleveland State's Center for Rotating Machinery Dynamics and Control (RoMaDyC) [42]. This prototype spindle system is a high-speed machining station with an AMB supported high-speed spindle rotor, complete with support structure, and motorized chuck. This HSM station is designed to machine the inner surfaces of a preexisting hole within a work piece. The test rig is enabled for controls oriented research activity by providing access to the AMB and sensor signals via a dSPACE digital interface. This access allows for research and development of advanced control strategies as well as for the possibility of developing advanced features such as AVC or even chatter suppression in machining.

The supporting frame is built from standard 3 in square tube steel which has a footprint of roughly 6.5 ft by 2.5 ft. The machining area (spindle and chuck) is safely enclosed by a protective housing constructed from extruded aluminum framing and clear plastic walls to prevent escape of debris during the machining process.

The remotely controlled motorized work piece holder consists of a chuck, chuck mount, and a motorized linear translation stage. The self-centering six-jaw chuck is used to hold the work piece concentric to the spindle rotor and is mounted on a motorized translation stage. The translation stage, manufactured by Parker Hannifin, has an operation range of 500 mm. A custom stage controller system for this stage has been built and is used to direct stage movements following a given set of predefined distances and velocities.

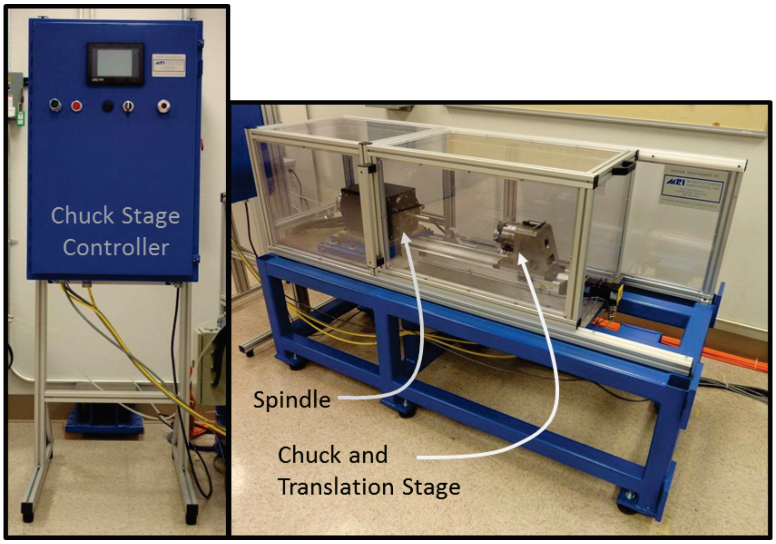

Figure 13: AMB HSM station with chuck stage controller.

The control center (see Figure 14) for the spindle is housed within a cabinet that contains a magnetic bearing controller (MBControl™ from SKF), a breakout module (MBResearch™ Module from SKF), a dSPACE module, and an Amplifier Chassis (MB12400 from SKF). The MBControl™ box is a digital, magnetic bearing controller which features five differential sensor channels, five axis levitation control, ten bearing amplifier channels, auto ranging 300 W power supply, and discrete I/O for custom logic interface [43]. In order to provide current to the electromagnet's coils, this system is combined with bearing amplifiers and an amplifier power supply. The MBResearch™ box is a BNC connector-based breakout module that provides access to signals from Revolve Magnetic Bearings Inc.'s line of magnetic bearing controllers. The signals available include analog current and position signals, and a Top Dead Center (TDC) pulse signal for monitoring speed and phase [44]. The Amplifier Chassis MB12400 drives two radial bearings and one double acting thrust bearing utilizing a total of ten amplifiers. This system has been specifically designed for use with MBControl™ system. The amplifier voltage is determined by the DC power supply and can operate between 100 and 400 VDC. Each amplifier can deliver up to 400 V at 12 A [45]. A dSPACE module is installed that allows for manipulation of signals injected and received by the controller. The computer that interfaces the components is a rack mount P4 3.0 GHz PC.

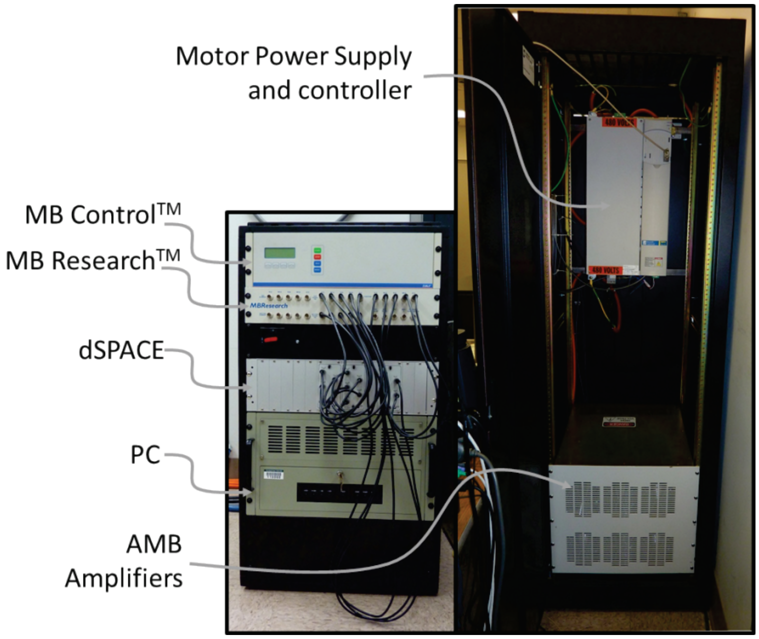

Figure 14: AMB control center and power supply.

2.2 HSM Spindle

The spindle is developed by Revolve Magnetic Bearings, a subsidiary of SKF, Inc and is pictured in Figure 15. It is supported by two radial AMBs and one thrust AMB and is designed to operate at a maximum speed of 50,000 rpm. The AC asynchronous induction motor rotor is located between the thrust bearing and the rear bearing. The maximum static radial loads that the front and rear AMBs can support are 1,400 N and 600 N, respectively. The thrust bearing can support a maximum static load of 500 N. In the de-levitated state, the rotor rests on backup ball bearings which have a radial clearance of 254 μm. Full contact seals between the rotor and the spindle housing are not possible, so to prevent internal contamination, positive air pressure is provided using shop air at approximately 100 psi. Water cooling is integrated into the spindle housing to remove heat generated by the high current components such as the induction motor and electromagnets.

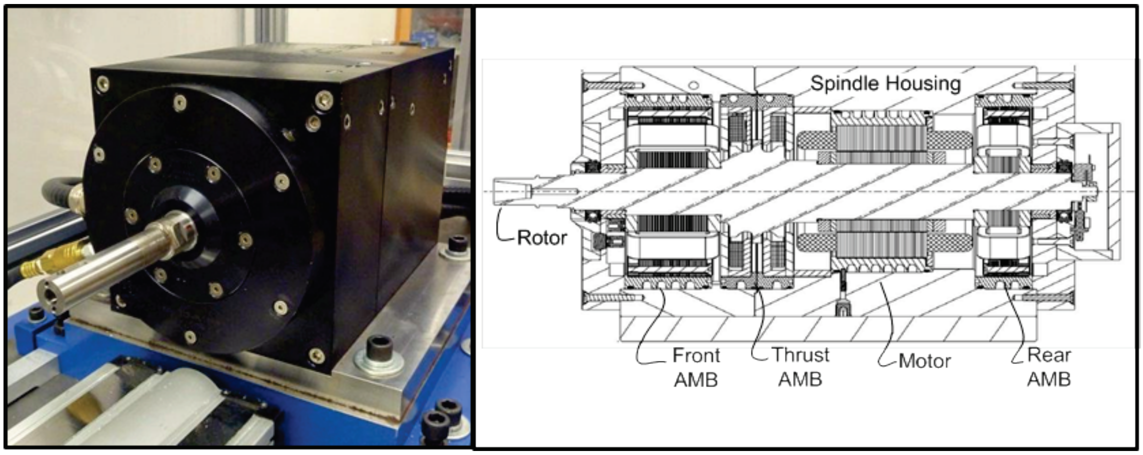

Figure 15: AMB HSM spindle at Cleveland State's RoMaDyC laboratory, photo and cross-section.

2.2.1 PID Controller

The Proportional-Integral-Derivative (PID) controller was used in this test rig to perform system identification of the levitated spindle and also to complete updated model assessment tasks. In previous works in the RoMaDyC laboratory, the controller successfully maintained rotor levitation up to the maximum running speed of 50,000 rpm. The PID controller strategy is inherently SISO so each of the five AMB axes in the spindle operates independently to drive sensor readings at zero. The first four axes of control are for the radial directions of the front and rear AMBs. The fifth axis is the thrust AMB and was not changed throughout this work. Presented later in this work, the

PID controller of the four radial axes was replaced with an advanced MIMO controller for updated model validation and performance comparisons.

2.2.2 **Spindle Rotor**

A photo of the spindle rotor is shown in Figure 16 without the 65 mm tool holder attached. The rotor does not utilize a drawbar like most spindles do for tool retention; instead, the tool holder is mounted on the end of the rotor shaft utilizing a tapered fit connection and a retaining screw. The tool bit (as well as a counter weight) is attached near the end of the tool holder and held in place with set screws. The rotor itself is solid with the exception of the tool holder collet. The spindle rotor is 6.91 kg in mass and 465 mm in length with the tool holder attached. The rotor shaft is fabricated from 4140 steel, however, the bearing and motor components are more complex and are shrunk fit to onto the rotor shaft.

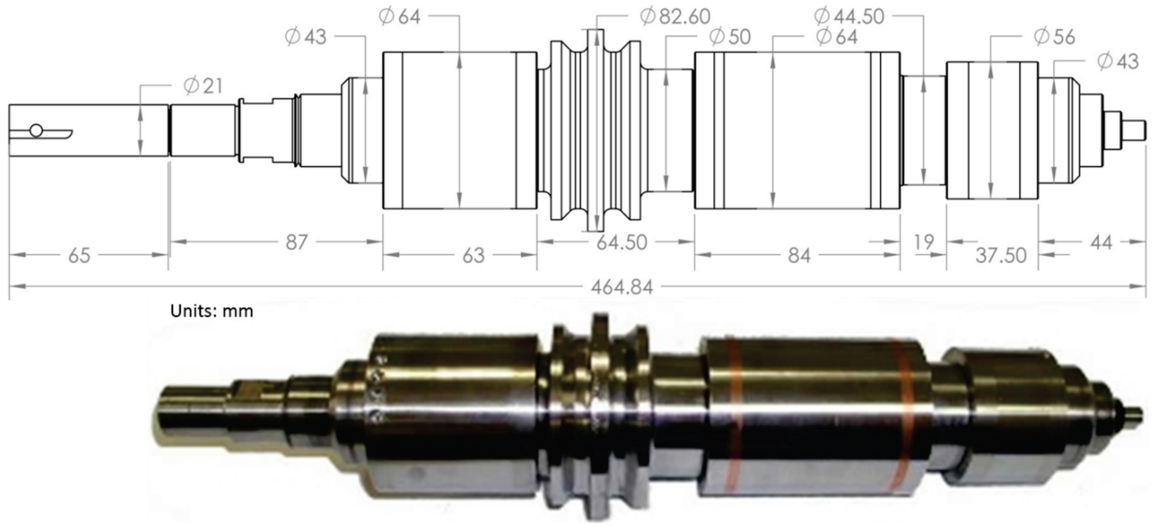

Figure 16: Basic dimensions and photo of the rotor (65 mm tool holder not shown in photo).

The bearing rotors are constructed from the Hiperco® 50 alloy which is designed to exhibit higher mechanical strength and the highest magnetic saturation relative to other soft magnetic metals. Materials of this type are demonstrate high permeability, low losses, and low residual magnetism and are primarily used in the manufacture of rotor and stator laminations in motors, generators, magnetic bearings, and other high magnetic flux machines. Hiperco® 50 is manufactured in sheets which are later laminated to create magnetically sensitive products. The purpose of lamination is to minimize heating and magnetic loss effects due to eddy currents. Titanium keeper rings are also incorporated to the ends of the bearing rotors. When assembled, the resulting AMB rotors exhibit inhomogeneous material properties which are assumed a source of error in modeling. The AC asynchronous induction motor is rated to perform at 50,000 rpm drawing 10 kW of power. The induction motor rotor is built based on squirrel cage construction typical of AC asynchronous induction motors. The copper rods and two copper short circuit rings are embedded within iron laminations. Benefits of induction motors are that they are contactless, wear free, require virtually no maintenance, and have high power density. Similar to the bearing rotors, this component is structurally ambiguous and introduces error to the model. The tool holder is fabricated from Ti-6Al-V and is mounted to the shaft via a tapered fit collet which is held in with a bolt torqued to prescribed specification. The structural properties of the tapered collet connection are not clearly defined and present modeling ambiguity.

Each of the aforementioned components introduces difficulty in estimation of nominal structural properties of the rotor. To further augment the problem of structural ambiguity, the AMB and motor rotors are shrunk fit to onto the rotor shaft. This is done by expanding the rotors by heating while simultaneously shrinking the shaft by cooling, followed by final assembly. When assembled, temperatures of all components equalize to ambient which naturally fastens the assembly together. The estimated material interference between components is approximately 80 μm which produces the pre-stress required to overcome the effect centrifugal expansion at high speed rotation. The addition of the shrunk-fit AMB and motor rotors has an unclear effect on the global stiffness of the spindle rotor which is difficult to quantitatively predict. This is due to a variety of factors such as uncertain friction between components during bending, undefined magnitudes of pre-stress induced change in material stiffnesses, and non-uniformity in mating surface tolerances.

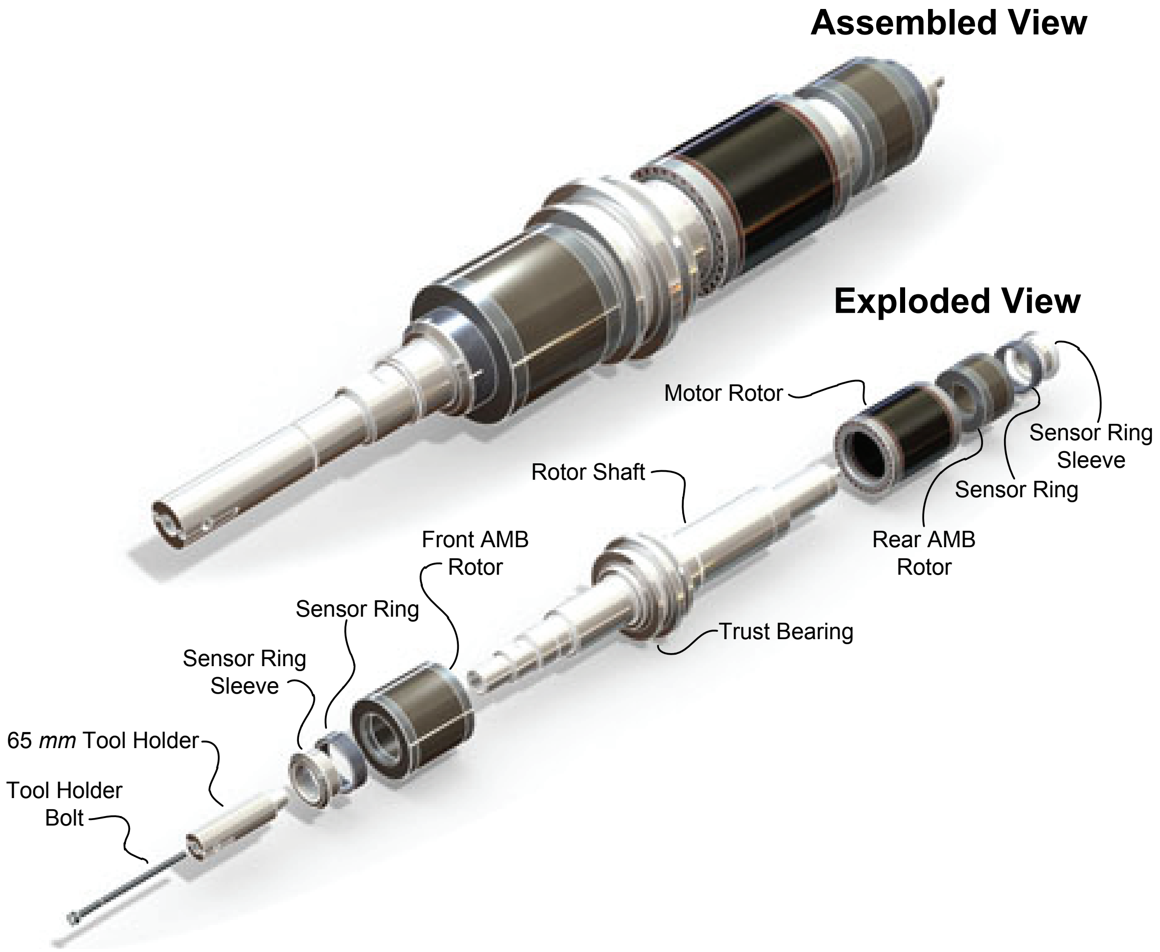

Figure 17: Assembled and exploded views of the spindle rotor.

2.2.3 **Spindle Tooling**

Tools used in HSM are required to be the extremely hard, wear resistant, and durable in order to endure the HSM action. The tool bit used in this test rig is made from Poly-Crystalline Diamond (PCD) manufactured by SilverHawk Precision. It is a model P705231801A pin bore tool that mounts to the end of the tool holder shaft using a set screw. Since only one bore tool is needed in this spindle for machining, a counter weight is attached to the other side of the tool holder shaft to maintain balance. A photo of the tool is shown in Figure 18.

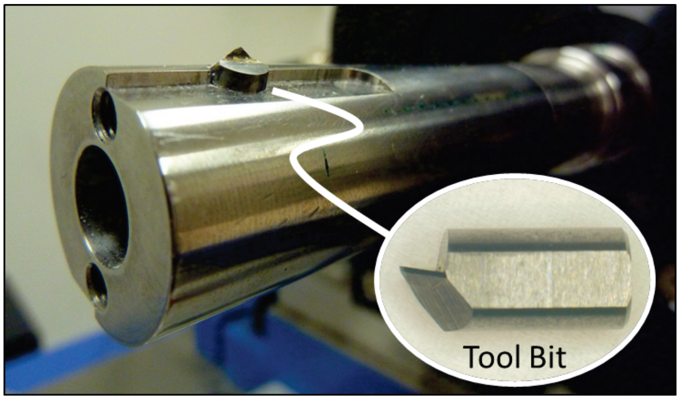

Figure 18: Photo of tool holder and tool bit.

2.3 System Identification

Open-loop system identification was required in defining the spindle system dynamics for use in open-loop and subsequent closed-loop spindle modeling. In this work, an in-situ testing method was implemented, utilizing only the existing AMB hardware for data acquisition. The spindle rotor was never removed for independent free-free rotor testing. In-situ open-loop transfer functions were measured [26] in the non-rotating, levitated state using the simple PID controller. The transfer function measurements are referred to as open-loop because the feedback effects of the spindle's PID controller were omitted. Open-loop system identification measurements characterized the dynamics of the spindle components that were seen by the digital controller such as the rotor, AMBs, power amplifiers, sensors, A/D and D/A convertors, etc., as illustrated in Figure 19. It should be noted that the spindle rotor in this system plays the dominant role in the open-loop system dynamics.

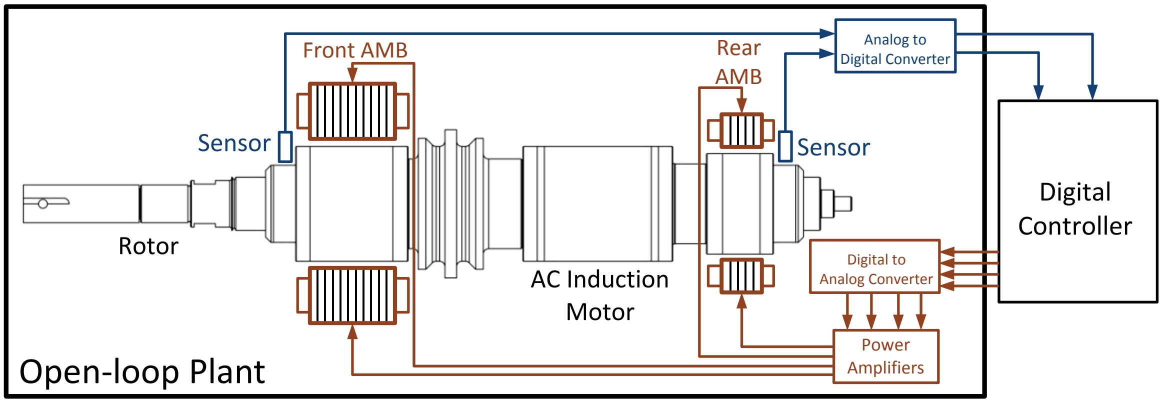

Figure 19: Diagram of system structure in a single plane.

The motivation for in-situ testing was to circumvent the removal of the spindle rotor. Disassembly of machinery can be a laborious, time-consuming procedure which may not be an appealing option in some industrial applications. However, the advantage of removal and isolation of the rotor is that transfer function measurements would be representative of the standalone rotor, which would allow for modeling much simpler, free-free rotor configuration.

Rigid-body modes are normally understood to exist at 0 Hz for both the cylindrical and conical modes; however, when levitated under feedback control, they are referred to as bearing modes and have a frequency value other than zero. This is typical to AMB levitated systems due to the combination of inherently low support stiffness of the AMBs at low frequencies and the presence of rotor mass. A sample data set in Figure

20 illustrates the dissimilarity between the open-loop and closed-loop transfer functions measured at the front AMB. The rotor's flexible modes were nearly identical since feedback control has less effect on the higher (flexural) natural frequencies. The difference was observed in the controller feedback effects which were dependent on the PID controller and independent of the rotor's flexure.

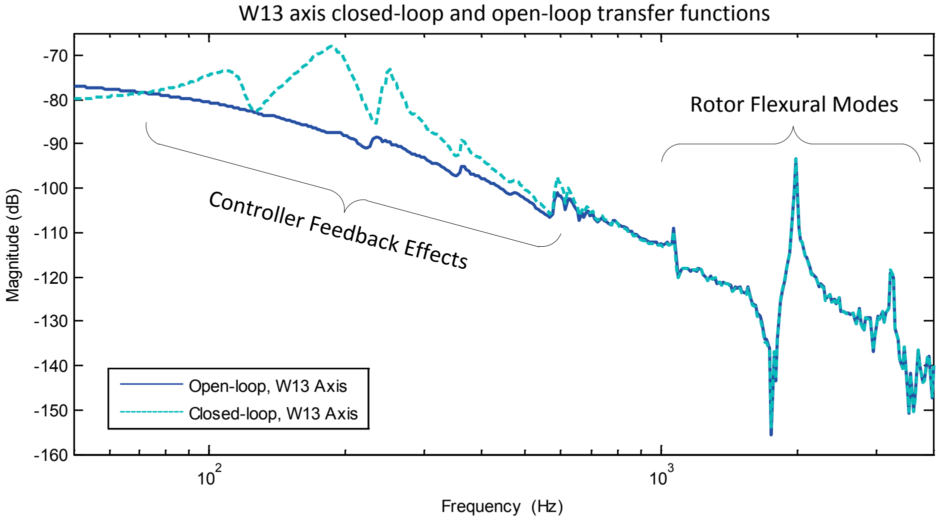

Figure 20: The dynamics of controller feedback were minimized in the open-loop transfer function measurements.

The existing spindle AMB hardware was utilized for transfer function measurements. This eliminated the need for implementation of external excitation and measurement hardware. During rotor levitation with PID control, force excitation was delivered by the AMB bearings meanwhile recording rotor response with the associated AMB eddy current sensors. A simple SISO transfer function was possible in this way; however, by employing the full set of four radial AMB axes, the assembly of a MIMO transfer function was achieved. The advantage of a MIMO transfer function is that it contains cross-coupled dynamic information across all four radial control axes. Figure 21 illustrates the rotor's coordinate system, namely the four axes that were used in open-loop MIMO transfer function calculation. The thrust bearing was not included in the analyses because the axial responses were assumed to have negligible impact on the spindle's lateral dynamics considered in this work. Throughout this work, the plant was assumed to operate linearly for small displacements.

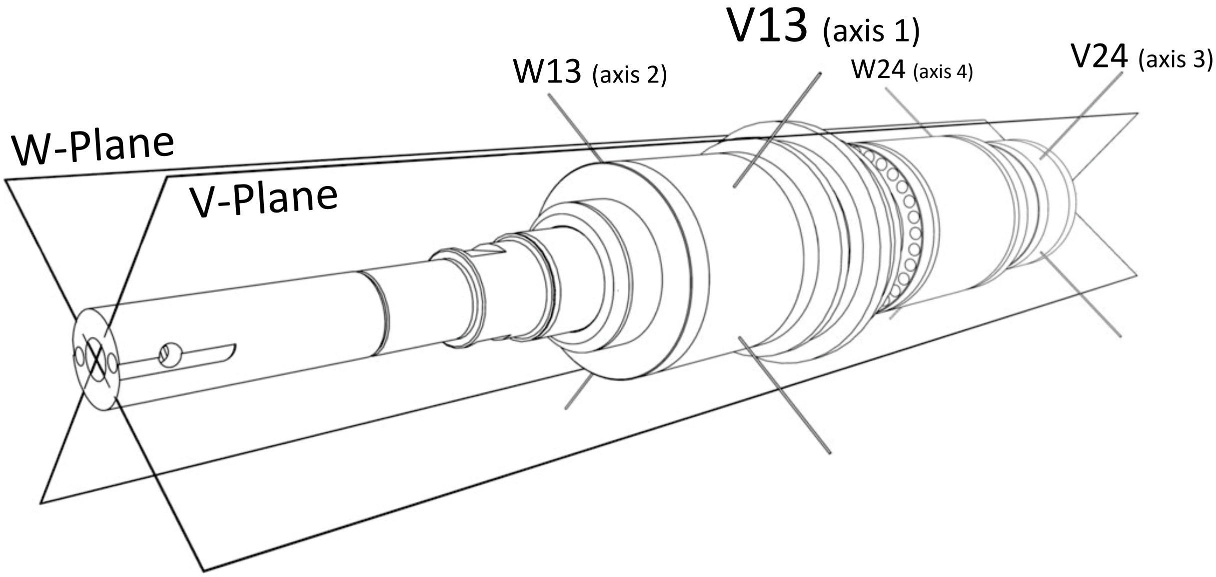

Figure 21: Rotor coordinate system defined.

One at a time, a sine sweep perturbation signal, u_i, was injected sequentially into all four AMB axes. During each sine sweep perturbation, all four AMB sensor signals, y_j, were recorded. Here, subscripts i and j represent integers from one to four corresponding to the input axis and output axis, respectively. In this way, four measurements were recorded per one axis of signal injection. Since injections were carried out for all axes, a total of 16 transfer function measurements were recorded. This is expressed in Equation (1) where **G**(*s*) is a 4×4 matrix of transfer functions.

$$\mathbf{y}_j = \mathbf{G}(s)\mathbf{u}_i \tag{1}$$

At each frequency of the sine sweep, Fourier coefficients, $\mathbf{U}(\omega_f)$ and $\mathbf{Y}(\omega_f)$, were measured for each of the four perturbation inputs and sensor response outputs. Here, subscript, *f*, represents discretized frequencies throughout the sine sweep signal input.

$$\mathbf{U}(\omega_f) = \left[U_{ij}(\omega_f)\right]_{i,j=1\ldots4} \qquad \mathbf{Y}(\omega_f) = \left[Y_{ij}(\omega_f)\right]_{i,j=1\ldots4} \tag{2}$$

In this way, the signals are related by the expression in Equation (3).

$$\mathbf{Y}(\omega_f) = \mathbf{G}(j\omega_f)\mathbf{U}(\omega_f) \tag{3}$$

To extract the open-loop transfer function, simple arithmetic was carried out to obtain Equation (4).

$$\mathbf{G}(j\omega_f) = \mathbf{Y}(\omega_f)\mathbf{U}^{-1}(\omega_f) \tag{4}$$

Figure 22 illustrates all 16 experimental open-loop TFs. The Bode plots are ordered in a similar fashion as matrix elements, Bode$_{ij}$, arranged based on injection inputs and response outputs. Note that the principal diagonal contains TFs where the injection and measurement axes are coincident and thus tend to show the highest gains and most clear resonance and antiresonance peaks.

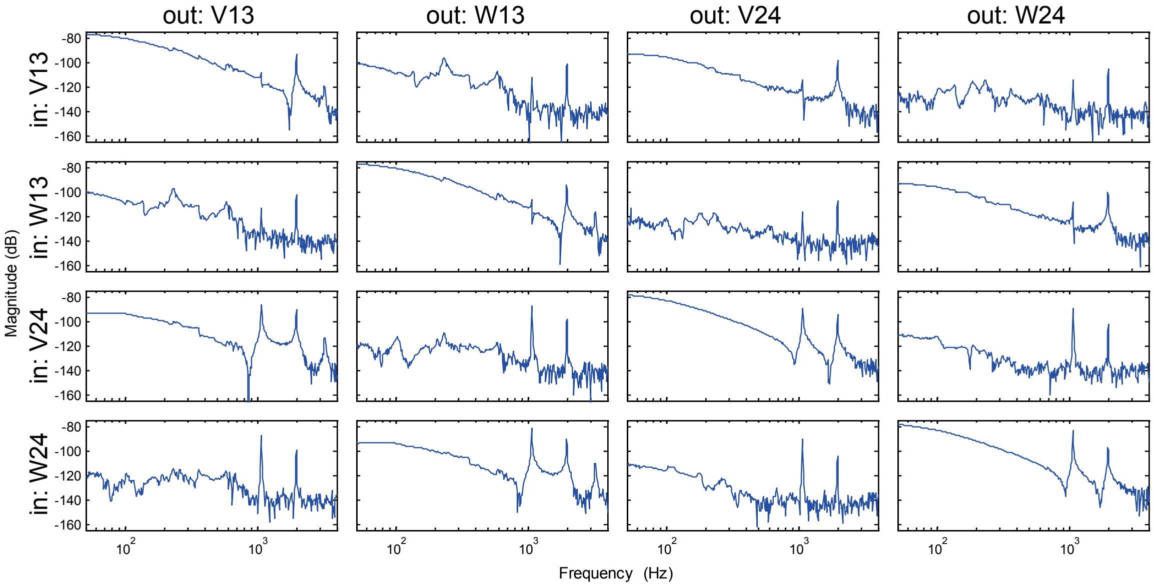

Figure 22: Bode plots of all 16 open-loop transfer functions.

The transfer function measurement frequency range was from 50 Hz to 4000 Hz, capturing the first three resonances of the rotor; 1069 Hz, 1955 Hz, and 3210 Hz. The measured resonance frequencies are alike for all the Bode plots. The antiresonances vary from plot to plot and contain useful information representing mode shapes.

2.3.1 **Interpretation of Antiresonance Peaks**

A case study based on this spindle was performed, with focus on the first flexural mode at the spindle's front AMB. First, the purpose of this investigation was to correlate antiresonance information in the frequency domain (from Bode plots) with rotor's flexible mode shapes in the spatial domain. Commonly, interpretation of antiresonance information is entirely ignored in system identification, which sacrifices spatial response information. Secondly, the location of the bending node (of the spindle rotor's first flexural resonance at the front AMB) has historically been a difficult feature to model correctly in this AMB spindle. Special attention was given to the location of this bending node because it resides between the front AMB's sensor and actuator due to the AMB's non-collocated nature. This is inherent in the design of the rotor and cannot be changed without physical modifications of the spindle.

Interpretation of the antiresonances (also known as transmission zeros) in a Bode plot provides insightful information regarding the flexible mode shapes of the rotor [46] [47] [48]. The location of an antiresonance peak relative to its corresponding resonance peak provides an indication of the spatial location of the rotor's bending nodes. The bending node of the rotor refers to the axial location where there exists virtually no measured radial displacement during the excitation of a given flexible mode. Note that torsion is not considered in this work.

Figure 23 illustrates the simulated comparison of an array of rotor models which were derived from the model updating methodology presented later in Section 3.2. This section does not provide details on this topic. The models plotted in the figure were *updated* to maintain the correct values for the first three rotor resonance frequencies as well as the second two antiresonance frequencies in the Bode plot. Note that the first antiresonance is not fixed. The array of models were generated in such a manner that allowed the first antiresonance frequency of Bode_{22} to progressively pass through a prescribed frequency envelope, passing the corresponding first resonance frequency as shown in the open-loop transfer function. Each rotor model is designated with a color which is consistent between the top and bottom plots.

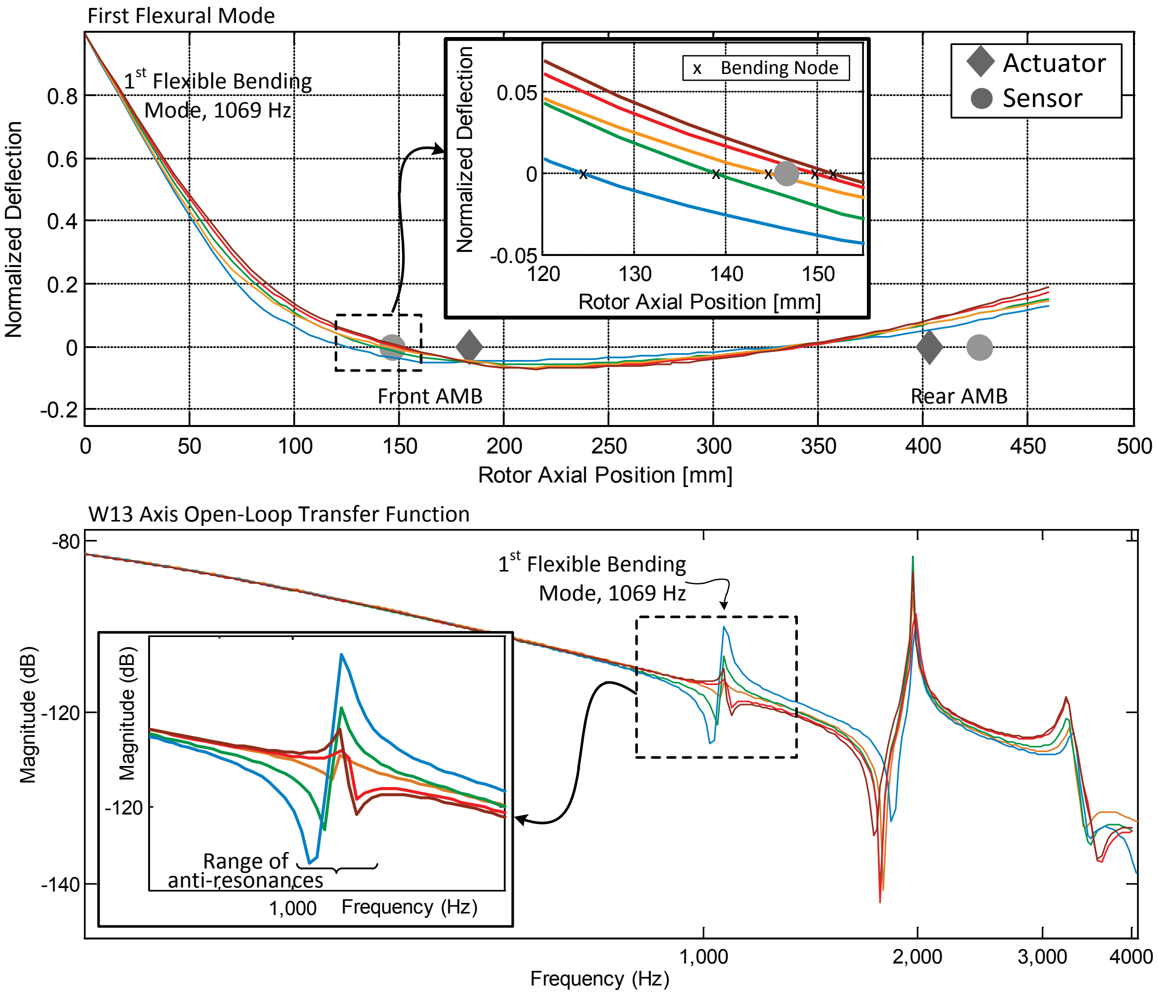

Figure 23: An array of rotor models with varying 1st antiresonance (bottom), directly correlated to the bending mode (top) of at the front AMB in Bode$_{22}$.

Initial inspection suggests that the front bending node (of the first bending mode) is located near the sensor or actuator due to the relatively low response amplitudes of both the resonance and antiresonance peaks. A bending node near the actuator location will limit the AMB's controllability of rotor vibration. Similarly, a bending node near the sensor will limit the controller's observability of the rotor vibration. Further information was interpreted from the location of the antiresonance peak relative to its corresponding resonance peak in the frequency domain. Since the sensor and actuator are inherently non-collocated, the antiresonance peak location switched from the left side to the right side of the corresponding mode's resonance peak just as the bending node crossed the sensor location in the mode shapes plot. The location of the bending node determines whether the antiresonance peak will precede or follow the corresponding resonance peak. If the bending node falls between the sensor/actuator pair, the antiresonance peak follows the corresponding resonance peak; otherwise, it precedes the corresponding resonance peak. This interpretation applies to all bending modes and transfer function plots throughout this work. For example, through observation of the experimental open-loop transfer function in Figure 23, it is clear that the bending node of the second bending mode does not fall between the sensor/actuator pair at the front AMB because the corresponding antiresonance precedes the corresponding resonance peak. However, since the third antiresonance is located immediately after the third resonance peak, the bending node of the third bending mode is located between the sensor/actuator pair in the front AMB. This is visible in the updated model mode shape plot in Figure 34. A complete measurement of the mode shapes is not possible in most experimental applications which emphasize the importance in the intuitive understanding of the antiresonance peaks from experimental system identification plots.

Figure 24 illustrates two Bode plots extracted from the complete MIMO transfer function in Figure 22. Note that $\hat{\omega}_{ij,k}$ and ${}^{a}\hat{\omega}_{ij,k}$ are the experimental values for resonances and antiresonances, respectively, where subscript k denotes the corresponding flexural resonance or antiresonance peak number. The subscripts i and j reference the corresponding Bode plot's input and output axes, respectively. These two Bode plots were utilized throughout this work and illustrate the where their inputs and outputs are relative to the spindle rotor on the *W*-plane. Through interpretation of experimental data (Bode$_{22}$ and Bode$_{44}$) in Figure 24, it was determined from Bode$_{22}$ that the spindle rotor has a bending node between the front sensor and front actuator for the first resonance frequency. This was identified by the antiresonance peak $^{a}\hat{\omega}_{22,1}$ located immediately afterward the corresponding resonance peak $\hat{\omega}_{22,1}$. The relatively low response amplitudes are typical to measurements near a bending node and support this observation.

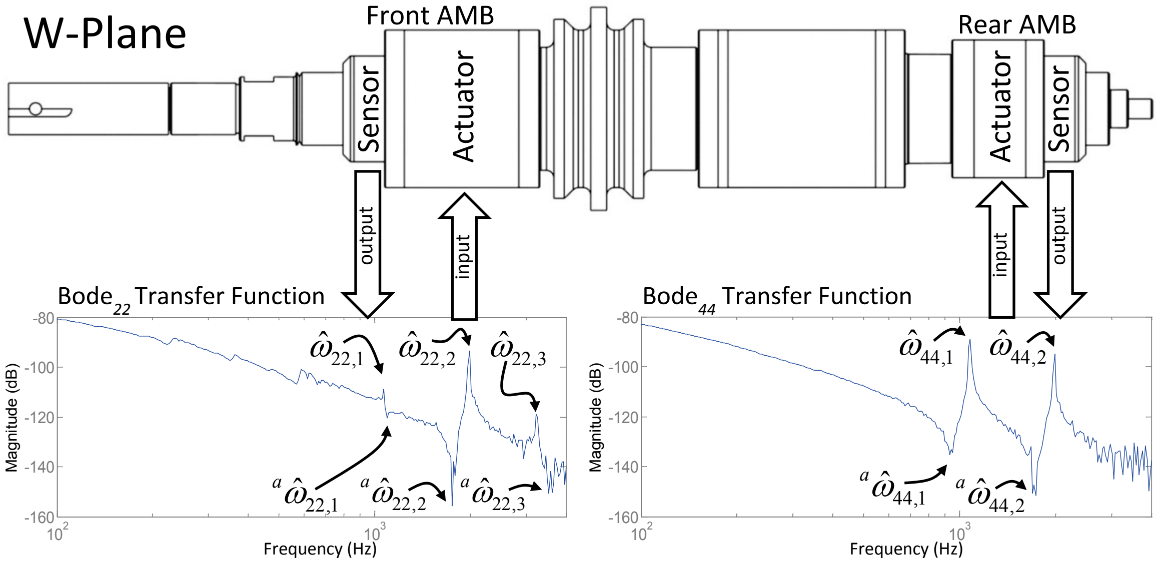

Figure 24: Bode$_{22}$ (left) and Bode$_{44}$ (right), indicate a bending node between sensor/actuator pair of the front AMB for first and third bending modes due to antiresonances immediately following their corresponding resonance peaks.

This observation is applicable to the remaining flexible modes as well. Bode$_{22}$ exhibits an antiresonance peak $^{a}\hat{\omega}_{22,3}$ following the third resonance peak $\hat{\omega}_{22,3}$ which is indicative of a bending node between the sensor/actuator pair. Figure 34 is the simulated mode shape plot for the updated open-loop model in which this can be observed for the third flexural mode.

Similarly, Bode$_{44}$ exhibits nearly no response for the third flexural mode. This indicates the existence of a bending node of the third flexible mode near the actuator or sensor, which is unknown from the Bode plot in this case. For the case when a bending node is coincident with the actuator, the actuation is not enough to significantly displace the rotor. Conversely, for the case when a bending node is coincident with the sensor, nearly zero displacement is registered. Through observations of the updated model's mode shapes in Figure 34, it is shown that the bending node for the third flexural mode is nearly coincident with the rear magnetic actuator, preventing any significant excitation.

CHAPTER III

HSM SPINDLE MODELING

3.1 Introduction

Spindle modeling was completed in open-loop and closed-loop form like seen in the diagram in Figure 25. This open-loop spindle model was then compared to system identification data for accuracy evaluation. Throughout this work, the open-loop plant did not change properties, so one set of open-loop transfer function data was necessary to derive one final updated open-loop model. The focal point of the spindle was its performance at the tool, which would potentially reflect the quality of machining operations in future studies. For this reason, model assessments were performed at the tool location to evaluate the predictive aptitude of the updated model under various disturbances. Assessments of the updated model were performed in closed-loop form at the tool location, which was completely independent of locations where system identification data was acquired. The same P, I, and D parameters that were used in the initial levitation of the rotor were applied in the PID model of the closed-loop system.

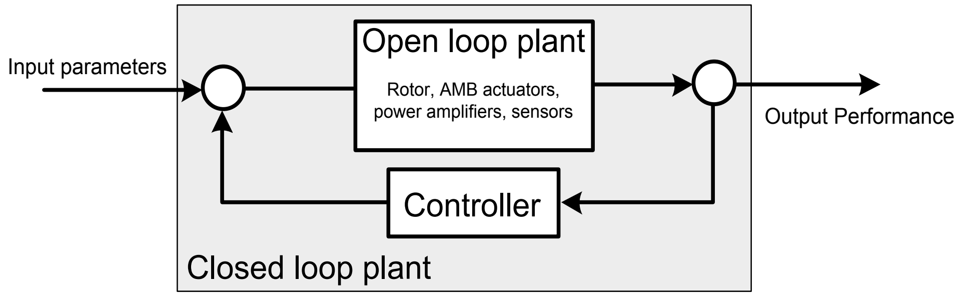

Figure 25: Open-loop and closed-loop diagram.

Although control strategies were not discussed in detail, substantial motivation for the derivation of an accurate spindle model stems from the MIMO robust control requirements. Robust control, and particularly for MIMO systems applying μ-synthesis control, is heavily model-based. This is often a significant drawback [49] [50] due to the difficulties in open-loop plant modeling. With this type of control, uncertainties are defined based on the presumption that various parameters are not accurately defined in the plant model. Plant modeling error is often a considerable source of uncertainty estimation for robust control design, which can be significantly minimized with an accurate and also validated plant model. Reducing the plant modeling uncertainty increases the effectiveness of robust controller calculation routines.

The open loop-plant is composed of a multitude of components, however, in the spindle system studied here, only the dominant components were considered in the open-loop model. Although the spindle rotor is the dominant component of the plant's frequency response, the amplifier model and AMB parameters were also included to complete the open-loop plant.

3.1.1 **Rotor Model**

The nominal spindle rotor model is a simplification of the real rotor. The real rotor is difficult to accurately model due to its elaborate geometry and complex structure. More specifically, modeling difficulties were found to be in the structural properties of the laminate materials in the AMB/motor rotors, the shrink fit interfaces, and the tapered attachment of the tool holder.

Based on the known geometrical and mass information of the spindle rotor, a simplified finite element rotor model was developed. The finite element rotordynamic code in this work did not consider the complex interactions of shrink fit interfaces, multiple material layers, inhomogeneous materials, small geometrical details, and so on. The spindle rotor modeling code assumed a single, homogenous linear elastic material for each element, with the ability of defining a single hollow volume along the rotational axis. Further, concentrated mass and bearing supports were added at desired station locations. The rotor model is defined by the element length, l, element outer diameter, OD, element inner diameter, ID, element modulus of elasticity, E, element density, ρ, concentrated mass, m, polar moment of inertia of concentrated mass, I_p, and transverse moment of inertia of concentrated mass, I_t.

The code is based on the transfer matrix method. The chief advantage of using this calculation method over other finite element methods is that the size of matrices generated used in calculations are independent of the number of finite elements in the rotor model. Because of this, computational cost does not increase with the number of elements in the model and is more suitable in situations where repetitive calculations are necessary, such as in model updating schemes. The main limitation of this method is that it can only be applied to particular situations where the model is constructed of elements that are arranged in-line or in series, one after the other. Naturally, beams are ideal candidates to take advantage of this computation method. The transfer matrix method is found in many references and is commonly separated into Holzer's method and Myklestadt's method for torsional systems and for beam flexing systems, respectively [51] [52] [53]. The transfer matrix method utilizes state vectors and transfer matrices to perform calculation from element to element. A typical element (or segment) is composed of two spans, one from a massless spring, k_{ns}, and the other from a point mass, m_{ns}. The state vector, $\mathbf{Z}_{ns}^{R}$, is a column of numbers which defines state variables at each station of the system, commonly displacements and forces based on the degrees of freedom at each segment. The state variables are transferred to from one station to the next by the transfer matrix, $\mathbf{H}_{ns}^{R}$. The left and right sides of the spans are referred to by *L* and *R* and the station number is referred to by *ns*. Since a typical segment is composed of two parts, the transfer matrix generally consists of the field transfer matrix and the point transfer matrix. The field transfer matrix relates the $\mathbf{Z}_{ns-1}^{R}$ state vector to the $\mathbf{Z}_{ns}^{L}$ state vector which covers the span containing k_{ns}. The point transfer matrix relates the $\mathbf{Z}_{ns}^{L}$ state vector to the $\mathbf{Z}_{ns}^{R}$ state vector which covers the span containing m_{ns}. The resulting transfer matrix covering both spans in the segment shown in Equation (5).

$$\mathbf{Z}_{ns}^{R} = \mathbf{H}_{ns}\mathbf{Z}_{ns-1}^{R} \tag{5}$$

Further, the state vector at the boundary, $\mathbf{Z}_0^R$, can be related to the state vector at station *ns*, $\mathbf{Z}_{ns}^R$, by observing Equation (6).

$$\mathbf{Z}_{ns}^R = [\mathbf{H}_{ns}\mathbf{H}_{ns-1}\cdots\mathbf{H}_2\mathbf{H}_1]\mathbf{Z}_0^R \tag{6}$$

The finite element rotor model is discretized into 73 elements (74 nodes) and is illustrated in Figure 26. It is directly compared to the design cross-section drawing to illustrate the location of the interference fit components outlined in boxes. Notice that the tool holder bolt (station 8) and sensor rings (stations 23 and 66) are modeled as rotating masses. They are assumed to have mass, I_p, and I_t values but not contribute any stiffness to the overall spindle rotor. Although the AMBs (nodes 28 and 62) are shown in Figure 26, they are not included in the rotor model until the open-loop plant model is derived.

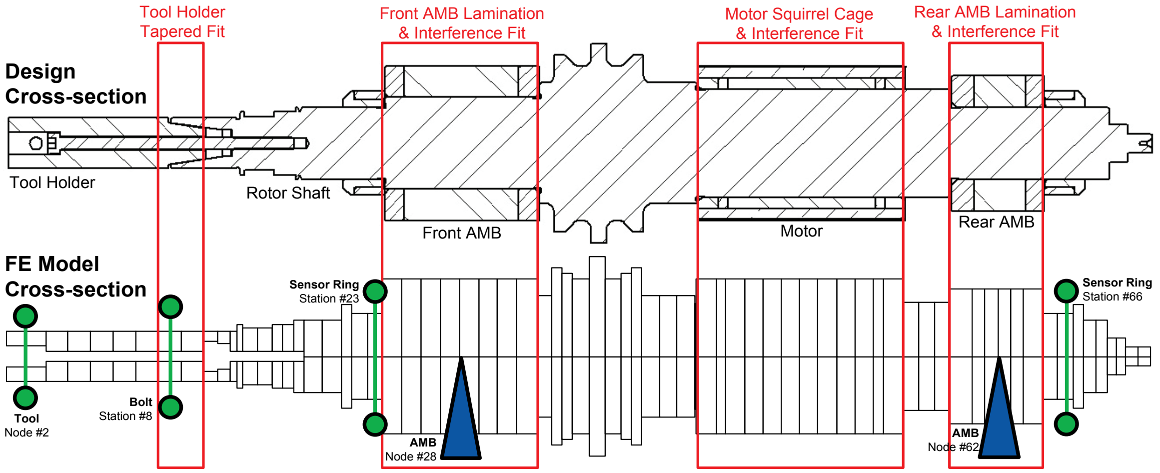

Figure 26: Finite element model compared with design drawing.

The model was oriented toward implementation in control systems, so a modally reduced state-space representation was most convenient. Modal truncation was applied in order to retain the first three flexible modes because the system identification measurements were not capable of capturing higher frequencies. Five modes m_t were retained which included two rigid-body modes m_r and the first three flexible modes m_f. In state-space systems, ordinary differential equations are represented in matrix form for programming convenience. They are also considered to be more numerically stable than models represented by transfer function equations. The state-space matrices for the free-free (*ff*) rotor, $\mathbf{A}_{ff}$, $\mathbf{B}_{ff}$, $\mathbf{C}_{ff}$, and $\mathbf{G}_{ff}$, are generated and are utilized for subsequent mathematical model manipulations [26]. Here, **s** is the state vector of node position, **f** is the input force on the selected nodes, and **y** is the output position of selected nodes in real coordinates. The term **Ω** is the rotor angular speed. The two perpendicular, longitudinal planes are represented by subscripts *v* and *w*. Nominally, 0.5 % proportional damping is added to the state-space model's flexible modes and gyroscopic coupling of the rotor's two mutually perpendicular planes is applied. A modally reduced state-space model of a single free-free rotor takes the form of the first-order differential in Equation (7). For notational convenience, the form of Equation (8) is used.

$$\begin{cases} \begin{Bmatrix} \dot{\mathbf{s}}_{ff,v} \\ \dot{\mathbf{s}}_{ff,w} \end{Bmatrix} = \begin{bmatrix} \mathbf{A}_{ff} & -\Omega\mathbf{G}_{ff} \\ \Omega\mathbf{G}_{ff} & \mathbf{A}_{ff} \end{bmatrix} \cdot \begin{Bmatrix} \mathbf{s}_{ff,v} \\ \mathbf{s}_{ff,w} \end{Bmatrix} + \begin{bmatrix} \mathbf{B}_{ff} & 0 \\ 0 & \mathbf{B}_{ff} \end{bmatrix} \cdot \begin{Bmatrix} \mathbf{f}_{ff,v} \\ \mathbf{f}_{ff,w} \end{Bmatrix} \\ \begin{Bmatrix} \mathbf{y}_{ff,v} \\ \mathbf{y}_{ff,w} \end{Bmatrix} = \begin{bmatrix} \mathbf{C}_{ff} & 0 \\ 0 & \mathbf{C}_{ff} \end{bmatrix} \cdot \begin{Bmatrix} \mathbf{s}_{ff,v} \\ \mathbf{s}_{ff,w} \end{Bmatrix} \end{cases} \tag{7}$$

$$\begin{cases} \dot{\mathbf{s}}_{ff} = \mathbf{A}_{ff}(\Omega)\mathbf{s}_{ff} + \mathbf{B}_{ff}\mathbf{f}_{ff} \\ \mathbf{y}_{ff} = \mathbf{C}_{ff}\mathbf{s}_{ff} \end{cases} \tag{8}$$

Generally, the inputs to the rotor model are forces and moments applied at each mass station and the outputs from the rotor model are displacements and rotations at each mass station. In the spindle system in this work, the inputs for this model are forces applied at the tool and AMB actuator locations. The outputs are the displacements at the tool and sensor locations. The sensor displacement outputs are directed to the controller while the tool location displacements are used for assessing spindle performance. Although all inputs and outputs can be retained, only a select few were preserved as shown in Equation (9), leaving only the relevant tool forces and AMB actuator forces. As a result, selection matrices, $\mathbf{S}_{tool}$ and $\mathbf{S}_{act}$, were created which reduced the dimension of the input vector from 292 forces and moments to just simply six input forces as shown in Equation (10). The subscripts $_{act}$, $_{amp}$, $_{tool}$, and $_{sens}$ refer to the actuator (AMBs) nodes on the rotor, the amplifier, the tool nodes on the rotor, and the AMB sensor nodes of the rotor, respectively.

$$\mathbf{f}_{ff} = \begin{Bmatrix} \mathbf{f}_{ff,v} \\ \mathbf{f}_{ff,w} \end{Bmatrix} : \ \mathbf{f}_{ff,v} = \begin{Bmatrix} f_{tool,v} \\ \vdots \\ f_{act_1,v} \\ \vdots \\ f_{act_2,v} \\ \vdots \end{Bmatrix} \ and \ \mathbf{f}_{ff,w} = \begin{Bmatrix} f_{tool,w} \\ \vdots \\ f_{act_1,w} \\ \vdots \\ f_{act_2,w} \\ \vdots \end{Bmatrix} \tag{9}$$

$$\mathbf{f}_{ff} = \mathbf{S}_{tool} \begin{Bmatrix} f_{tool,v} \\ f_{tool,w} \end{Bmatrix} + \mathbf{S}_{act} \begin{Bmatrix} f_{act_1,v} \\ f_{act_2,v} \\ f_{act_1,w} \\ f_{act_2,w} \end{Bmatrix} = \mathbf{S}_{tool}\mathbf{w}_{tool} + \mathbf{S}_{act}\mathbf{u}_{act} \tag{10}$$

Here, $\mathbf{w}_{tool}$ is the external force on the rotor applied to the tool nodes and $\mathbf{u}_{act}$ is the control current to the actuators. The outputs of interest were retained which included the displacements at the tool, AMB actuators, and sensors. As a result, selection matrices, $\mathbf{S}_{\text{tool}}$, $\mathbf{S}_{\text{sens}}$, and $\mathbf{S}_{\text{act}}$ were created which reduced the dimension of the output vector from the maximum 292 displacements and rotations to just ten displacements as shown in Equations (11) and more simply in Equation (12).

$$\mathbf{y}_{ff} = \begin{Bmatrix} \mathbf{y}_{ff,v} \\ \mathbf{y}_{ff,w} \end{Bmatrix} : \mathbf{y}_{ff,v} = \begin{Bmatrix} y_{tool,v} \\ \vdots \\ y_{sens_1,v} \\ \vdots \\ y_{act_1,v} \\ \vdots \\ y_{act_2,v} \\ \vdots \\ y_{sens_2,v} \\ \vdots \end{Bmatrix} \; and \; \mathbf{y}_{ff,w} = \begin{Bmatrix} y_{tool,w} \\ \vdots \\ y_{sens_1,w} \\ \vdots \\ y_{act_1,w} \\ \vdots \\ y_{act_2,w} \\ \vdots \\ y_{sens_2,w} \\ \vdots \end{Bmatrix} \tag{11}$$

$$\begin{gathered} \mathbf{y}_{tool} = \begin{Bmatrix} y_{tool,v} \\ y_{tool,w} \end{Bmatrix} = \mathbf{S}_{tool}^{\mathrm{T}} \mathbf{y}_{tool} \\ \mathbf{y}_{sens} = \begin{Bmatrix} y_{sens_1,v} \\ y_{sens_2,v} \\ y_{sens_1,w} \\ y_{sens_2,w} \end{Bmatrix} = \mathbf{S}_{sens}^{\mathrm{T}} \mathbf{y}_{ff} \\ \mathbf{y}_{act} = \begin{Bmatrix} y_{act_1,v} \\ y_{act_2,v} \\ y_{act_1,w} \\ y_{act_2,w} \end{Bmatrix} = \mathbf{S}_{act}^{\mathrm{T}} \mathbf{y}_{ff} \end{gathered} \tag{12}$$

By extracting the inputs and outputs in the manner described above, the rotor model is described by Equation (14). The terms defined below are used for notational convenience.

$$\begin{aligned}
\mathbf{B}_{tool} &= \mathbf{B}_{ff}\mathbf{S}_{tool} \\
\mathbf{B}_{act} &= \mathbf{B}_{ff}\mathbf{S}_{act} \\
\mathbf{C}_{tool} &= \mathbf{S}_{tool}^{\mathrm{T}}\mathbf{C}_{ff} \\
\mathbf{C}_{sens} &= \mathbf{S}_{sens}^{\mathrm{T}}\mathbf{C}_{ff} \\
\mathbf{C}_{act} &= \mathbf{S}_{act}^{\mathrm{T}}\mathbf{C}_{ff}
\end{aligned} \tag{13}$$

$$\begin{cases}
\dot{\mathbf{s}}_{ff} = \mathbf{A}_{ff}(\Omega)\mathbf{s}_{ff} + \mathbf{B}_{tool}\mathbf{w}_{tool} + \mathbf{B}_{act}\mathbf{u}_{act} \\
\mathbf{y}_{tool} = \mathbf{C}_{tool}\mathbf{s}_{ff} \\
\mathbf{y}_{sens} = \mathbf{C}_{sens}\mathbf{s}_{ff} \\
\mathbf{y}_{act} = \mathbf{C}_{act}\mathbf{s}_{ff}
\end{cases} \tag{14}$$

The calculations do not account for material layers, so an average total density per element was estimated based on the full knowledge of the complete spindle rotor's mass and geometry. The mass and volume of the remaining AMB and motor rotors were interpolated through subtraction of the known rotor shaft. Average mass and density properties were calculated for the AMB and motor regions outlined with boxes in Figure 26. All individual finite elements have a single specified set of material properties. The resulting rotor model retains correct geometry, mass, and polar and transverse moments of inertias. The boxed areas in Figure 26 designate the tapered fit, AMBs, and motor regions, where the modulus of elasticity, *E*, for each element was assumed to take nominal values of titanium and steel. These were nominal candidate values that were adjusted in subsequent model updating procedures. The remaining regions of the shaft had fixed nominal *E* values.

Table 1 lists the nominal material properties applied to the spindle rotor model, separated into groups corresponding to regions on the rotor. The exposed rotor shaft, where no additional components are mounted, retained nominal density and modulus of elasticity values. The tool holder retained the nominal density of Ti-6AL-4V; however, due to a tapered fit mounting feature, the nominal *E* value in that region of two elements was modified in model updating operations. The FE element groups marked with asterisks (*) in the table represent elements which have densities that have been averaged to account for multiple material layers as previously discussed. The (*) groups have lower density values which were due to the AMB and motor rotors being composed of materials that were of equal and lesser densities than the steel shaft. Similarly to the tool holder tapered fit, these sections were assigned nominal *E* values which were modified in model updating operations.

Table 1: Nominal spindle rotor material values of selected FE elements groups.

FE Element Group	**Density kg/m^3**	**Modulus of Elasticity GPa**
Tool Holder (Ti-6AL-4V)	4430.00	113.80
Rotor Shaft (Steel)	7850.00	205.00
Front AMB Region *	7802.97 *	205.00
Motor Region *	7811.27 *	205.00
Rear AMB Region *	7797.43 *	205.00

* Represents elements with densities that have been averaged.

3.1.2 **AMB Model**

The general force function, *F*, of the electromagnetic force is defined by Equation (15) and is a nonlinear function of coil current, *i*, and target-to-electromagnet gap, *g* [54]. The other terms are the geometric correction factor, ε, magnetic flux permeability constant in vacuum, $\mu_0 = 4\pi\times10^{-7}$ H/m, number of coils, *N*, and area face of each pole, A_g.

$$F = \varepsilon \frac{\mu_0 N^2 i^2 A_g}{4g^2} \tag{15}$$

Active magnetic bearings are inherently unstable without active control due to their negative stiffness properties. In addition to active control, AMBs are most often arranged in opposing pairs to increase their effectiveness in single axis of controlled actuation due to their inherent pull-only operation. The force function for an opposed magnetic actuator pair [54] is calculated with Equation (16).

$$F_{amb} = \left(\frac{\varepsilon \mu_0 A_g N^2 i_b}{x_c^2} \right) i_c - \left(\frac{\varepsilon \mu_0 A_g N^2 i_b}{x_c^3} \right) x_r \tag{16}$$

Here, the electromagnetic force equation, F_{amb}, has the terms control current, i_c, radial displacement, x_r, bias current, i_b, and nominal radial clearance, x_c. To simplify the calculation, the widely accepted linearized AMB model shown in Equation (17) was applied. It uses values for current stiffness, k_i, and position stiffness, k_x, which are assumed to be accurate for small displacements around the AMB's operating point. For augmentation into the open-loop model, the matrices $\mathbf{K}_x$ and $\mathbf{K}_i$ are defined in Equation (18).

$$\begin{Bmatrix} f_v \\ f_w \end{Bmatrix} = \mathbf{K}_i \begin{Bmatrix} i_{c,v} \\ i_{c,w} \end{Bmatrix} + \mathbf{K}_x \begin{Bmatrix} x_{r,v} \\ x_{r,w} \end{Bmatrix} \tag{17}$$

$$where,\ \mathbf{K}_x = k_x \begin{bmatrix} 1 & 0 \\ 0 & 1 \end{bmatrix} \ and\ \mathbf{K}_i = k_i \begin{bmatrix} 1 & 0 \\ 0 & 1 \end{bmatrix} \tag{18}$$

The spindle houses two radial AMBs which have associated parameters unique to each. They are arranged so that the eight coils act as four actuators per AMB oriented at 45° relative to the horizontal. The parameters used in AMB modeling are provided in

Table 2. The front AMB was applied to the model at node 28 and the rear AMB was applied at node 62 in the single plane. The thrust AMB was assumed to have no cross coupled effects in the spindle system and was not included in the model. Only lateral displacements were considered.

Table 2: AMB current and position stiffness values.

AMB Location	Current Stiffness, k_i N/A	Position Stiffness, k_x N/m
Front AMB	231.3	2,261,346.7
Rear AMB	97.1	934,911.1

When incorporated into Equation (14), the spindle model including the AMBs results in Equation (19).

$$\begin{cases} \dot{\mathbf{s}}_{ff} = \left[\mathbf{A}_{ff}(\Omega) - \mathbf{B}_{act}\mathbf{K}_x\mathbf{C}_{act}\right]\mathbf{s}_{ff} + \mathbf{B}_{tool}\mathbf{w}_{tool} + \mathbf{B}_{act}\mathbf{K}_i\mathbf{u}_i \\ \mathbf{y}_{tool} = \mathbf{C}_{tool}\mathbf{s}_{ff} \\ \mathbf{y}_{sens} = \mathbf{C}_{sens}\mathbf{s}_{ff} \end{cases} \tag{19}$$

$$where, \quad \mathbf{u}_i = \begin{Bmatrix} i_{c,v_1} \\ i_{c,v_2} \\ i_{c,w_1} \\ i_{c,w_2} \end{Bmatrix} = \mathbf{C}_{amp}\mathbf{s}_{amp} \tag{20}$$

3.1.3 **Power Amplifiers**

Each of the AMB axes relies on its own dedicated power amplifier which converts control voltage to control current. The control current generates particular magnetic flux in the electromagnets that attempt to restore the rotor to the requested position. The power amplifiers operate by tracking reference voltages from the controller using measured voltages that are directly proportional to coil currents. The relationship defining the dynamic behavior of the measured voltage and the coil current is referred to as transconductance. The power amplifier model transfer function plotted in Figure 27 has four inputs and four outputs which correspond accordingly to the rotor model's I/Os and is normalized to a DC gain of one. The amplifier model is in state-space form for direct incorporation into the open-loop plant model. Since all four amplifiers are alike, one transfer function is representative of each of their individual performance characteristics. The bandwidth is defined as when the magnitude of the transfer function decreases three dB below its DC value, which in this case is approximately 3500 Hz.

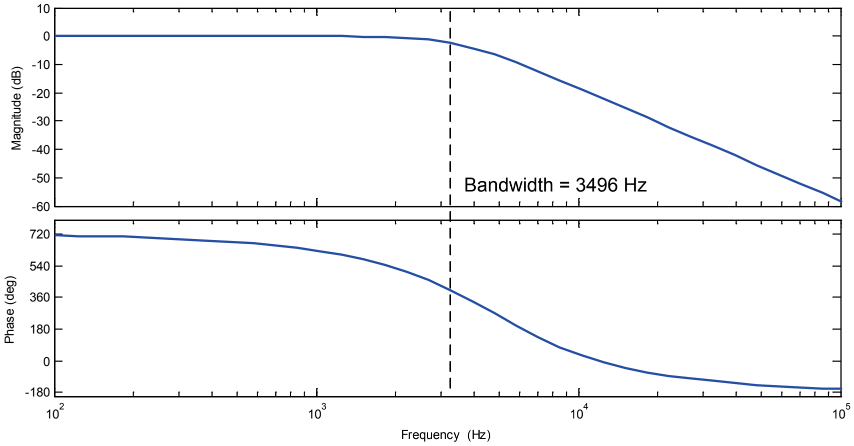

Figure 27: Amplifier transfer function and bandwidth.

The set of amplifiers is represented in Equation (21). Here, the control voltage signal, v, defines the $\mathbf{u}_{amp}$ vector.

$$\dot{\mathbf{s}}_{amp} = \mathbf{A}_{amp}\mathbf{s}_{amp} + \mathbf{B}_{amp}\begin{Bmatrix} v_{v,1} \\ v_{v,2} \\ v_{w,1} \\ v_{w,2} \end{Bmatrix} = \mathbf{A}_{amp}\mathbf{s}_{amp} + \mathbf{B}_{amp}\mathbf{u}_{amp} \tag{21}$$

3.1.4 **Nominal Open-Loop Model**

The open-loop model describes significant components in the control loop except for the controller. This consists of the free-free rotor model, the amplifier model, and the AMB actuator current and position stiffnesses. Figure 28 graphically illustrates the assembled state-space representation of these components. The controller is represented by the dashed lines and is not included. Further, Equation (22) shows the complete expression representing the open-loop model of the spindle system.

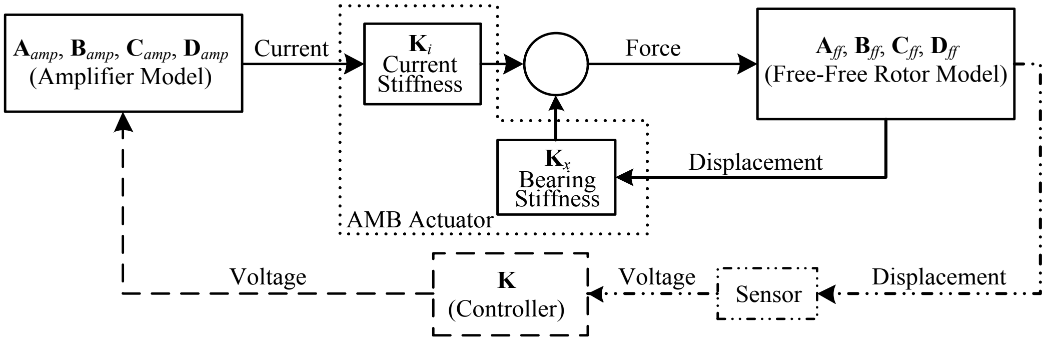

Figure 28: The open-loop model (solid lines).

$$\begin{cases} \begin{Bmatrix} \dot{\mathbf{s}}_{ff} \\ \dot{\mathbf{s}}_{amp} \end{Bmatrix} = \begin{bmatrix} \mathbf{A}_{ff}(\Omega) - \mathbf{B}_{act}\mathbf{K}_x\mathbf{C}_{act} & \mathbf{B}_{act}\mathbf{K}_i\mathbf{C}_{amp} \\ 0 & \mathbf{A}_{amp} \end{bmatrix} \begin{Bmatrix} \mathbf{s}_{ff} \\ \mathbf{s}_{amp} \end{Bmatrix} + \begin{bmatrix} \mathbf{B}_{tool} \\ 0 \end{bmatrix} \mathbf{w}_{tool} + \begin{bmatrix} 0 \\ \mathbf{B}_{amp} \end{bmatrix} \mathbf{u}_{amp} \\ \mathbf{y}_{tool} = \begin{bmatrix} \mathbf{C}_{tool} & 0 \end{bmatrix} \begin{Bmatrix} \mathbf{s}_{ff} \\ \mathbf{s}_{amp} \end{Bmatrix} \\ \mathbf{y}_{sens} = \begin{bmatrix} \mathbf{C}_{sens} & 0 \end{bmatrix} \begin{Bmatrix} \mathbf{s}_{ff} \\ \mathbf{s}_{amp} \end{Bmatrix} \end{cases} \tag{22}$$

The calculated transfer functions based on the nominal open-loop model do not represent the Bode$_{22}$ and Bode$_{44}$ experimental transfer functions. This is evident by examining Figure 29 which plots the open-loop model transfer function, $\mathbf{P}_0$, against experimental open-loop transfer function, $\mathbf{G}_0$. The error between the model and experimental data was quantified based on the difference of the corresponding resonance and the antiresonance peaks. Because system identification was performed in the nonrotating state, the calculated model responses were calculated under the same condition.

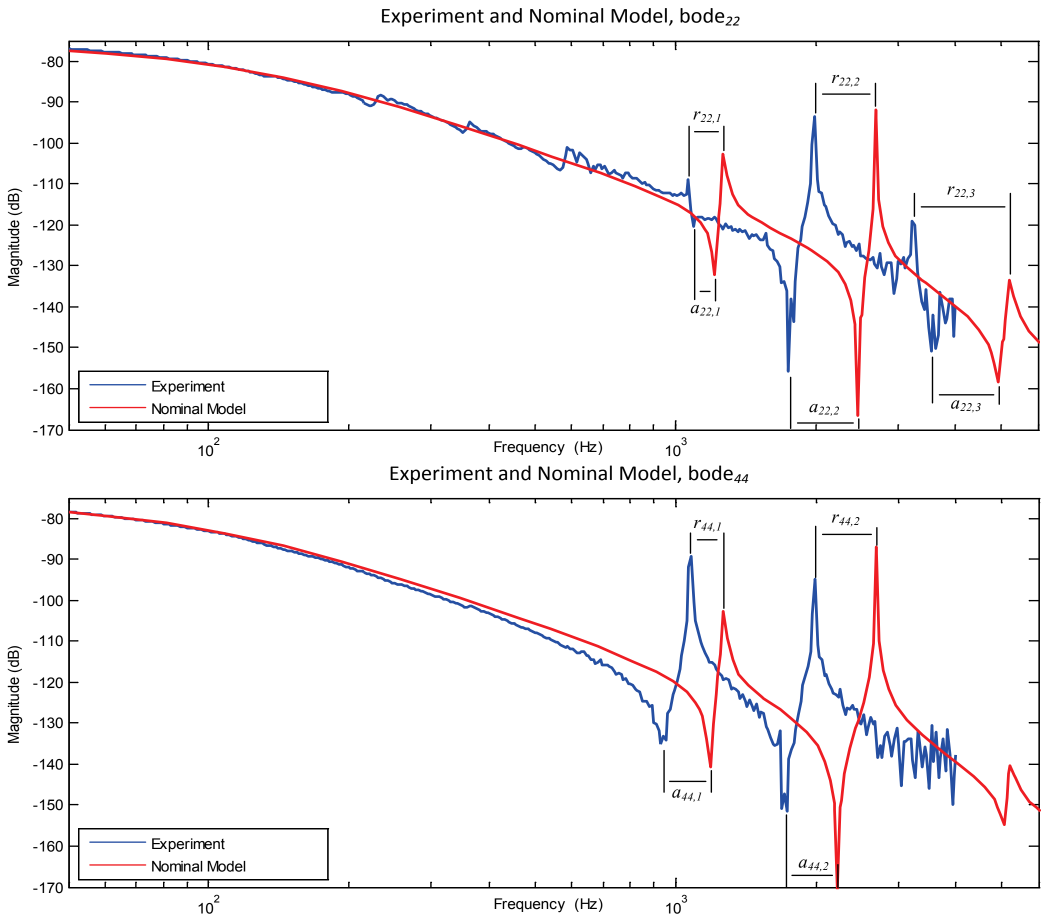

Figure 29: Nominal open-loop model compared to experimental transfer function data showing substantial disparity.

Table 3 and Table 4 are associated with both plots summarizing the differences between peaks. Void spaces in the table represent peaks that were not easily distinguishable from experimental data and were omitted. Note that the resonance values were omitted in the *W24* axis because they are identical to *W13* axis values. The terms $r_{ij,k}$ and $a_{ij,k}$ represent the resonance and antiresonance errors, respectively. The subscripts i and j denote the Bode plot from Figure 22 and the subscript k denotes the corresponding flexural resonance and antiresonance peak number. This annotation is used in model updating operations.

Table 3: Comparisons of experimental and calculated data corresponding to *W13* (Bode$_{22}$) axis.

Feature of Interest	Experiment, Hz	Model, Hz	Error, Hz / %
1st Resonance	1069	1270	$r_{22,1}$ = 201 / 18.0
2nd Resonance	1955	2692	$r_{22,2}$ = 737 / 37.7
3rd Resonance	3210	5219	$r_{22,3}$ = 2009 / 62.6
1st Antiresonance	1098	1219	$a_{22,1}$ = 121 / 11.0
2nd Antiresonance	1785	2472	$a_{22,2}$ = 687 / 34.5
3rd Antiresonance	3340	4937	$a_{22,3}$ = 1597 / 47.8

Table 4: Comparisons of experimental and calculated data corresponding to *W24* (Bode$_{44}$) axis.

Feature of Interest	Experimental, Hz	Model, Hz	Error, Hz / %
1st Antiresonance	940	1187	$a_{44,1}$ = 247 / 26.3
2nd Antiresonance	1700	2227	$a_{44,2}$ = 527 / 31.0
3rd Antiresonance	--	5080	$a_{44,3}$ = -- / --

Based on the resulting errors from comparisons of transfer functions, it was clear that the nominal open-loop plant model was not accurate. Correction of the model was required.

3.2 Model Updating

The goal of the model updating operations in this work was to adjust the modulus of elasticity values of structurally ambiguous spindle rotor regions in order to minimize the error when compared with the experimental transfer function data. By using the select elements' *E* values as the design variables, the rotor model retained true geometry, mass, and inertial properties. Adjusting only modulus of elasticity values compensated for simplification errors in the nominal model.

The open-loop model function is not readily differentiable so a derivative-free optimization routine was employed to minimize error between open-loop model and open-loop experimental data. This is an iterative approach where the error is minimized until the open-loop spindle model reaches an acceptably accurate solution. The error function was calculated from the difference of resonance and antiresonance frequencies between model and experiment, from the rotor's first three available modes.

3.2.1 Model Updating Background and Review

Since the advent of modern computers, computationally intensive matrix operations have been extensively applied in a vast array of fields. The application of finite element modeling dominates the modeling world due to its capability of modeling extremely complex models not possible with analytical approaches. However, it is up to the engineer to appropriately apply the current state-of-the-art modeling and simulation tools, which requires extensive practice and experience. Dynamic modeling is not a trivial task and almost always results in errors to some degree [55] when compared to experimentally acquired data. Discrepancies between finite element models and experimental data are generated for a variety of reasons [56] which primarily originate from structurally unknown features and engineering simplifications [57].

This brings into question the most practical approach of improving the model; model refinement or model updating [58]. Model refinement addresses the physical principle to produce a more advanced model which better represents the physics of the problem. Such approaches may account for nonlinearities, micro-scale effects, advanced boundary conditions, etc., which introduce complexity to the model, but in the end, still may not ensure higher accuracy results. The alternative approach is to correct the existing model based on physical observations/measurements through the application of model updating. With model updating, it may not be necessary to pursue exhaustive research campaigns for understanding all physics of a particular model, which may become costly and time consuming.

Two fundamental approaches exist in model updating that take the form of direct and iterative methods, quantified in both the time and frequency domains [59]. Direct methods act on the internal mass and stiffness matrices to produce the desired results very efficiently and quickly. Most of these methods are based on minimum norm corrections and methods based on control theory [60]. The limitation of this approach is that the updated mathematical representation may not translate back to a physically meaningful model which in many cases is not acceptable. In contrast, iterative approaches update particular physically meaningful model parameters in which the model's physical characteristics are maintained. Iterations are terminated when satisfactory level of model accuracy is reached. This approach commonly employs optimization routines which minimize an error function defined by the engineer.

Although an extensive list of methods exist [61], this work applies iterative, derivative-free optimization [62] model updating and is the focus of the forthcoming material. It is common knowledge that useful information is contained within the derivatives of any differentiable function. For continuously differentiable functions, the minimum is generally defined when the first-order derivatives equal zero. Many optimization routines take advantage of these differentiable function properties to effectively find an optimal solution. Although many functions fall in this category, the engineering field is continuously crossing paths with more and more non-differentiable functions in which derivative-free optimization methods are required [63]. This happens for a variety of reasons [64]. For example, experienced engineers commonly rely on legacy codes written many years ago to perform certain calculations in which the source code is proprietary. Re-writing some codes to be differentiable may be an extremely difficult and time consuming task. In other instances, non-differentiable functions take the form of complex, multidisciplinary problems consisting aerodynamic, thermodynamic, structural, etc., calculations in series. Although derivative-free optimization is commonly implemented, it does have limitations. The most significant consideration in this optimization is the quantity of design variables. On a serial machine, it may not be reasonable to have more than a few dozen of variables due to excessive computation time. Taking advantage of parallel computation when possible should be considered. Another known concern is in the case where there exist multiple minimizing solutions, derivative-free optimizations tend to minimize locally in the early iterations.

Construction of an objective function has been approached in a variety of ways, most of which rely on the experimental data to represent true system characteristics. Here, experimental data was assumed correct, although every experiment has some associated degree of error which many studies consider [65]. Most often, experimental frequency response functions are utilized as the basis of defining dynamic characteristics of the system.

Comparing and correlating model and experimental data should be performed on as many domains as possible, such as spatial, frequency, and time response [66] [67]. Several techniques have been adopted by to quantify the comparison and are categorized into either visual or numerical assessments [68]. There are an extensive list of methodologies from various authors, however, only a few are described.

The simplest method of assessment is the direct error calculation, $err(\tilde{\omega}_k)$, of resonance frequencies, $\hat{\omega}_k$ and $\tilde{\omega}_k$, between experiment and model, respectively. Based in this, Equation (23) shows an error function in which a perfect match of resonance values would result in an error of zero. The subscript k represents the resonance number (which inherently corresponds to the k^{th} mode shape number) and m_f is the number of flexible modes of interest. For visualization, $\hat{\omega}_k$ and $\tilde{\omega}_k$, may be plotted as points for all accessible resonances in an x-y plot.

$$err(k) = \sum_{k=1}^{m_f} \left| \hat{\omega}_k - \tilde{\omega}_k \right| \tag{23}$$

Experimental and calculated modes shapes may be directly compared by plotting one against the other. In cases where modes are complicated, visualization may be difficult. Similar to the natural frequency plot mentioned above, the normalized experimental and calculated mode shape vectors of can be plotted against each other in an *x-y* plot to assist in visualization of discrepancies. Points deviating from a line slope of one denote locations of error. A Mode Scale Factor (MSF) [67] is defined in Equation (24) where $\hat{\phi}_k$ and $\tilde{\phi}_k$ are the experimental and calculated mode shapes vectors, respectively, and the asterisk is the complex conjugate. It represents the slope of the best straight line for the model in with respect to the experiment.

$$MSF\left(\tilde{\phi}_k, \hat{\phi}_k\right) = \frac{\tilde{\phi}_k^{\ T} \hat{\phi}_k^{\ *}}{\tilde{\phi}_k^{\ T} \tilde{\phi}_k^{\ *}} \tag{24}$$

The Modal Assurance Criterion (MAC) [69] in Equation (25) is broadly used to quantify the comparison of mode shapes. The resulting value always lies between zero and one, with a value of one signifying a perfect match.

$$MAC(i, j) = \frac{\left|\hat{\phi}_i^T \tilde{\phi}_j\right|^2}{(\hat{\phi}_i^T \hat{\phi}_i)(\tilde{\phi}_j^T \tilde{\phi}_j)} \tag{25}$$

The MAC is extended to include a set of mode shapes for each individual degree of freedom and is referred to as the Coordinate Modal Assurance Criterion (COMAC) [70]. The COMAC is calculated in Equation (26) where $\tilde{\phi}_{ik}$ and $\hat{\phi}_{ik}$ is the i^{th} component of the k^{th} calculated and experimental mode shape vectors.

$$COMAC(i) = \frac{\left(\sum_{k=1}^{m_f} \left| \tilde{\phi}_{ik} \hat{\phi}_{ik}^{*} \right| \right)^2}{\sum_{k=1}^{m_f} \left(\tilde{\phi}_{ik} \right)^2 \sum_{k=1}^{m_f} \left(\hat{\phi}_{ik}^{*} \right)^2} \tag{26}$$

Even further, the application of model updating has been successfully implemented in the field of damage detection [71] [72] [47]. Although it is not pursued in this work, it remains an appealing field of study.

3.2.2 **Spindle Open-loop Plant Model Updating Methodology**

Section 3.1.4 presents transfer function comparisons illustrating the inaccuracy of the nominal open-loop plant model. Since each modeling problem is unique, methodologies to address and correct the nominal model errors are specifically tailored to each individual problem. This section outlines steps for the open-loop model updating methodology formulation presented in this work.

A *model updating* approach was utilized here. The initial realization of the problem was whether or not to attempt to refine the nominal model with enhancements in modeling the extensive physics if the structure. This refers to predicting the properties of structurally ambiguous regions of the rotor such as the AMB/motor rotors, effects of shrink fits, and the tapered fit connection of the tool holder. In many cases, this is not a practical approach due to the extensive research efforts required, in which success is not always guaranteed. Hence the model updating approach was embraced in this work. Here, model updating was utilized to compensate for the nominal model simplifications at the known structurally ambiguous rotor regions. It was essential to understand exactly what parameter of the particular regions is ambiguous, which in this case is strictly the modulus of elasticity of the selected finite elements. The rotor mass and geometry is known and was not altered.

An *iterative* model updating approach was used to update model to maintain a physically realistic representation of the real rotor. The iterative method used here operated on a physically meaningful parameter, in particular, the finite element's *E* value. Model adjustments were performed until an updating termination criterion was met.

An *error function* was constructed based on the differences between the transfer functions of the experimental measurements and model calculations. Experimental data was acquired from in-situ MIMO sinusoidal sweeps as described in Section 2.3. The transfer function data utilized is in the frequency domain which provided access to resonance and antiresonance peak information. The information contained within the transfer functions is exploited to define the system's resonance frequencies (resonance peaks) and mode shapes (antiresonance peaks).

A *derivative-free optimization* routine was required in this case due to the inaccessibility of derivative information of the open-loop plant function. This function is considered a *black box* because the optimization routine only considered the specified elements' *E* values as the design variables and minimized the single error value that was produced. Because the purpose of the design variables is to compensate for the unknown magnitude of modeling error, *unconstrained* optimization was applied. The degree of unrealism of the updated *E* values was not essential for this work since it was strongly dependent on the degree of error of the nominal model generated by the engineer. It should be emphasized that, the unrealistic numerical values of updated *E* values were not a concern since the importance lies in the accuracy of the rotor model's dynamic, geometrical, and mass properties.

The *Nelder-Mead non-linear unconstrained optimization method* [73] [74] [75] was used to perform the minimization of the nominal model error. This is a well-established, derivative-free optimization algorithm which can handle discontinuous, non-smooth functions. This method minimizes the function of real design variables using only the objective function's value. The search for function minimization proceeds through recursive updates of the simplex vertices. Each simplex operation depends on the objective function evaluation, where the simplex is updated through a progression of reflection, expansion, contraction, and shrinkage operations.

Model assessment was performed in closed-loop form to evaluate the updated model's robustness for predictive use. The complete closed-loop spindle model was presented which utilized the PID controller.

3.2.3 **Spindle Open-Loop Plant Model Updating Formulation**

The nominal open-loop plant in Section 3.1.4 is the basis of the model's transfer function calculation. The rotor model within the open-loop plant requires *E* value corrections in the structurally ambiguous regions as shown in Figure 30. Although there are 28 elements in the regions of interest, 15 design variables were formulated to balance computational cost and rotor solution flexibility. This was accomplished by pairing selected neighboring elements into one design variable.

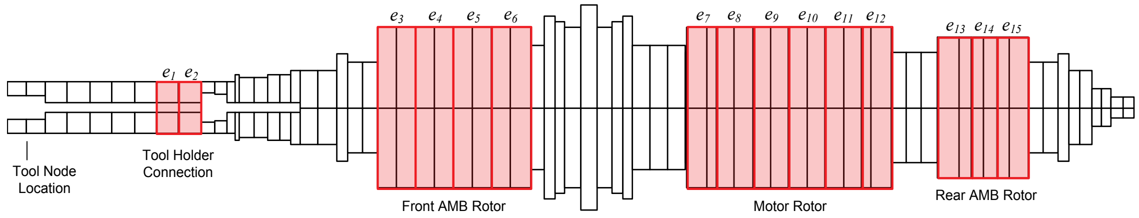

Figure 30: FE rotor model illustrating locations of the 15 modulus of elasticity design variables.

Initialization of the updating routine began with the definition of the design variables, e_p, represented by the vector, $\mathbf{e}$, in Equation (27), where subscript p denotes the individual design variable and n is the total number of design variables. All other finite elements have fixed nominal properties and were assumed correct.

$$\mathbf{e} \in \mathbb{R}^n \text{ so that } \left\{ e_p \right\}_{p=1\ldots n} \tag{27}$$

The function $B(\mathbf{e})$ is an augmentation of the open-loop rotor transfer function $\mathbf{P}_0(\mathbf{e})$ and the open-loop experimental transfer function $\mathbf{G}_0$ which outputs a real numerical error value calculated by $err(r_{ij,k}, a_{ij,k}) \in \mathbb{R}$. The variables $r_{ij,k}$ and $a_{ij,k}$ represent the resonance errors and antiresonance errors, respectively.

$$\begin{aligned} r_{ij,k} &= \left| \hat{\omega}_{ij,k} - \tilde{\omega}(\mathbf{e})_{ij,k} \right| \\ a_{ij,k} &= \left| {}^a\hat{\omega}_{ij,k} - {}^a\tilde{\omega}(\mathbf{e})_{ij,k} \right| \end{aligned} \tag{28}$$

The subscripts i and j reference the individual transfer function in Figure 22 and the subscript k denotes the corresponding flexural resonance or antiresonance peak number. The variables $\hat{\omega}_{ij,k}, \tilde{\omega}(\mathbf{e})_{ij,k} \in \mathbb{R}$ are the experimental and calculated values for resonances, respectively. The variables ${}^a\hat{\omega}_{ij,k}, {}^a\tilde{\omega}(\mathbf{e})_{ij,k} \in \mathbb{R}$ are the experimental and calculated values for antiresonances, respectively, denoted with the superscript a. The frequency values for $\hat{\omega}_{ij,k}$ and ${}^{a}\hat{\omega}_{ij,k}$ are extracted manually from $\mathbf{G}_{0,ij}$ and are hard coded into expressions $r_{ij,k}$ and $a_{ij,k}$ since they are fixed and do not change for this system. The frequency values $\tilde{\omega}(\mathbf{e})_{ij,k}$ and ${}^{a}\tilde{\omega}(\mathbf{e})_{ij,k}$ are extracted based on calculation of poles and zeros of $\mathbf{P}_{0}(\mathbf{e})_{ij}$. The error, in the most general form, between $\mathbf{G}_{0}$ and $\mathbf{P}_{0}(\mathbf{e})$ is calculated in Equation (29). The terms b_x and b_y represent the dimension of the experimental MIMO Bode plots in Figure 22. The exponents $w_{k,r}$ and $w_{k,a}$ are the weighting factors for each error value which can be different based on the mode error priority decided by the engineer.

$$err(r_{ij,k}, a_{ij,k}) = \sum_{i=1}^{b_x} \sum_{j=1}^{b_y} \sum_{k=1}^{m_f} \left[r_{ij,k}^{w_{k,r}} + a_{ij,k}^{w_{k,a}} \right] \tag{29}$$

The open-loop plant, experimental data, and error function are augmented into a *black box* function $B(\mathbf{e})$ as illustrated in Figure 31. Here, the input is **e** and the output is a single real value representing the error. The generalized minimization is defined to find the vector **e** such that:

$$\min_{\mathbf{e} \in \mathbb{R}^n} B(\mathbf{e}) \tag{30}$$

An important note is made about the redundancy of both the $r_{ij,k}$ and $a_{ij,k}$ terms in Equation (29). All of the MIMO transfer functions (experimental and calculated) have the same resonance values $\hat{\omega}_{ij,k}$ and $\tilde{\omega}(\mathbf{e})_{ij,k}$, so only one Bode plot is required to define the open-loop plant's resonances frequency values. However, the antiresonance values ${}^{a}\hat{\omega}_{ij,k}$ and ${}^{a}\tilde{\omega}(\mathbf{e})_{ij,k}$ are unique throughout the MIMO transfer function, where each Bode plot has a matching twin since the rotor is based on measurement on two perpendicular planes, *V* and *W*. To avoid redundancy, only two selected Bode plots out of sixteen were chosen and assumed adequate for define the open-loop model dynamics. The error function used in this works was based on Bode plots from the *W*-plane with inputs and outputs at the same corresponding AMB. Equation (31) defined the error function used in this work which is based on Bode$_{22}$ and Bode$_{44}$. Here, the weighting factors were chosen the have the same value for correcting all peaks in the transfer function comparison.

$$err(r_k, a_k) = \sum_{k=1}^{3} \left[r_{22,k}^2 + a_{22,k}^2 + a_{44,k}^2 \right] \tag{31}$$

To implement the Nelder-Mead minimization routine, the vector, **e**, populated with e_p values was required to begin the search. At this point, mitigation of two concerns regarding the Nelder-Mead algorithm was addressed. Firstly, the inherent serial operation of the algorithm was moderated by employing all processing cores on the machine to run independent minimizations in parallel, one per processing core. This resulted in multiple solutions per run initialization. Secondly, the inherent tendency for the Nelder-Mead algorithm to minimize to a single local solution was lessened by seeding the **e** vector with randomly generated e_p values, constrained to ±100 % of the nominal E values. Depending on how many processing cores were employed, an array of updated open-loop models was generated, where one was manually selected. The array of updated models generated trended to similar solutions, although none were exactly the same.

The model updating flow chart is illustrated in Figure 31. Here, the optimization was terminated when the result of the objective function evaluation would not reach any lower values. At this point it was assumed that the updated model was satisfactorily near a solution.

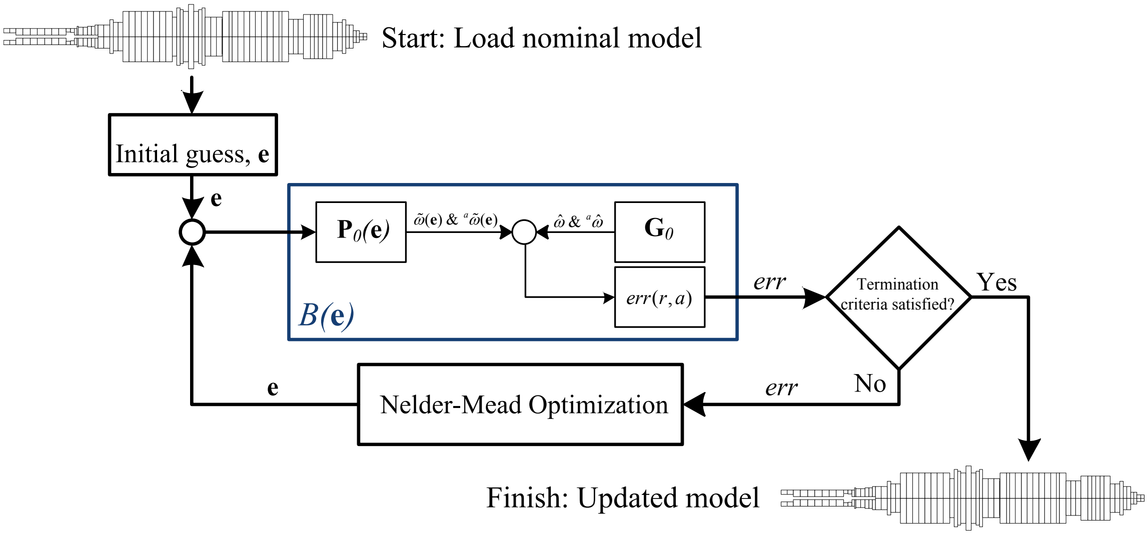

Figure 31: Flow chart of model updating operation, where $\mathbf{P}_0(\mathbf{e})$ is the open-loop plant as a function of the updating variables and $\mathbf{G}_0$ is the open-loop measurement.

3.2.4 **Model Updating Results**

The computer used for running the optimization routine is equipped with a 2.6 GHz quad-core processor with 4 Gb memory. When applying the Nelder-Mead simplex minimization algorithm with 15 design variables in combination with other open-loop model assembly calculations, the updating iterations ran at approximately 1.0 Hz. To reach a solution that successfully met the termination requirements, on average, 400-500 iterations were necessary. The updated model transfer function is compared with the experimental data in Figure 32 showing Bode$_{22}$ and Bode$_{44}$. The updated model agrees well with experimental data based on the correspondence of resonance and antiresonance peaks. The error values listed in Table 5 and Table 6 present errors that are mostly less than 1.0 %.

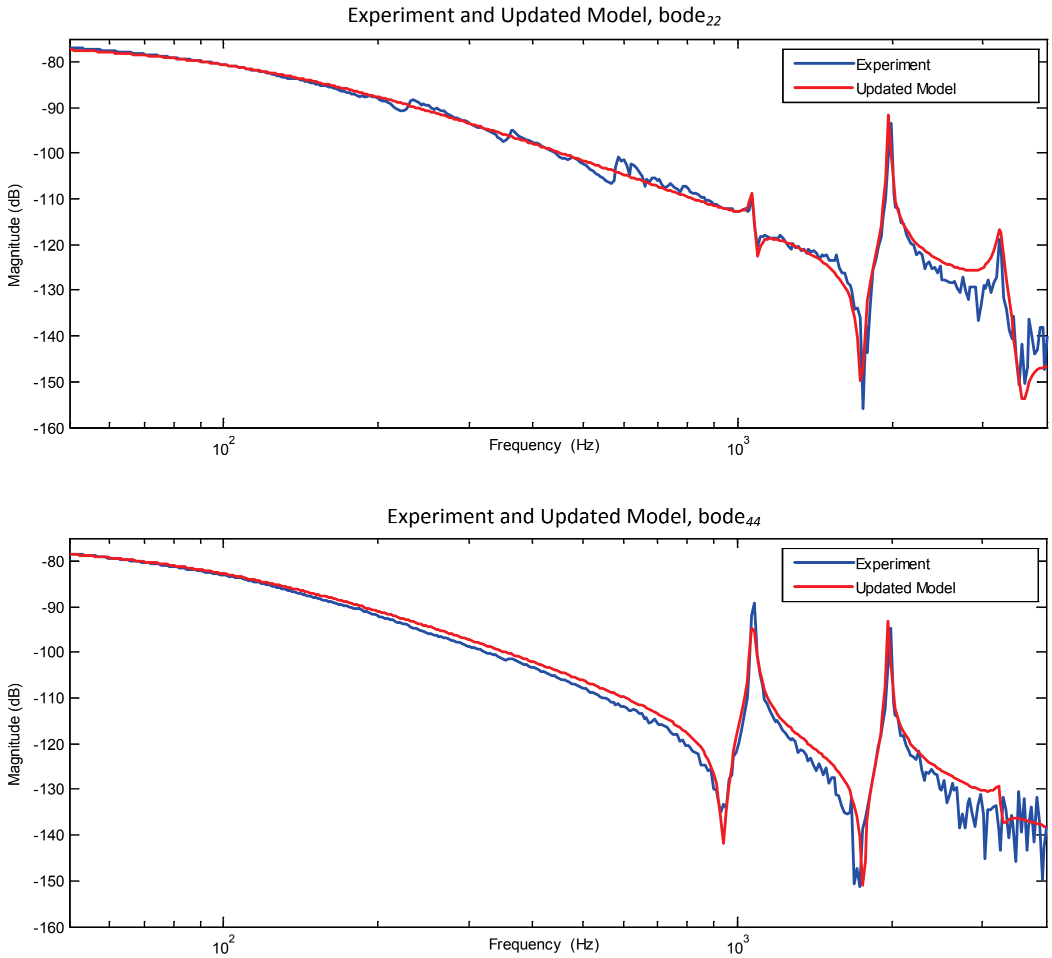
Experiment and Updated Model, bode$_{22}$

Experiment and Updated Model, bode$_{44}$

Figure 32: Comparison of experiment and updated open-loop model, Bode$_{22}$ (top) and Bode$_{44}$ (bottom).

Table 5: Tabulated comparisons corresponding to *W13* (Bode$_{22}$) axis experimental and updated calculated data.

Feature of Interest	Experiment, Hz	Updated Model, Hz	Error, Hz / %
1st Resonance	1069	1070.7	$r_{22,1}$ = 1.7 / 0.02
2nd Resonance	1955	1953.8	$r_{22,2}$ = 1.2 / 0.06
3rd Resonance	3210	3210.5	$r_{22,3}$ = 0.5 / 0.01
1st Antiresonance	1098	1099.8	$a_{22,1}$ = 1.8 / 0.16
2nd Antiresonance	1785	1778.5	$a_{22,2}$ = 6.5 / 0.36
3rd Antiresonance	3340	3358.8	$a_{22,3}$ = 18.8 / 0.56

Table 6: Tabulated comparisons corresponding to *W24* (Bode$_{44}$) axis experimental and updated calculated data.

Feature of Interest	Experimental, Hz	Updated Model, Hz	Error, Hz / %
1st Antiresonance	940	951.5	$a_{44,1}$ = 11.5 / 1.22
2nd Antiresonance	1700	1706.5	$a_{44,2}$ = 6.5 / 0.38
3rd Antiresonance	--	3320.1	$a_{44,3}$ = -- / --

Model/experiment resonance and antiresonance correspondence is graphed in Figure 33 where the left plot illustrates the quality of the nominal model and the right illustrates the quality of the updated model. The plots here have experimental values of the resonance ($\hat{\omega}_{ij,k}$) and antiresonance (${}^{a}\hat{\omega}_{ij,k}$) on the *x*-axis and the calculated values ($\tilde{\omega}_{ij,k}$ and ${}^{a}\tilde{\omega}_{ij,k}$) on the *y*-axis. The nominal model clearly exhibits errors, while the updated model marks are located nearly along the 0 % error line.

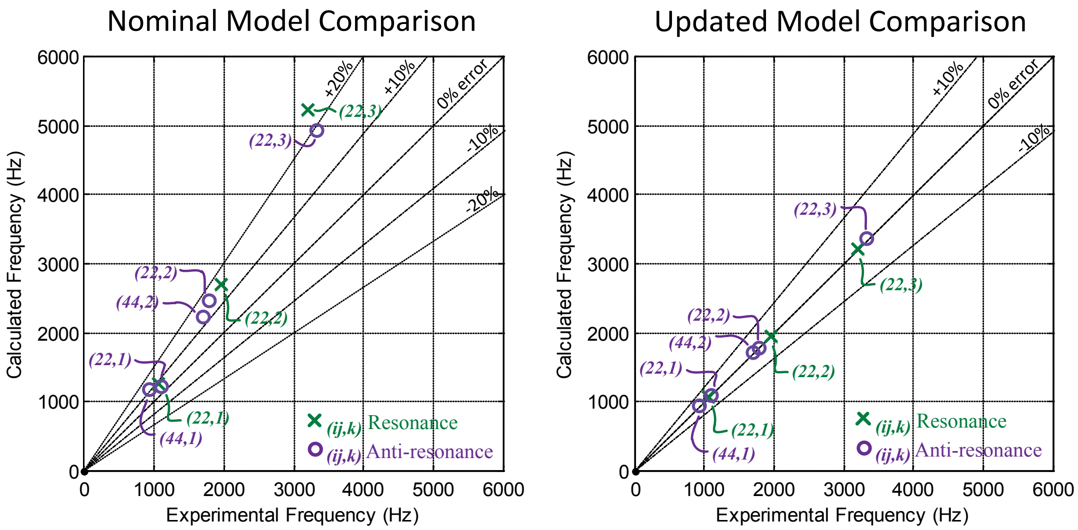

Figure 33: Nominal (left) and updated (right) models compared against experimental data.

The normalized free-free mode shapes of this rotor model are shown in Figure 34. The conical rigid-body mode and the first three flexible bending modes are plotted as well as sensor and bearing locations. Exciting the spindle in its designed speed range induces a rotor bending mode that approaches the first bending mode depicted in the plot. By closely examining the mode shape as well as the sensor and bearing locations, it is observed that the there is a bending node near the front sensor as suggested by examination of Bode$_{22}$. Mode shapes are often difficult model features to predict and verify. However, the presented free-free mode shapes hold merit due to the accuracy of the antiresonances seen in Figure 32.

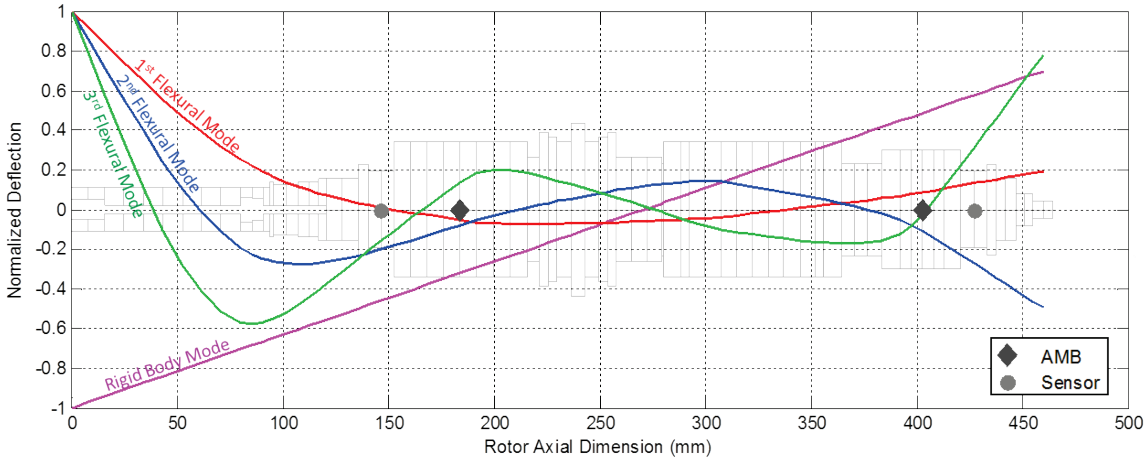

Figure 34: Modeled updated mode shape plot of rotor.

The updated Young's modulus values, e_p, are plotted in Figure 35, illustrating significant deviations from realistic material values. The updated **e** vector forces the open-loop plant model to exhibit dynamic characteristics (up to the third flexible mode) comparable to those measured experimentally. Note that the mass and geometry were not modified in the rotor's finite element model so the rotor maintained true physical characteristics.

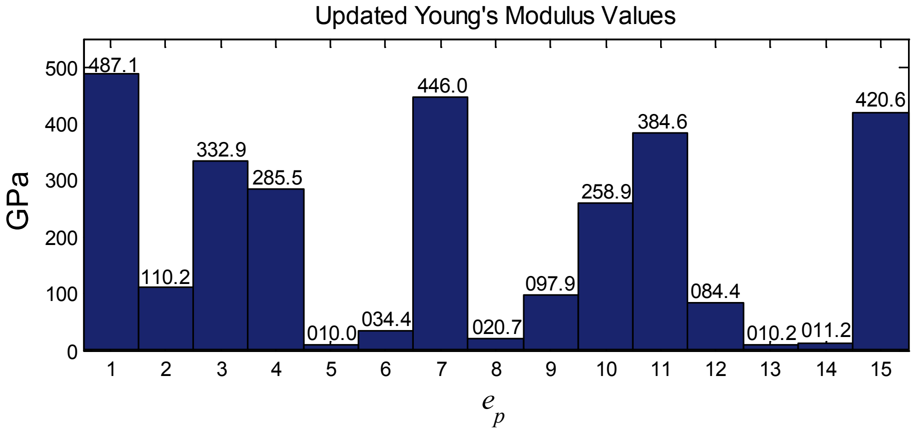

Figure 35: Bar graph illustrating the updated modulus of elasticity values.

The source of the unconventional *E* values is the simplification in the nominal finite element rotor model. The finite element model does not account for multiple material layers, material bonding physics, and inhomogeneous material properties, all which contribute to its inaccuracy. To generate a model with realistic *E* values, the finite element rotor model needs to be refined to include all the previously mentioned qualities. This would require a far more complex finite element code than the in-house code used in this work.

3.3 Updated Model Assessment

The updated modulus of elasticity values, e_p, did not represent realistic values for the materials in the rotor. This, understandably, introduces question in the validity of the updated model so experimental testing and comparisons were carried out to assess the reliability of the updated plant model, especially for predictive uses.

The following experimental/simulated model assessments were performed; mode shapes comparisons in the spatial domain and tool location response comparisons in the time domain. These assessments investigated the predictive quality of the closed-loop spindle model levitating with the PID control, in the non-rotating state. Note that the PID controller was not modified for the updated plant model; the same was used in the system identification MIMO transfer functions.

The assessments were based on experimentally accessible locations on the rotor shaft which were limited to the length of exposed rotor due to the spindle housing as seen in the photo in Figure 15. Also included were the measurements at the internal AMB sensors. The external sensor used for the measurements is a capacitance probe model C23-C from Lion Precision pictured in Figure 36 below.

Figure 36: Lion Precision capacitance probe model C23-C applied as an additional vibration sensor outside of the spindle housing.

The assessment operations were executed at or including the tool location which was independent of the locations (AMBs) where MIMO transfer functions were acquired for model updating purposes. The closed-loop spindle model's predicted responses using the updated rotor model, demonstrated agreement with experimental data.

3.3.1 **Mode Shape Assessment**

Mode shape assessment is generally a difficult task due to the inaccessibility to the rotor. The mode shapes measurements were performed in-situ on the accessible rotor length which is 107 mm from tool holder tip to where the spindle housing begins. AMB sensor data was recorded and included in the mode shape measurements as well.

The model simulations were calculated based on free-free mode shapes analysis of the rotor. The assumption made here states that the free-free bending modes of the rotor were negligibly influenced by the PID control and sensor/actuator hardware. The reasoning for this was that the rotor itself is very robust, i.e., its slenderness ratio is relatively low. The controller and AMB stiffness values primarily affect the rigid-body modes if the rotor. Through close examination of Figure 20, it is seen that the rotor's three bending modes do not change from closed-loop to open-loop form which suggests that the PID controller has negligible influence. However, care must be taken in this observation because may not hold true for rotors with high slenderness ratio in which control forces have significant effect on rotor flexure. For this case, it was assumed acceptable to compare the free-free model mode shapes with the closed-loop measured mode shapes.

The experimental acquisition of the mode shape was accomplished through the use of the Lion Precision capacitance probe mounted on to translation stage which allowed for displacement mapping the exposed rotor in the axial direction. To acquire bending mode data, the rotor was excited by the front AMB on the *W*-plane. A continuous sinusoidal signal was applied at the exact frequency of resonance corresponding to the desired bending mode. The sinusoidal injection force was adjusted to induce sufficient displacements at the rotor tip location which was approximately 100 μm, 60 μm, and 20 μm peak-to-peak for the first, second, and third bending modes, respectively. During this operation, the capacitance probe was translated along the exposed rotor beginning from the tool end in 3 mm increments, acquiring 5 s of data at each position at 50 kHz acquisition rate using a dSPACE ds1103 system. A sufficient spatial resolution was achieved with 36 axial measurement points along the accessible rotor length. Two additional measurement points were included from the AMB sensors to produce 38 total mode shape measurement points registered with blue circles in Figure 37. Note that the AMB actuator and sensor locations are shown as well.

Processing of the time domain data was required to correctly plot spatial mode shape data. First, band-pass filtering centered at the resonance frequency was applied to filter out noise. Noise was found to be problematic at locations near bending nodes because it registered as vibration amplitudes when there wasn't. Filtering out noise in this manner was acceptable because the only frequency of interest was the single resonance injection frequency. The position data was squared and then numerically integrated to yield a single value for each 5 s data set at each axial location. The vibration amplitude was solved for using the analytic solution of the integral of the square of a sine wave. This assumes the true lateral motion of the shaft was in the form of a sine wave since sinusoidal signal was injected. This method was found to be more consistent than other methods such as RMS evaluations. Vibration amplitude was found for each position along the shaft and the results were normalized by dividing by the maximum amplitude. Note that because the amplitude of vibration is always positive, the sign of the amplitude was manually changed when the value of zero (bending node) was approached.

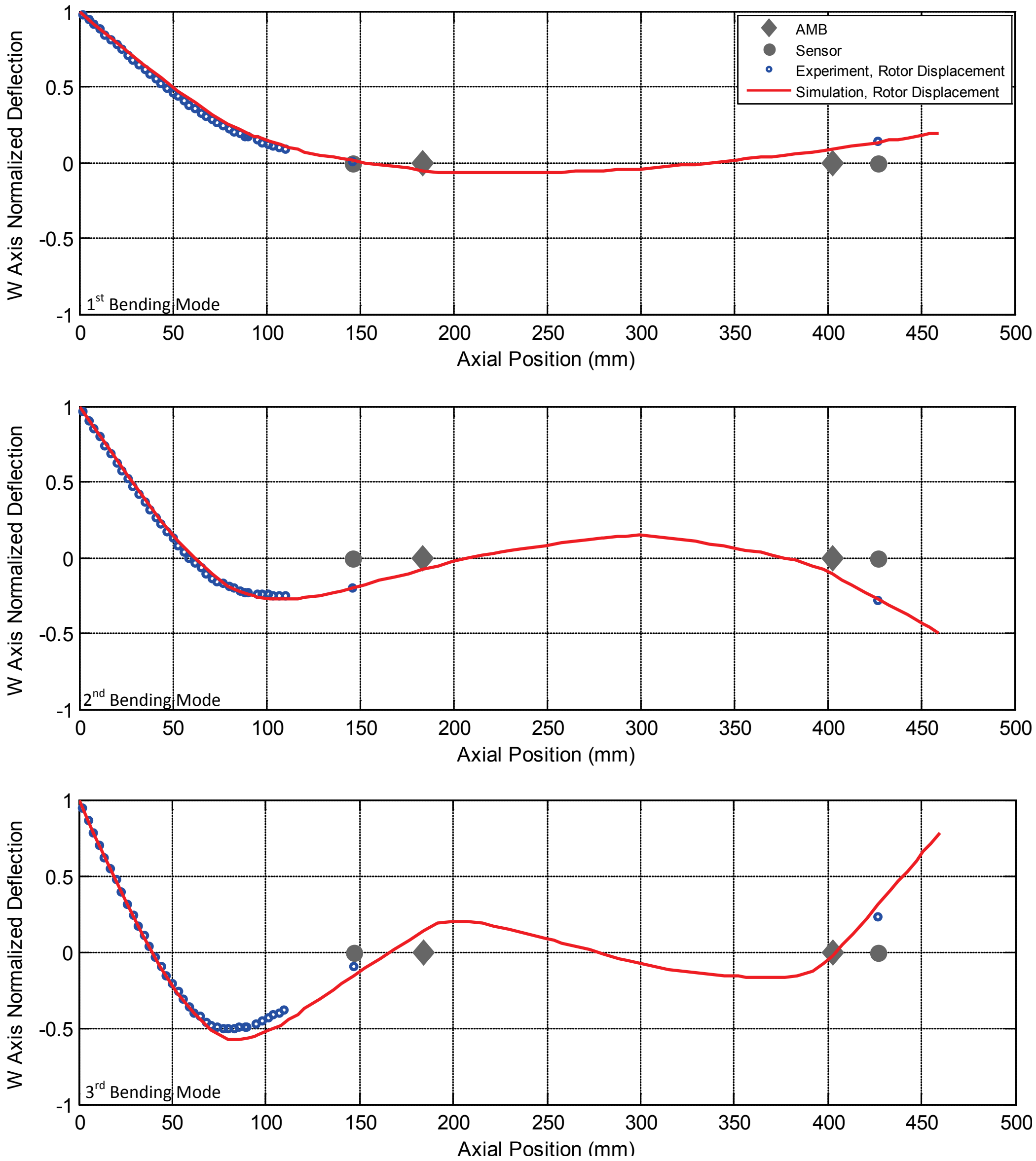

Figure 37: Simulated mode shapes plotted against experiment, normalized for the first three bending modes.

Figure 37 illustrates the comparison of experimental and modeled free-free mode shapes. Through observation of this comparison, it is evident that the results agree with each other very well. The first two bending modes show a nearly identical match while third begins to show some mismatch. This may be associated with the deficiency of the third antiresonance frequency information in the experimental transfer function data seen in Table 6.

3.3.2 Time Response Model Assessment

The aim of the time response comparisons was to assess the predictive performance of the updated model in closed-loop form. The closed-loop model utilizes the updated open-loop model in feedback configuration under PID control. The PID parameters used for closed-loop simulations were extracted from the real spindle's PID controller. The time response comparisons presented were performed at the tool location located near the rotor end. Again, note that the locations of the tool performance assessments are independent of system identification data which the updated model was corrected with. The significance of predicting spindle rotor response at the tool location is that it enforces the strength of updating the open-loop model based on resonance and antiresonance values from the transfer function measurements made at the AMBs. The intent is to establish higher confidence levels in the model's predictive ability under various loads and locations.

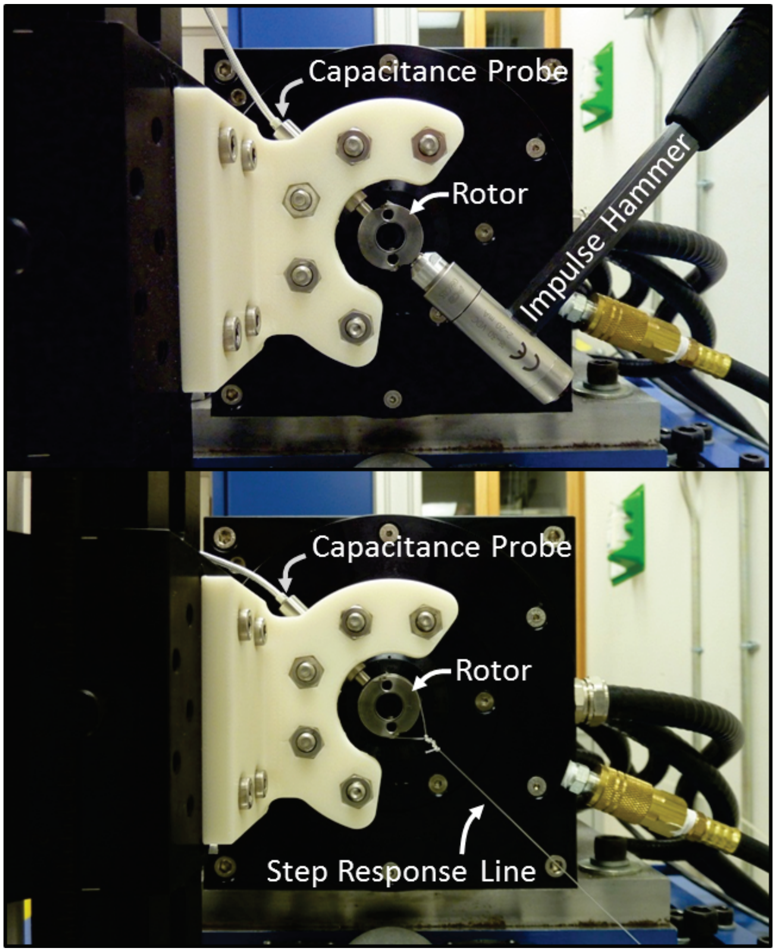

Figure 38: Front view of experimental setup of impulse (top) and step (bottom) response measurements at the tool location.

Two tool location time response comparisons are carried out in the levitated state to assess the closed-loop spindle model; an impulse and step response. Both time response tests are conducted in the *W*-plane plane, avoiding planar cross-coupling effects as much as possible. This is illustrated in Figure 38 showing the front view of the experiment, with excitation and measurement at the tool location. The impulse response experiment utilized an instrumented hammer (model#: PCB Piezotronics 086C03) to strike the rotor at the tool location opposite of the capacitance probe. The hammer and capacitance probe were connected to a dSPACE ds1103 system, recording the responses of both with 50 kHz sample rate. The step response experiment utilized a set of weights attached with a nylon string, applying a known force to the rotor at the tool location. The nylon string was routed with a pulley to avoid interference with the machining station frame. Once the rotor was loaded, the nylon string was cut to induce a step unloading. The time response at the tool location was measured with the same capacitance probe.

The impulse response simulation was based on an approximation of the experimental the impulse force data extracted from the instrumented hammer. Figure 39 illustrates the estimated impulse. The experimental impulse was defined by the area under the curve over a specified interval of time. Here, the area under the experimental force curve was estimated through trapezoidal numerical integration in the first time interval where the curve was positive. The estimated impulse has the same area under the curve as well as the same maximum values. The simulated impulse applied at the tool location resulted in an impulse force, F_{imp}, equal to 115 N for an impulse duration, t_{imp}, equal to 0.6 μs.

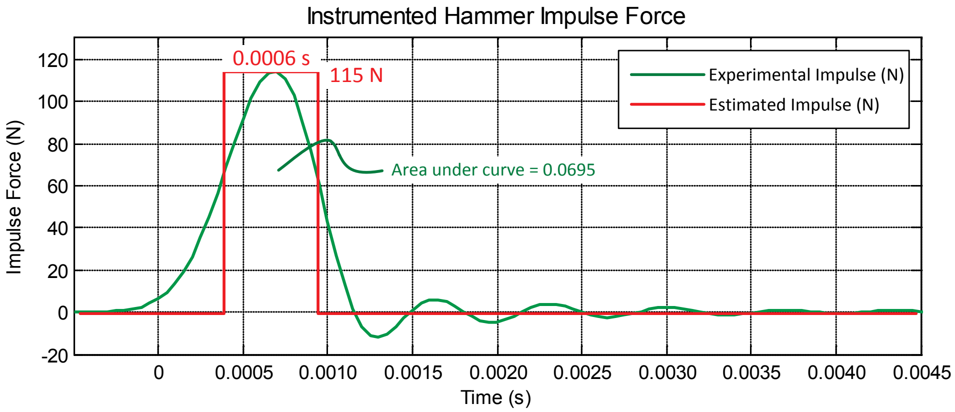

Figure 39: Estimated impulse force, determined from instrumented hammer data.

The step response simulation applied the force induced by the weights suspended by the nylon string at the tool location. The step response force, F_{stp}, is equal to 36.77 N which was delivered by 3.75 kg hanging weights. The simulation was initialized with F_{stp} forcing the rotor at the tool location and was stepped instantly to a value of zero, resulting in a step unloading.

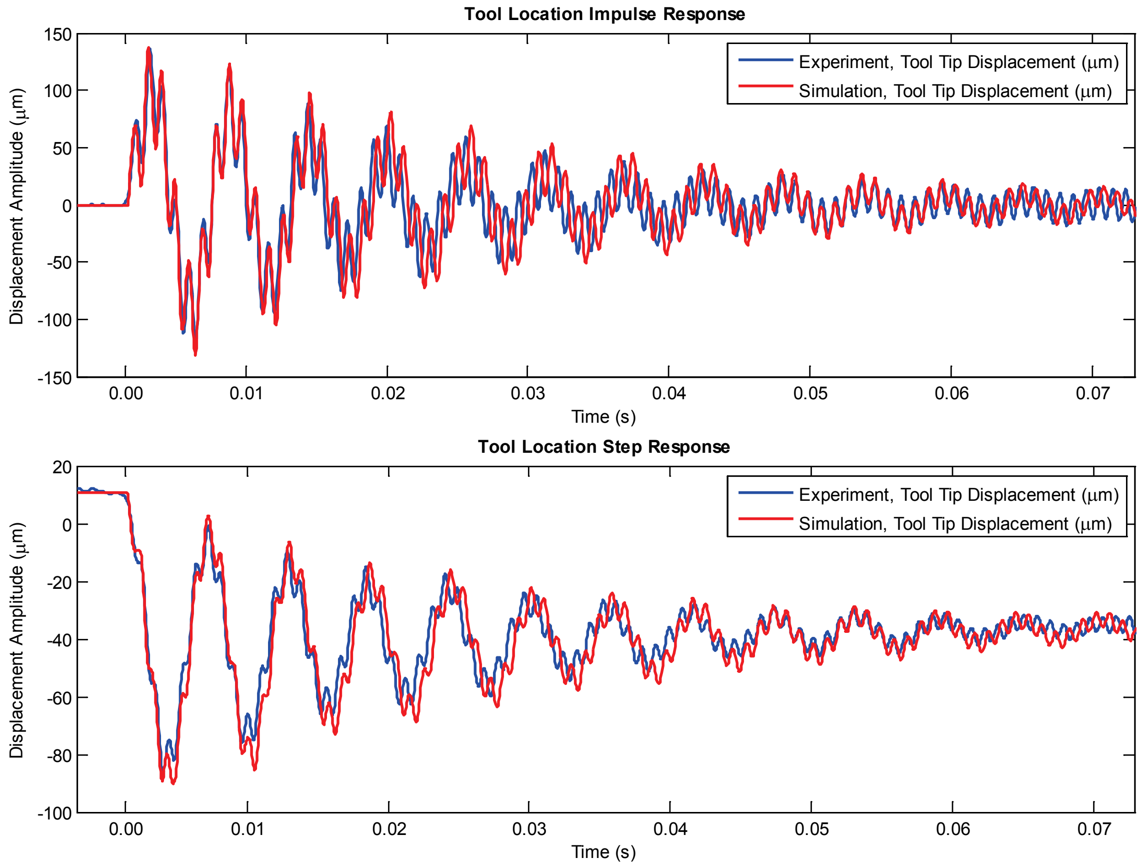

Figure 40: Closed-loop impulse and step response, assessment of simulation prediction with experiment.

Figure 40 illustrates both experimental data and simulations under the same respective conditions previously described. The comparison of the closed-loop simulation with the experimental data shows that the updated model responds very similarly to the real system for both impulse and step responses at the tool location. The updated model provides accurate prediction of its dynamics at a significantly different location (tool) than where the experimental transfer functions for model updating were acquired (AMBs).

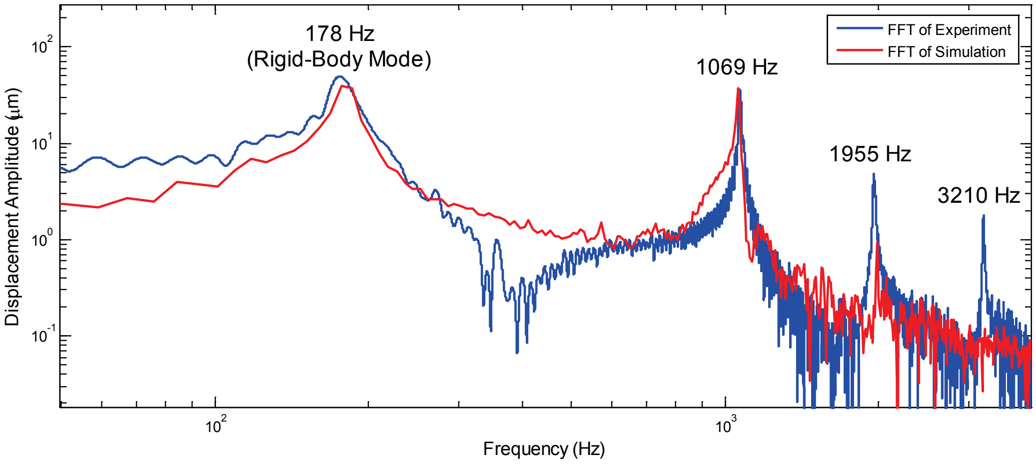

Figure 41: FFT of the impulse response of experiment and simulation illustrating the similitude of the bearing mode at 178 Hz.

Figure 41 illustrates an FFT plot calculated from the experimental and simulated impulse responses from Figure 40, which shows that the fundamental frequency of the closed-loop system is a bearing (rigid-body) mode at 178 Hz. This frequency was induced by the spindle's PID controller in closed-loop coupled with AMB and rotor hardware. Three of the rotor's flexural modes are present as well which were negligibly affected by the PID controller. Through observation of Figure 40 and Figure 41, great confidence was placed in the PID controller model due to the quality of coincidence between simulation and experimental data in both the time and frequency domain of the dominant 178 Hz frequency peak. Hence, the dynamic information extracted from two experimental AMB MIMO transfer functions were shown to be effective for updating the nominal rotor model for confident use in subsequent applications.

3.4 Spindle Modeling Conclusions

The spindle rotor is a complex structure that is difficult to accurately model and to predict its dynamic behavior. The structurally ambiguous regions of the finite element rotor model were chosen to host values of modulus of elasticity which were adjusted by minimization of an error function calculated derived from comparisons with experimental data. Error minimization was performed using an unconstrained Nelder-Mead optimization algorithm which adjusted the E values of the finite element rotor model in order to force discrepancies with experimental data to a minimum.

The resonance and antiresonance frequencies were shown to be important criteria for use in model updating. This ensured that the resonance frequencies as well as mode shape information are incorporated in the updating procedures. To retain a physically accurate rotor model in terms of mass, transverse and polar moments of inertia, and geometry, only the modulus of elasticity of selected finite elements were corrected. The updated model was evaluated to be reliable for predictive use through comparisons of simulation and experimental data at the tool location, which was completely independent of the transfer function data used in model updating. The derivation of unconventional modulus of elasticity values for the select finite elements has shown results that demonstrated a high degree of predictive capability. Since the updated model has been evaluated at other locations than where transfer function data for model updating were acquired, it is suitable for predictive uses in design of model-based MIMO controllers, and is also potentially capable for use in solving for optimal high-speed machining parameters.

CHAPTER IV

SPINDLE MODEL VALIDATION

4.1 Validation of Updated Model

In this chapter, the term *validation* was used to substantiate the updated model's accuracy through implementation of μ-synthesis (MIMO) controller design methodology. The purpose here is not to provide an in depth discussion of μ-synthesis controller design theory, but to demonstrate its application experimentally. The μ-synthesis control strategy is inherently *model based* which means it requires an accurate plant model for successful controller generation and, in particular, experimental implementation. In other words, high performance robust levitation of the spindle rotor is only achieved with a μ-controller when an accurate plant model is provided, coupled with appropriately selected performance weighting and uncertainty specifications.

The PID control strategy (as demonstrated in previous chapters) successfully levitates the spindle rotor. However, this SISO control method is not model-based and requires only a rough plant model for PID controller design, thus not thoroughly fulfilling model validation duties required in this chapter. Further, PID controller design does not quantitatively take into consideration performance weighting functions and uncertainty specifications. In every case, there exist modeling simplifications, assumptions, and errors when compared to the actual physical plant. If the designed controller can tolerate model discrepancies, the controller is considered to be robust. PID controllers sometimes may be considered robust to a certain extent, but cannot guarantee robust levitation through specified performance requirements and uncertainties such as with the μ-controller.

Performance characterization of the high-speed machining spindle was carried out at the tool plane, obtaining dynamic stiffness and orbit measurements in the rotor's levitated state. Study of tool location performance receives priority for the purpose of achieving high quality machining operation. With this in mind, reasonable performance at the magnetic bearings was prescribed, although, was not prioritized. Dynamic stiffness evaluations were presented with both simulation and experiment, supplemented with comparison of results using the existing PID controller. Experimental orbit measurements weren't complemented with simulation due to its dependency on the assumptions made in specifying unbalance magnitude and location on the rotor.

4.2 μ-Synthesis Controller Design Implementation

Various references describe robust control in detail [76] [77] [78] providing detailed descriptions of the μ-synthesis controller design strategy. The μ-synthesis controller design process quantitatively incorporates bounds on the disturbance and parameter uncertainties associated with the plant model. Since the μ-controller is derived based on the given plant model, it is possible to specify performance bounds at locations other than at the AMB sensors.

4.2.1 Introduction to μ-Synthesis Controller Design

The *D-K* iteration μ-synthesis method is used to solve the controller optimization problem. This is a two-step iterative process in which an H_∞ controller is synthesized and the structured singular value μ is used to evaluate whether the specified performance is guaranteed over the prescribed uncertainty. This controller design methodology can be very effective for machining applications due to the presence of varying cutting conditions, notably found in the high-speed machining regime. The specified performance requirement dictates that vibrations at the tool location must be kept to a minimum to maintain desired machining results. By specifying uncertainties of the high-speed machining parameters, μ-controllers may be designed to sacrifice little performance to achieve the necessary robustness [79]. Such MIMO controllers use all positions sensors to control magnetic force applied by each bearing actuator and are able to close feedback loops around all potentially cross-coupled effects to stabilize the rotor. However, a commonly encountered disadvantage to μ-synthesis design method is the inherent requirement of an accurate model which, in many cases, is difficult to produce. For the case of controller synthesis based on an inaccurate model, the performance or relative stability of the controller and physical plant combination will not meet intended design goals.

There have been various successes in the implementation of the μ-synthesis method in application to AMB machining spindles [13] [49] [79] [80] [81] [82]. Discussions of AMB system component modeling have been presented as well the assembly of the open-loop system model. Emphasis in all cases is placed on the accuracy of the plant model which governs the magnitude of uncertainty designed into the μ-controller.

4.2.2 **Benchmark μ-Controller Configuration**

In the past, successful implementation of μ-synthesis controller design has been demonstrated on this AMB spindle in the RoMaDyC laboratory at Cleveland State University [24] [26] [34] [83]. Spindle modeling descriptions were presented as well as descriptions of performance weighting functions and uncertainty specifications for this spindle. The weighting functions included loads assumed at the bearings and tool location, and performance measures which limited AMB coil currents and voltages as well as displacements at the AMB journals.

The μ-controller used in this work was generated with performance weighting functions and uncertainty specifications shown in Table 7. This μ-controller is considered the *benchmark* μ-controller in which subsequent controller research advances in the RoMaDyC laboratory will be compared against. Note that the benchmark μ-controller was designed with the updated plant model presented in previous chapters.

Damping values of the plant model were assumed to be sufficiently accurate based on the experimental system identification. The design intent of this controller was to sustain robust levitation under a variety of excitation sources such as unbalance forces due to rotation (0 to 50,000 rpm), and impulse inputs at the tool location. The performance weighting functions and uncertainty specifications were assumed to be reasonable for benchmarking purposes. Real machining operations were not considered in this work. The benchmark μ-controller's transfer function is illustrated in Figure 42 and is plotted along with the PID controller's transfer function for comparison.

Table 7: Design specifications of the benchmark μ-synthesis controller.

	Tool	**Front AMB**	**Rear AMB**
Maximum DC Load, N	40	100	100
Maximum HF Load, N	5	10	10
Maximum DC Displacement, µm	50	10	10
Maximum HF Displacement, µm	10	30	30
K_x Uncertainty, %	--	10	10
K_i Uncertainty, %	--	5	5

1st Flexible Mode Uncertainty, %	1
2nd Flexible Mode Uncertainty, %	1
First Bending Weight	5

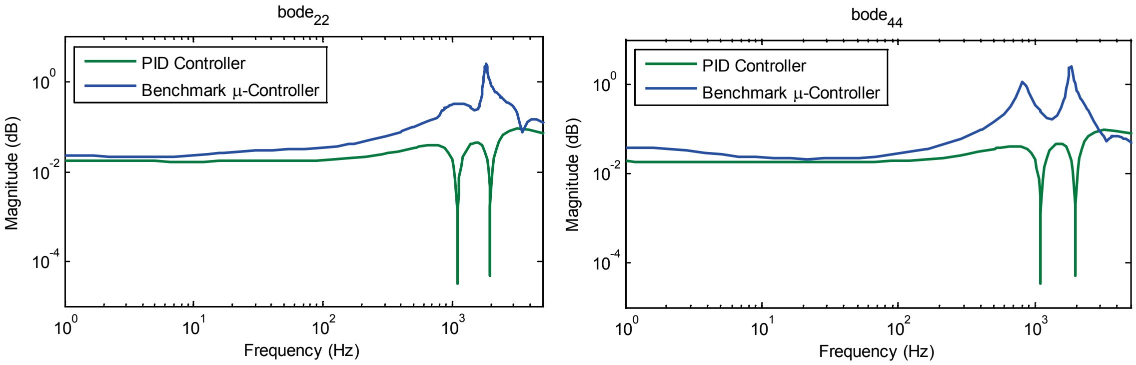

Figure 42: PID and μ-controller transfer functions.

4.3 Performance Characterization

Performance of a machining spindle can be quantified in a variety ways; however, tool stiffness is commonly understood as the desirable characteristic. Static stiffness is dependent on the combination of the bending of the shaft and the deflection in the bearings. Note that the deflection at the bearings is dependent on the rest of the machine structure. On the other hand, dynamic stiffness at the tool is influential on the machine's susceptibility to machining chatter; therefore, understanding this characteristic is desirable. For this reason, the characteristic of interest in the high-speed machining spindle is its dynamic stiffness at the tool plane. This refers to the stiffness of the rotor at the tool location across a range of frequencies, and is also known as the inverse of the dynamic compliance. Any given system will inherently have the lowest dynamic stiffness at the resonance frequencies, and in the case of the AMB spindle, this includes rigid-body bearing modes. In other words, the spindle is most compliant at its resonant frequencies. With increases of the stiffness at the tool location, it is possible to increase the MRR and improve surface finish quality of a machining process.

The orbit of the rotor near the tool plane is measured to verify that robust control is achieved under excitation due to rotation. Orbit measurements are presented, levitated with the μ-controller as well as with the PID controller for comparison. As the orbit amplitude is decreased, it can be inferred that improved machining quality can potentially be achieved.

4.3.1 Dynamic Stiffness and Orbits at Tool Location

The dynamic stiffness measurements were performed on the non-rotating spindle rotor in the levitated state utilizing the μ-controller. Note that dynamic stiffness levitated with the PID controller was included as well. The measurements were conducted using a PCB Piezotronics instrumented hammer and Lion Precision capacitance probe at the tool plane similarly to the impulse testing performed in the previous chapter. The input and output responses of the instrumented hammer and capacitance probe were recorded by a spectrum analyzer which was used to calculate the dynamic stiffness. These responses are plotted in Figure 43 alongside the corresponding model simulations.

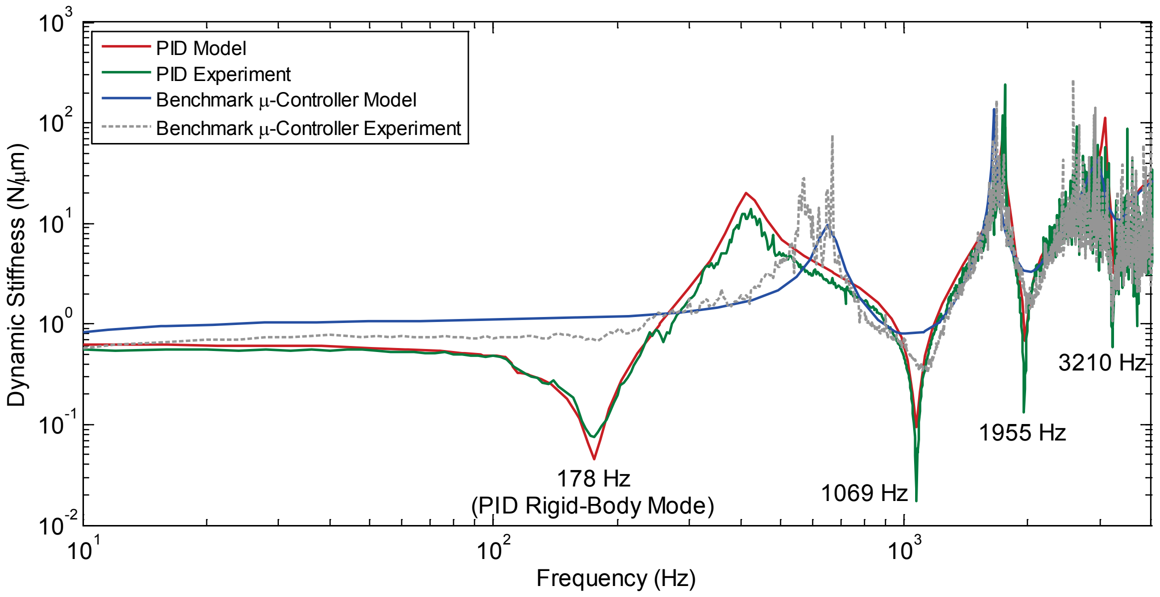

Figure 43: Experimental and simulated dynamic stiffnesses at the tool plane of the *μ*-controller and the PID controller.

Figure 43 illustrates good agreement between the experiment results and closed-loop spindle model simulations, demonstrating the quality of the updated model's predictive capacity. Good agreement is demonstrated in terms of both the frequency domain as well as in overall stiffness amplitudes.

The rotor performance advantage of the successfully implemented *μ*-controller is clear when compared against the PID controller. First, the overall tool location stiffness magnitude is notably higher over the low frequency range as well as at the spindle's maximum speed (833 Hz). Note that because Figure 43 is the inverse of the dynamic compliance plot, the spindle's resonances are annotated as the minimum peaks, which illustrate the rotor's maximum compliance. Second, the responses of the three flexible modes, 1069 Hz, 1955 Hz, and 3210 Hz, are substantially damped by the *μ*-controller when compared with the PID controller. The suppression of resonance frequency responses can be a substantial performance and safety improvement in machines which have to pass through critical speeds. Since the maximum running speed (833 Hz) is well below the first rotor resonance frequency, passing though critical speeds are not a concern for this spindle. Third, under PID control, there exists a rigid-body bearing mode at 178 Hz which is non-existent when levitated with the μ-controller. Similar to the suppression of rotor resonance frequency response, the absence of a rigid-body mode is a significant performance and safety enhancement.

Orbit plots measured near the tool plane were presented to illustrate the spindles performance during rotation in complement the dynamic stiffness plot. Note that it was not possible to effectively measure obits at the tool plane due to the tool holder's geometry as seen in Figure 44. The relatively large notches at the end of the tool holder corrupted a significant portion of the time domain sensor data per each revolution. To avoid this problem, orbits were measured at the next nearest axial plane where the tool holder notches are absent. This orbit measurement plane was 0.75 in from the tool plane towards the rotor's center of mass. Further, orbits measured by the front AMB and rear AMB sensors are included.

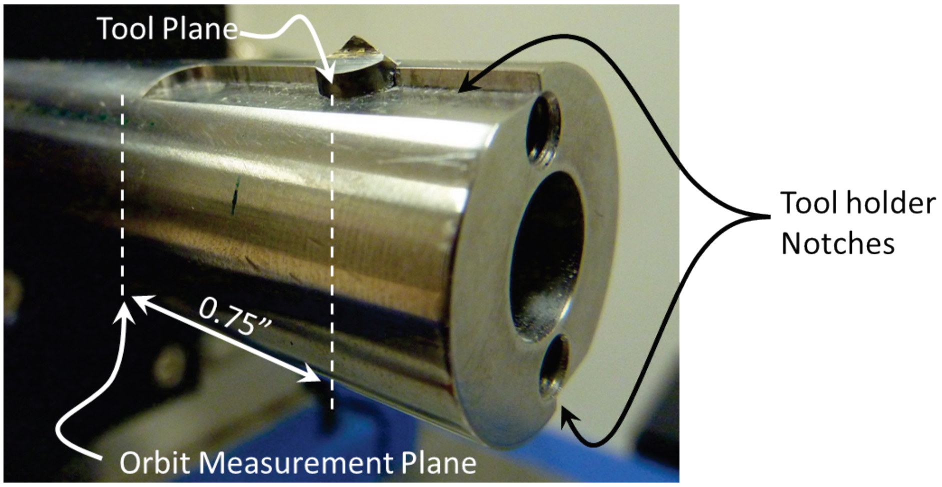

Figure 44: Location of orbit measurement plane is not coincident with tool plane.

The orbit plots in Figure 45 and Figure 46 illustrate the relative difference in performance between the benchmark μ-controller and the existing PID controller with the presence of the gyroscopic effect. Here, attention is given to the correlation of the tool orbit and the dynamic stiffness plot for the corresponding rotational frequency. The rotational speeds presented are 24,000 rpm (400 Hz) and 41,000 rpm (683 Hz) which correspond to the maximum stiffnesses at the tool under PID control and μ-control, respectively, within the running speed range.

At the frequency of 400 Hz, the dynamic stiffness plot in Figure 43 shows that higher stiffness was achieved with the PID controller, which directly reflects the tool orbit performance in Figure 45. The PID controller outperforms the benchmark μ-controller as indicated by the dynamic stiffness plot.

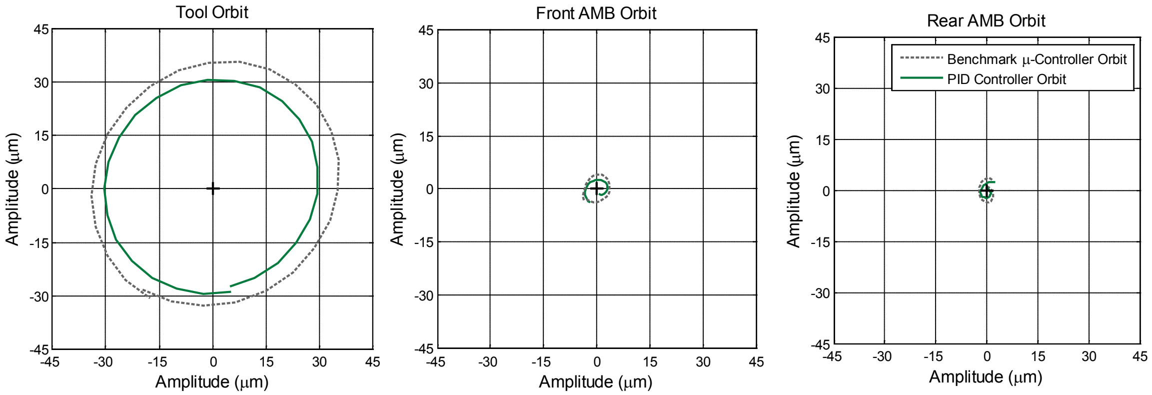

Figure 45: Measured orbits of three rotor locations at speed of 24,000 rpm (400 Hz). The benchmark *μ*-controller demonstrates larger tool orbit amplitudes in comparison to the PID controller performance.

In contrast, the tool orbit plot at in Figure 46 illustrates the substantial improvement in performance when under *μ*-control at 41,000 rpm (683 Hz). This frequency corresponds to the benchmark *μ*-controller's highest dynamic stiffness as seen in Figure 43. The tool orbit amplitude under the benchmark *μ*-controller is on the order of several micrometers, much less than the tool orbit under PID control. Further observation shows that the orbit amplitude for the *μ*-controller at the AMB's is substantially higher. This is due to the inherent MIMO capability of the *μ*-controller to guarantee high frequency tool displacements to a maximum of 10 μm and also to relax the high frequency AMB displacements to a maximum of 30 μm. See Table 7. To achieve the specified *μ*-controller design goals, the *μ*-controller intentionally increased the displacements at the AMBs in order to minimize deflections at the tool location. On the other hand, the SISO PID controller's only design goal was to minimize displacements at the individual AMB axes with no consideration for displacements at the tool location.

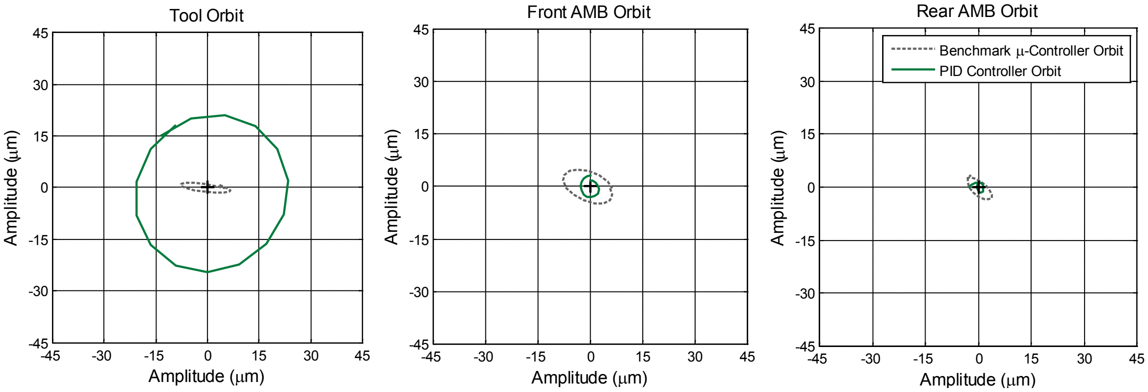

Figure 46: Measured orbits of three rotor locations at speed of 41,000 rpm (683 Hz). The benchmark μ-controller demonstrates substantially better tool performance at its highest stiffness.

4.4 Dynamic Stiffness Varying Flexible Mode Uncertainty

The study presented in this section is based on four μ-controllers which are very similar to benchmark μ-controller previously exhibited. The focus here is to demonstrate the impact of plant model accuracy in the design of μ-controller through observations of the dynamic stiffness at the tool location. The four μ-controllers were designed with different flexible mode uncertainties specified to them, ranging from 1.0 % to 4.0 %. The flexible mode uncertainty specifies the uncertainty of the first two resonance frequencies of the model. Although the same updated open-loop plant was used for synthesis of all μ-controllers, the uncertainty designed into the controller was adjusted to accommodate for varying degrees of plant model inaccuracy. The purpose of doing this was to demonstrate the significance and the advantage of designing μ-controllers with high plant model accuracy.

It should be noted that the benchmark μ-controller has been developed independently from the series of four μ-controller found in this section. The benchmark μ-controller has been designed with 1.0 % flexible mode uncertainty and with a high frequency tool deflection performance specification of 10 μm as seen in Table 7. With this tool deflection performance specification, it was not possible to generate μ-controllers with larger flexible mode uncertainties. For this reason, the series of four μ-controllers in this section required a relaxation of the high frequency tool deflection performance requirement to 15 μm. With this adjusted μ-controller design parameter, it was possible to successfully generate μ-controllers with up to 4.0 % flexible mode uncertainty. As the demands for controller performance increased, the less tolerant the μ-controller design process was for plant modeling error.

4.4.1 μ-Controller Configuration

The design parameters of the four μ-controllers are listed in Table 8. Note that the High Frequency (HF) displacement has been relaxed to 15 μm in order to achieve μ-controllers with flexible mode uncertainty values of 1.0 % to 4.0 %. All other μ-controller design parameters were kept constant.

Table 8: μ-controller design parameters for generation of four μ-controllers with varying flexible mode uncertainties.

	Tool	**Front AMB**	**Rear AMB**
Maximum DC Load, N	40	100	100
Maximum HF Load, N	5	10	10
Maximum DC Displacement, μm	50	10	10
Maximum HF Displacement, μm	**15**	30	30
K_x Uncertainty, %	--	10	10
K_i Uncertainty, %	--	5	5

1st Flexible Mode Uncertainty, %	1, **2, 3,** and **4**
2nd Flexible Mode Uncertainty, %	1, **2, 3,** and **4**
First Bending Weight	5

4.4.2 **Experiments with Varying Flexible Mode Uncertainty**

Figure 47 illustrates the tool location dynamic stiffness for each of the four μ-controllers with varying flexible mode uncertainties. Although the benchmark μ-controller has a different HF displacement specification, it was included for comparison. The experimental results show the difference in low frequency stiffness, the lowest being the μ-controller with 4.0 % flexible mode uncertainty. Incremental increase of dynamic stiffness is observed when the flexible mode uncertainty designed into the μ-controller is decreased.

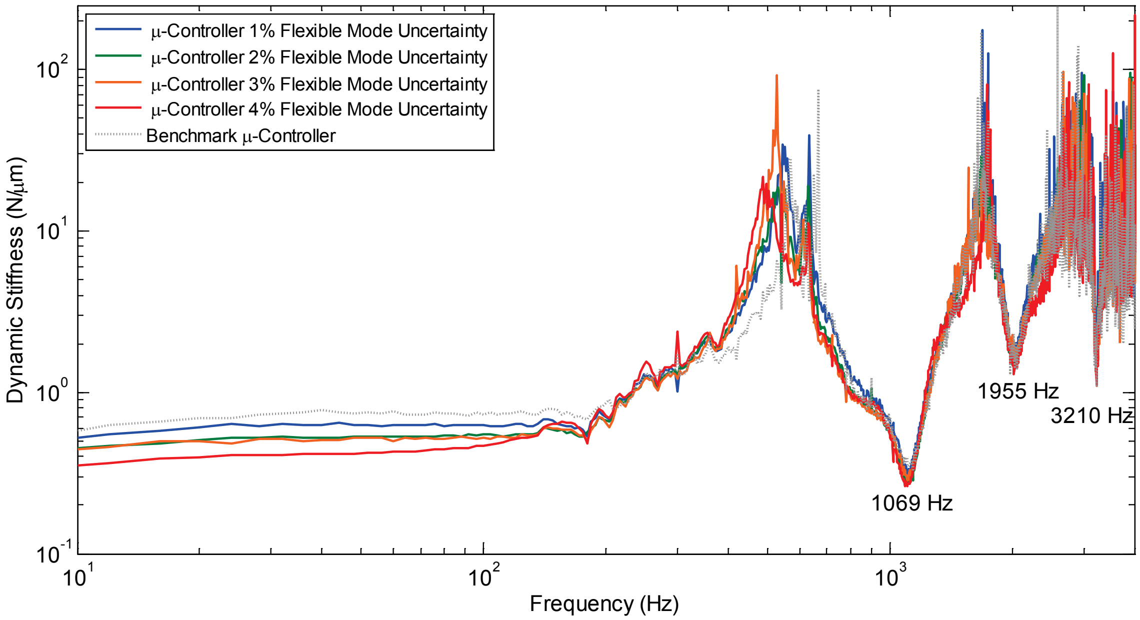

Figure 47: Experimental dynamic stiffness results comparing μ-controllers designed with flexible mode uncertainties ranging from 1.0 % to 4.0 %. There is a noticeable increase in low frequency amplitude with the μ-controller designed with less flexible mode uncertainty. The benchmark μ-controller is included for comparison.

Figure 48 presents more detailed observations of the tool location stiffness at the first and second flexible mode frequencies, showing that there exists substantial improvement in suppression of the rotor's resonance frequencies. Again, the μ-controller with 4.0 % flexible mode uncertainty exhibited the lowest suppression of the resonance response, while the μ-controller with 1.0 % flexible mode demonstrated higher stiffness values at resonance. The improvement was approximately 24 % and 16 % increase in stiffness for the first and second flexible mode responses, respectively. The μ-controllers with 2.0 % and 3.0 % flexible mode uncertainty show responses that fall between the 1.0 % and 4.0 % μ-controller responses, as intuitively expected.

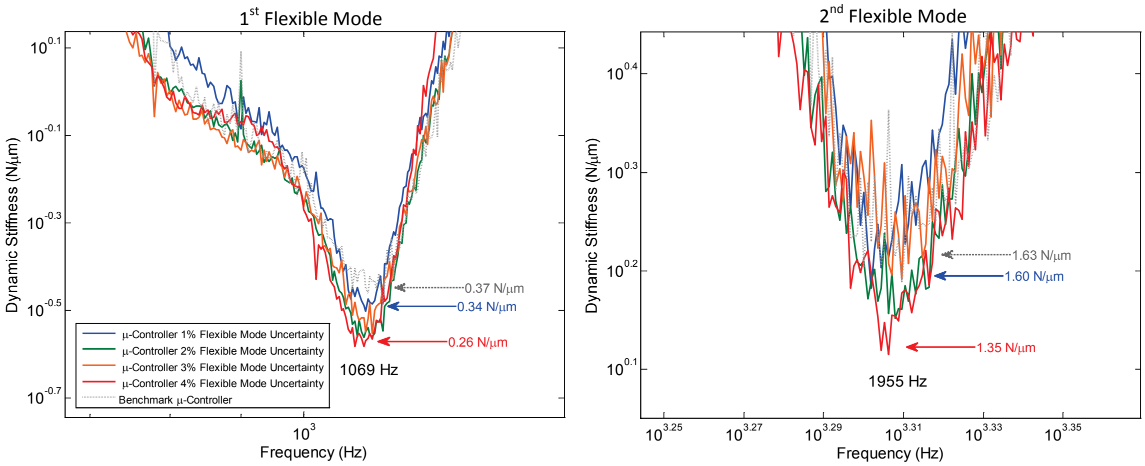

Figure 48: The zoomed in views of dynamic stiffness at the first and second flexible modes show improvements of approximately 24 % and 16 % increase in stiffness, respectively. The benchmark *μ*-controller is included for comparison which exhibits even higher stiffnesses.

Orbit measurements in Figure 49 were acquired for the series of *μ*-controllers at a maximum speed of 36,000 rpm (600Hz). Higher speeds as seen in Figure 45 and Figure 46 were not attempted for concerns for lab safety. However, the experimental tool orbits exhibit a significant difference in amplitude. The *μ*-controller with 4.0 % flexible mode uncertainty shows a dramatic increase in orbit amplitude over the *μ*-controller with 1.0 % flexible mode uncertainty. Note that the benchmark *μ*-controller has the lowest amplitude orbit by a small margin.

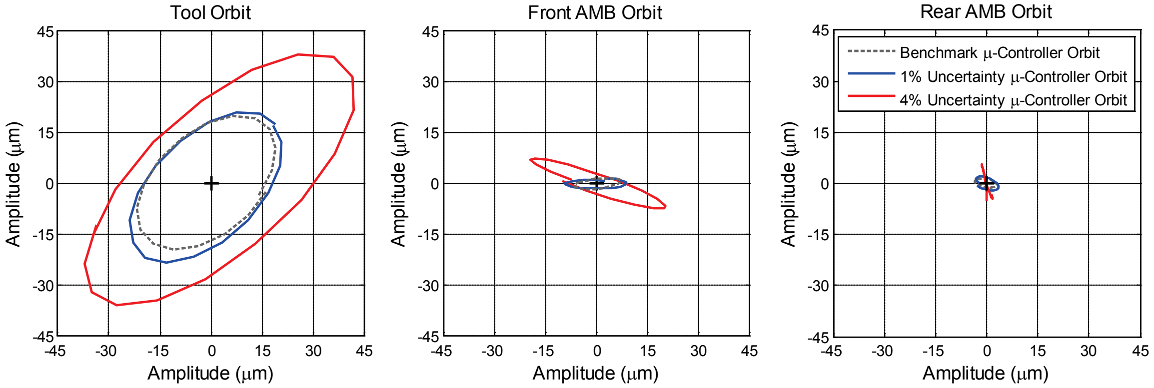

Figure 49: Measured orbits of three rotor locations at speed of 36,000 rpm (600 Hz). The tool orbit with the 1.0 % flexible mode uncertainty *μ*-controller performs better than with the 4.0 % flexible mode uncertainty *μ*-controllers. The benchmark *μ*-controller is included for comparison.

Based on the experimental tool performance data, there exists a clear trend demonstrating the effect of plant model uncertainty designed into the *μ*-controller. The resulting *μ*-controller designed with less plant model uncertainty had demonstrated higher low frequency stiffness and better suppression of resonance frequencies at the tool location. The measured orbits at the tool agree with dynamic stiffness experiments at the corresponding frequencies.

CHAPTER V

CONCLUSIONS

This research has addressed the process of modeling and model validation of the magnetically levitated machining spindle. The process consisted of system identification and extraction of open-loop transfer functions, assembling an open-loop spindle model, updating the open-loop model to accurately represent the system identification data. Further, updated model assessments and validation operations were carried out. Assessments and validations have been investigated in closed-loop form under PID and μ-controllers. Several conclusions throughout this process have been made.

System identification of the spindle consisted of sine sweeps while levitated under PID control. The sine sweeps were conducted in a MIMO scheme resulting in a sixteen closed-loop transfer functions defined by the four lateral control axes. The open-loop transfer functions were calculated in efforts to isolate the rotor hardware. Note that the spindle rotor was not removed from the test rig and all system identification was performed in situ using all existing AMB hardware.

The open-loop model was developed to represent the open-loop system which consisted of the FE rotor model, amplifier model, and AMB parameters. The amplifier model and AMB parameters were assumed to be correct as they had little influence on the calculated open-loop transfer functions. The FE rotor model was the dominant component in the open-loop system. A nominal FE rotor model was developed based on the rotor design drawings; however, the model did not represent the system identification data accurately in terms of resonance and antiresonance frequencies. Traditionally, hand-tuning of the model is the method for model adjustments, but due to the rotor's complexity, an automated open-loop model updating methodology was required and developed.

Open-loop model updating was developed based on minimizing error of the difference in experimental and calculated transfer functions on one rotor plane. It was found to be sufficient to use two transfer functions, one having the input/output at the front AMB and the other having input/output at the rear AMB, in a single plane. The error was quantified by the difference of the corresponding resonance peaks and antiresonance peaks. The adjusted variables in the FE rotor were the modulus of elasticity of finite elements in structurally ambiguous regions in the rotor. In this way, the rotor's mass and inertial properties remained correct and only the rotor's dynamic properties were corrected. The errors were minimized through application of an optimization routine which adjusted the modulus of elasticity of the selected finite elements accordingly. The use of both the resonance and antiresonance information was found to be necessary in defining the rotor dynamics in the frequency and spatial domains. The resonances are, of course, defining the natural frequencies of the system, while the antiresonances were found to be strongly correlated to mode shapes, particularly to bending node locations. A novel case study was presented to directly correlate the antiresonances in the frequency domain to the mode-shapes in the spatial domain. Further, the solution derived by the model updating methodology had solved for unrealistic values for the selected modulus of elasticity variables. However, it was shown that this was not a concern for the reason that the FE rotor model represented the real system physically, i.e., geometry, mass, and inertias, as well dynamically, i.e., resonances and mode shapes. Although this was the case, an updated model assessment and validation campaign was carried out.

Updated model assessments were carried out to verify quality of the updated model's predictive ability at the tool location. In closed-loop form under PID control, simulations with the updated model where compared to experimental mode shape measurements, and time domain impulse and step responses at the tool location. The comparisons showed nearly identical correspondence between experiments and simulations. This established that, although the updated FE rotor model's moduli of elasticity values were questionable, it produced nearly identical dynamic predictions when compared with experimental data. Further, this concluded that the system identification data acquired at the front and rear AMBs in one plane was sufficient to constrain the open-loop plant optimization problem for the rotor solution to generate high quality dynamic predictions at other locations on the rotor.

Final updated model validations were performed through implementation of μ-controllers generated based on the updated FE rotor model. The concept for this was that since the MIMO μ-controller was designed based on the updated plant model provided, the rotor will not levitate robustly if the plant model was not representative of the real spindle. Firstly, the successful experimental implementation of the μ-controller demonstrates the high quality of the updated open-loop plant model. Secondly, it was demonstrated that the μ-controller performance was significantly improved by generating μ-controllers with less defined flexible mode uncertainty in the updated model. Although the same updated open-loop plant was used for all cases, the μ-controller designed with a 4.0 % uncertainty in flexible mode uncertainty did not perform as well as the μ-controllers with 1.0 % uncertainty. Hence, significant performance improvements were experimentally demonstrated possible when designing model-based MIMO controllers with increases in model accuracy. Notable suppression of resonance responses were observed as well as elimination of a rigid-body mode seen with PID control. Based on results in this work, an automated open-loop model updating routine for use in a magnetically levitated machining has significant benefits and is worth the model correction efforts.

Applications for the presented methodology can easily be envisioned practical were magnetically levitated system are utilized. For example, magnetically levitated machining spindles can benefit greatly with the automated system identification, model updating, and μ-controller generation. It is common practice for CNC machines to utilize tool cassettes carrying an array of tools from which the machining spindle selects from for the specific machining process. Since each tool has a slightly different mass and geometry, changes to the spindle's plant will occur, causing degradation in robustness of rotor levitation or even complete failure to levitate. Based on the research performed in this work, the automated system identification, model updating, and μ-controller generation for each individual tool is envisioned to enable optimized high-speed machining performance for CNC machines equipped with AMB spindles using multiple tools. Although this automated process would be completed prior to machining operation, once completed, the machine can select the optimal μ-controller for each corresponding tool to ensure the highest achievable stiffness and performance at the tool location. With optimized tool performance, MRR can be increased with better surface finishes and have more favorable stability lobe regions.

BIBLIOGRAPHY

[1] R. Jerard, B. Fussell, M. Xu and C. Schuyler, "A Testbed for Research on Smart Machine Tools," in *International Conference on Smart Machining Systems*, Gaithersburg, 2007.

[2] K. Jurrens , J. Soons and R. Ivester, "Smart Machining Research at the National Institute of Standards and Technology," in *Small Lots Intelligent Manufacturing Workshop*, Santa Fe, 2003.

[3] R. Ivester and J. Heigel, "Smart Machining Systems: Robust Optimization and Adaptive Control Optimization for Turning Operations," *NAMRI/SME,* vol. 35, 2007.

[4] L. Deshayes, L. Welsch, A. Donmez and R. Ivester, "Robust Optimization for Smart Machining Systems: An Enabler for Agile Manufacturing," *ASME International Mechanical Engineering Congress & Exposition,* November 2005.

[5] S. Liang, R. Hecker and R. Landers, "Machining Process Monitoring and Control: The-State-of-the-Art," *ASME Journal of Manufacturing Science and Engineering,* vol. 126, pp. 297-310, May 2004.

[6] M. Donmez, K. Yee and B. Damazo, "Some Guidelines for Implementing Error

Compensation on Machine Tools," *National Institute of Standards and Technology NISTIR,* 1993.

[7] J. Koelsch, "High Speed Machining; A Strategic Weapon," *Machine Shop Guide,* 2001.

[8] S. Badrawy, "Cutting Dynamics of High Speed Machining," *WolfTracks,* vol. 8, no. I, 2001.

[9] H. Schulz, "The History of High-Speed Machining," *Revista de Ciencia & Tecnologia,* June 1999.

[10] D. West, "High Performance Aluminum and Titanium Machining," in *High Speed Machining Seminar*, Seattle, 2002.

[11] J. Halley, A. Helvey, S. Smith and W. Winfough, "The Impact of High-Speed Machining on the Design and Fabrication of Aircraft Components," *Proceedings of the 17th Biennial Conference on Mechanical Vibration and Noise,* September 1999.

[12] Y. Shin, B. Jorgensen and S. Jensen, "Modeling of Machine Tool Dynamics and Chatter Prediction," *Society of Automotive Engineers,* June 1996.

[13] L. Fittro, *A High Speed Machining Spindle with Active Magnetic Bearings: Control Theory, Design, and Application,* Dissertation ed., Virginia: Univerity of Virginia, 1998.

[14] J. McGee, "Manufacturing Methods for High-Speed Machining," 1978.

[15] A. Dashchenko, Ed., Manufacturing Technologies for Machines of the Future, Berlin Heidelberg: Springer, 2003.

[16] C. Salomon, "Process for the Machining of Metals or Similarly-Acting Materials When Being Worked by Cutting Tools". Germany Patent 523594, April 1931.

[17] R. King, "High-Speed Milling Production of Non-Ferrous Materials," *North American Metals Research Conference,* May 1976.

[18] R. King, "The Benefits of Ultra High-Speed Machining.," *Tooling and Production,* January 1978.

[19] Staubli, 2011. [Online]. Available: http://www.staubli.com/en/robotics/products/6-axis-scara-industrial-robot/specialized-robot/high-speed-machining-robot/rx170-hsm/.

[20] P. M. T. Corp., 2011. [Online]. Available: http://www.primero.com.tw/blog/km-11va.

[21] Y. Cao and Y. Altintas, "A General Method for the Modeling of Spindle-Braring Systems," *Journal of Mechanical Design,* vol. 126, November 2004.

[22] T. Schmitz, J. Ziegert and C. Stanislaus, "A Method for Prediction Chatter Stability for system with Speed-Dependent Spindle Dynamics," *Society of Manufacturing Engineers,* 2004.

[23] M. Chen and C. R. Knospe, "Control Approaches to the Suppression of Machining Chatter Using Active Magnetic Bearings," *IEEE Transactions on Control Systems Technology,* vol. 15, no. 2, pp. 220-232, 2007.

[24] J. T. Sawicki, H. Maslen and K. Bischof, "Modeling and Performance Evaluation of Machining Spindle with Active Magnetic Bearings," *Mechanical Science and*

Technology, 2007.

[25] R. Fittro and C. Knopse, "μ-Synthesis Control Design Applied to a High Speed Machining Spindle with Active Magnetic Bearings," *6th International Symposium on Magnetic Bearings,* pp. 449-458, 1998.

[26] J. T. Sawicki and E. Maslen, "Accurate Identification of Plant Model for Robust Control of an AMB Machine Tool Spindle," in *International Conference on Motion and Control*, 2008.

[27] C. Won-Lee, "Mechatronics in Rotating Machinery," *7th IFToMM-Conference on Rotor Dynamics,* 25-28 September 2006.

[28] S. Earnshaw, "On the Nature of the Molecular Forces which Regulate the Constitution of the Luminiferous Ther," *Transactions Cambridge Philosophical Society,* vol. 7, pp. 97-112, 1842.

[29] J. Bichsel, "The Bearingless Electrical Machine," *Procedings of International Symposium on Magnetic Suspension Technologies,* 1991.

[30] C. Knopse, "Introduction to the Special Issue on Magnetic Bearing Control," *IEEE Transactions on Control Systems Technology,* vol. 4, no. 5, September 1996.

[31] C. Lee and H. Jeong, "Dynamic Modeling and Optimal Control of Cone-Shaped Active Magnetic Bearing Systems," *Control Engineering Practice,* vol. 4, no. 10, pp. 1393-1403, 1996.

[32] J. E. Vrancik, "Prediction of Windage Power Loss in Alternators," *Nasa Technical Note, Lewis Research Center,* no. NASA TN D-4849, 1968.

[33] H. Liu, C. Hearn, M. Werst, J. Hahne and D. Bogard, "Splits of Windage Losses in Integrated Transient Rotor and Stator Thermal Analysis of a High-Speed Alternator During Multiple Discharges," *IEEE Transactions on Magnetics,* vol. 41, no. 1, pp. 311-315, January 2005.

[34] J. T. Sawicki and E. Maslen, "Rotordynamic Response and Identification of AMB Machining Spindle," *ASME Turbo Expo,* May 2007.

[35] A. Muszynska, Rotordynamics, Boca Raton: CRC Press, 2005.

[36] Revolve, [Online]. Available: http://www.skf.com/portal/skf_rev/home/products?contentId=079782&lang=en.

[37] IBAG, 2010. [Online]. Available: http://www.ibag.fr/Motor-spindles-range.html.

[38] S2M. [Online]. Available: http://www.s2m.fr/E/4-APPLICATIONS/milling.html.

[39] Mecos;, [Online]. Available: http://www.mecos.com/en/industries/index.php.

[40] Synchrony, 2009. [Online]. Available: www.synchrony.com/documents/090109_Fusion.pdf.

[41] Waukesha, 2009. [Online]. Available: www.waukbearing.com/downloads/ActiveMag_ENG.pdf.

[42] Cleveland State University. [Online]. Available: http://academic.csuohio.edu/romadyc/.

[43] R. M. B. Inc, "User's Guide - Magnetic Bearing Controller MBControl".

[44] R. M. B. Inc, "User's Guide - MBResearch".

[45] R. M. B. Inc, "User's Guide - Amplifier Chassis MB12400".

[46] J. Mottershead, "On the Zeros of Structural Frequency Response Functions and Their Sensitivities," *Mechanical Systems and Processing,* vol. 12, no. 5, pp. 591-597, February 1998.

[47] K. Jones, "Finite Element Model Updating Using Antiresonant Frequencies," 2000.

[48] W. D. D'Ambrogio and A. Fregolent, "The use of Antiresonances for Robust Model Updating," *Journal of Sound and Vibration,* vol. 236, no. 2, pp. 227-243, 2000.

[49] F. Losch, "Identication and Automated Controller Design for Active Magnetic Bearing Systems," Zurich, 2002.

[50] O. Gasparyan, Linear and Nonlinear Multivariable Feedback Control: A Classical Approach, Chichester West Sussex: John Wiley & Sons Ltd, 2008.

[51] G. Genta, Vibration Dynamics and Control, F. Ling, Ed., New York: Springer Science+Business Media, 2009.

[52] V. Ramamurti, Mechanical Vibration Practive with Basic Theory, New Delhi: Narosa Publishing House, 2000.

[53] J. Vance, Rotordynamics of Turbomachinery, John Wiley & Sons, Inc, 1988.

[54] R. J. Prins, "System Identification and Calibration Techniques for Force Measurement in Active Magnetic Bearings," Blacksburg, 2005.

[55] A. Berman and W. Flannely, "Theory of Incomplete Models of Dynamic Structures," *AIAA Journal,* vol. 9, no. 8, August 1971.

[56] M. Friswell and J. Mottershead, Finite Element Model Updating in Structural Dynamics, Dordrecht: Kluwer Academic Publishers, 1995.

[57] C. Hatch, G. Skingle, C. Greaves, N. Lieven, J. Coote, M. Friswell, J. Mottershead, H. Shaverdi, C. Mares, A. McLaughlin, M. Link, N. Piet-Lahanier, M. Van Houten , D. Goge and H. Rottmayr, "Methods for Refinement of Structural Finite Element Models: Summary of the GARTEUR AG14 Collaborative Programme," *32nd European Rotorcraft Forum,* 2006.

[58] Y. Xiong, W. Chen and K. Tsui, "A Better Understanding of Model Updating Strategies in Validating Engineering Models," in *AIAA Structures, Structural Dynamics, and Materials Conference*, Schaumburg, 2008.

[59] N. Maia and J. Silva, "Modal Analysis Identification Techniques," *The Royal Society,* 2001.

[60] D. Barthe, A. Deraemaeker, P. Ladeveze and S. Loch, "Validation and Updating of Industrial Models Based on the Constitutive Relation Error," *AIAA Journal,* vol. 42, no. 7, July 2004.

[61] S. Rao, Engineering Optimization, Theory and Practice, Hoboken: John Wiley & Sons, Inc., 2009.

[62] E. Hendrix and B. Toth, Introduction to Nonlinear and Global Optmization, New York: Springer Science+Business Media, LLC, 2010.

[63] A. Conn, K. Scheinberg and L. Vicente, Introduction to Derivative-Free Optimization, Philadelphia: Society for Industrial and Applied Mathematics and the Mathematical Programming Society, 2009.

[64] J. Dennis and R. Schnabel, Numerical Methods for Unconstrained Optimization and

Nonlinear Equations, Englewood Cliffs: Society for Industrial and Applied Mathematics, 1996.

[65] G. Steenackers and P. Guillaume, "Finite Element Model Updating Taking Into Account the Unceratainty on the Modal Parameter Estimates," *Journal of Sound and Vibration,* June 2006.

[66] T. Marwala, Finite-element-model Updating Using Computational Intelligence Techniques, London: Springer, 2010.

[67] D. Ewins, Modal Testing: Theory, Practice and Applications, Sussex: Research Studies Press Ltd, 2000.

[68] Y.-X. Xu, *Sensitivity-Based Finite Element Model Updating Methods with Application to Electronic Equipments,* Facult´e Polytechnique de Mons, Belgium, 1999.

[69] R. Allemang and D. Brown, "A Correlation Coefficient for Modal Vector Analysis," in *1st International Modal Analysis Conference*, 1982.

[70] N. Lieven and D. Ewins, "Spatial Correlation of Modeshapes, the Coordinate Modal Assurance Criterion (COMAC)," *International Modal Analysis Conference,* pp. 690-695, 1988.

[71] B. Titurus, M. Friswell and L. Starek, "Damage detection using generic elements: Part I. Model updating," in *Computers and Structures*, 2003.

[72] P. Bakir, E. Reynders and G. Roeck, "Sensitivity-based Finite Element Model Updating Using Constrained Optimization with a Trust Region Algorithm," *Journal*

of Sound and Vibration, vol. 305, pp. 211-225, August 2007.

[73] J. Nelder and R. Mead, "A Simplex Method for Function Minimization," *The Computer Journal,* pp. 308-313, 1965.

[74] W. Yang, W. Cao, T. Chung and J. Morris, Applied Numerical Methods Using MATALB, Hoboken: John Wiley & Sons, Inc., 2005.

[75] W. Press, S. Teukolsky, W. Vetterling and B. Flannery, Numerical Recipes in C, The Art of Scientific Computing, 2nd ed., New York: Press Syndicate of the University of Cambridge, 1992.

[76] W. K. Gawronski, Advanced Structural Dynamics and Active Control of Structures, New York: Springer, 2004.

[77] D. Xue, Y. Chen and D. P. Atherton, Linear Feedback Control, Philadelphia: Society for Industrial and Applied Mathematics, 2007.

[78] D.-. W. Gu, P. H. Petkov and M. M. Konstantinov, Robust Control Design with MATLAB, Verlag: Springer, 2005.

[79] C. R. Knospe, R. L. Fittro and L. S. Stephans, "Control of a High Speed Machining Spindle via μ-Synthesis," in *IEEE Conference on Control Applications*, Hartford, 1997.

[80] L. S. Stephans and C. R. Knospe, "μ-Synthesis Based, Robust Controller Design for AMB Machining Spindles," in *Fifth International Symposium on Magnetic Bearings*, Kanazawa, 1996.

[81] R. L. Fittro and C. R. Knospe, "The μ Approach to Control of Active Magnetic

Bearings," *Journal of Engineering for Gas Turbines and Power,* vol. 124, no. 3, pp. 566-571, July 2002.

[82] H. J. Ahn and D. C. Han, "System Modeling and Robust Control of an AMB Spindle: Part II A Robust Control Design and its Implementation," *KSME International Journal,* vol. 17, no. 12, pp. 1855-1866, 2003.

[83] J. T. Sawicki, E. H. Maslen and K. R. Bischof, "AMB Controller Design for a Machining Spindle Using μ-Synthesis," in *Tenth International Symposium on Magnetic Bearings*, Torino, 2006.

[84] S. Rao, Engineering Optimization Theory and Practice, fourth ed., Hoboken: John Wiley & Sons, Inc., 2009.

[85] L. Stephans, "Design and Control of Active Magnetic Bearings for A High Speed Machining Spindle," 1995.

[86] G. Li, Z. Lin and P. Allaire, "Uncertainty Classification for Rotor-AMB Systems," in *International Symposium on Magnetic Bearings*, Torino, 2006.

[87] S. Jafri, "Shrink Fit Effects on Rotordynamic Stability: Experimental and Theoretical Study," 2007.

[88] T. Janter and P. Sas, "Uniqueness Aspects of Model-Updating Procedures," *American Institute of Aeronautics and Astronautics,* vol. 28, no. 3, pp. 538-543, March 1990.

[89] J. Mottershead and M. Friswell, "Model Updating in Structural Dynamics: A Survey," *Journal of Sound and Vibrations,* vol. 167, no. 2, pp. 347-375, 1993.

[90] A. Conn , K. Scheinberg and L. Vicente, Introduction to Derivative-Free Optmization, Philadelpia : Society for Industrial and Applied Mathematics and the Mathematical Programming Society, 2009.

[91] J. T. Sawicki and E. Maslen, "Rotordynamic Response and Identification of AMB Machining Spindle," *ASME Turbo Expo,* May 2007.

[92] A. C. Wroblewski, J. T. Sawicki and A. H. Pesch, "High-Speed AMB Machining Spindle Model Updating and Model Validation," in *SPIE*, San Diego, 2011.